Structural-induced modifications of electronic properties in low dimensional systems : transition-metal dichalcogenides and rare-earth diantimonides

Jairo Obando Guevara

▶ **To cite this version:**

Jairo Obando Guevara. Structural-induced modifications of electronic properties in low dimensional systems : transition-metal dichalcogenides and rare-earth diantimonides. Physics [physics]. Université Paris-Saclay; Université Complutense de Madrid (1836-..), 2023. English. NNT : 2023UPASP196 . tel-04493384

HAL Id: tel-04493384
https://hal.science/tel-04493384v1

Submitted on 10 Jan 2025

HAL is a multi-disciplinary open access archive for the deposit and dissemination of scientific research documents, whether they are published or not. The documents may come from teaching and research institutions in France or abroad, or from public or private research centers.

L'archive ouverte pluridisciplinaire **HAL**, est destinée au dépôt et à la diffusion de documents scientifiques de niveau recherche, publiés ou non, émanant des établissements d'enseignement et de recherche français ou étrangers, des laboratoires publics ou privés.

THESE DE DOCTORAT

NNT : 2023UPASP196

Structural-induced modifications of electronic properties in low dimensional systems: transition-metal dichalcogenides and rare-earth diantimonides

Modifications structurellement induites des propriétés électroniques de systèmes à basse dimensionnalité : dichalcogénures de métaux de transition et diantimoniures de terres rares

Thèse de doctorat de l'université Paris-Saclay et de l'Université Complutense de Madrid

École doctorale n° 564, Physique en Île-de-France (PIF)
Spécialité de doctorat: Physique
Graduate School : Physique, Référent : Faculté des sciences d'Orsay

Thèse préparée à **Laboratoire de Physique des Solides** (Université Paris-Saclay, CNRS) et au **Departamento de Física de Materiales** (Universidad Complutense de Madrid), sous la direction de **Antonio TEJEDA GALA**, directeur de recherche, et **Arantzazu MASCARAQUE SUSUNAGA**, professeur des universités.

Thèse soutenue à Paris-Saclay, le 15 Décembre 2023, par

Jairo Israel OBANDO GUEVARA

Composition du jury

Membres du jury avec voix délibérative

Véronique BROUET Directrice de Recherche, Université Paris-Saclay	Présidente
Juan DE LA FIGUERA BAYÓN Directeur de recherche, Instituto de Química Física Blas Cabrera, Consejo Superior de Investigaciones Científicas	Rapporteur & Examinateur
Daniel MALTERRE Professeur des universités, Université de Lorraine	Rapporteur & Examinateur
María Pilar MARÍN PALACIOS Professeur des universités, Universidad Complutense de Madrid	Examinatrice
Óscar RODRíGUEZ DE LA FUENTE Maître de conférences, Universidad Complutense de Madrid	Examinateur

université PARIS-SACLAY | ÉCOLE DOCTORALE Physique en Île-de-France (PIF)

Titre: Modifications structurellement induites des propriétés électroniques de systèmes à basse dimensionnalité : dichalcogénures de métaux de transition et diantimoniures de terres rares.

Mots clés: ARPES, $LaSb_2$, onde de densité de charge (ODC), MoS_2, états de puits quantiques discrets, réaction de dégagement de l'hydrogène (HER).

Résumé: L'avènement des matériaux bidimensionnels (2D) offre une plateforme unique pour l'étude des solides à l'échelle atomique. Cependant, la manipulation des matériaux 2D est complexe et reste un inconvénient pour lequel aucune solution pratique n'a été trouvée pour l'élaboration massive de dispositifs. Les matériaux quasi 2D sont plus faciles à manipuler tout en conservant parfois les propriétés essentielles des matériaux strictement 2D. Cette thèse présente trois systèmes qui illustrent comment la structure électronique des matériaux quasi-2D peut être modifiée par des changements induits dans la structure atomique.

Les matériaux quasi 2D sont assez sensibles aux instabilités de la surface de Fermi (SF), qui peuvent induire des transitions de phase. Dans ce contexte, la magnétorésistance linéaire du $LaSb_2$ a été expliquée par une éventuelle onde de densité de charge (ODC). En effet la structure anisotrope du $LaSb_2$ donne lieu à une SF de faible dispersion en k_z qui a des régions favorables à l'emboîtement. En utilisant la spectroscopie de photoémission résolue en angle (ARPES), nous observons des changements significatifs dans la structure électronique à 13 K, tels que des répliques de la SF et des repliements de bandes, signes clairs de la périodicité supplémentaire dans la phase d'ODC, qui dans certains cas peut conduire à l'ouverture d'un gap. Ces caractéristiques spectrales nous permettent d'identifier le vecteur d'emboîtement q et de proposer un modèle théorique pour la distorsion périodique du réseau.

Une autre manière de contrôler les propriétés électroniques des matériaux est par confinement quantique. Lorsque l'épaisseur du matériau est réduit à une échelle comparable à la longueur d'onde de Fermi, comme c'est précisément le cas dans les systèmes quasi 2D, les électrons sont alors confinés et des états de puits quantiques discrets apparaissent. Les dichalcogénures de métaux de transition étant quasi 2D, ils sont des matériaux favorables à l'étude du confinement quantique. Nous avons observé une série d'états de puits quantique sur différents échantillons de MoS_2 et nous avons étudié leur nature confinée en considérant leur dispersion k_z et les tendances de l'énergie de liaison de leurs états fondamentaux. Ces états sont également espacés en énergie, ce qui implique que le puits de potentiel à leur origine est plus doux que celui du puits quantique infini. Nous proposons que le confinement apparaît dans un assemblage découplé de quelques couches de MoS_2 au-dessus du cristal en volume, après l'exfoliation de celui-ci.

Enfin, l'inclusion de défauts dans la structure permet aussi d'ajuster les propriétés électroniques des matériaux quasi 2D. Nous avons étudié cet aspect dans le MoS_2 dans le cadre de la catalyse pour la réaction de dégagement de l'hydrogène (HER). Bien qu'il existe un consensus concernant l'amélioration de l'activité catalytique par que les lacunes de soufre (V_S), la densité optimale des lacunes n'était pas connue. Nous avons alors étudié la modification des propriétés électroniques en fonction du nombre de lacunes. Nous identifions les caractéristiques spectrales spécifiques à l'élimination du soufre, telles que des modifications de la queue de la bande de valence et des bandes S *p*. De plus, nous observons que même des faibles densités de lacunes jouent un rôle actif dans la dissociation et l'adsorption du H_2. En outre, nous observons que l'interaction de la surface avec H_2 dépend fortement de la pression d'exposition. En effet, l'hydrogénation à haute pression aboutit *in fine* à la métallisation de la surface. D'autre part, nous constatons qu'une densité élevée de défauts conduit à une surface inerte, probablement en raison d'une agglomération des défauts.

Title: Structural-induced modifications of electronic properties in low dimensional systems: transition-metal dichalcogenides and rare-earth diantimonides.

Keywords: ARPES, $LaSb_2$, charge density wave (CDW), MoS_2, quantum well states (QWS), hydrogen evolution reaction (HER).

Abstract: The advent of two-dimensional (2D) materials offers a unique platform for the study of solids at the atomic scale. However, the manipulation of 2D materials is complex and remains a drawback for which no practical solution has been found for the mass production of devices. Quasi-2D materials are easier to manipulate while sometimes retaining the essential properties of strictly 2D materials. This thesis presents three systems that illustrate how the electronic structure of quasi-2D materials can be modified by induced changes in the atomic structure.

Quasi-2D materials are susceptible to Fermi surface (FS) instabilities, which can induce phase transitions. In this context, the linear magnetoresistance of $LaSb_2$ has been explained by a possible charge density wave (CDW). Indeed, the anisotropic structure of $LaSb_2$ gives rise to a low-dispersion FS in k_z with regions favourable to nesting. Using angle-resolved photoemission spectroscopy (ARPES), we observe significant changes in the electronic structure at 13 K, such as FS replicas and band folding, clear signs of additional periodicity in the CDW phase, which in some cases can lead to gap opening. These spectral features allow us to identify the nesting vector *q* and propose a theoretical model for the periodic distortion of the lattice.

Another way of controlling the electronic properties of materials is by quantum confinement. When the thickness of the material is reduced to a scale comparable to the Fermi wavelength, as is precisely the case in quasi-2D systems, the electrons are confined and discrete quantum-well states (QWS) appear. As transition metal dichalcogenides (TMD) are quasi-2D, they are favourable materials for studying quantum confinement. We have observed a series of QWS on different MoS_2 samples. We have studied their confined nature by considering their k_z dispersion and the binding energy trends of their ground states. These states are also equally spaced in energy, implying that the potential well at their origin is softer than that of the infinite quantum well. We propose that confinement arises in a decoupled MoS_2 few-layer assembly on top of the bulk crystal after exfoliation.

Finally, the inclusion of defects in the structure also makes it possible to adjust the electronic properties of quasi-2D materials. We have studied this aspect in MoS_2 in the context of catalysis for the hydrogen evolution reaction (HER). Although there is a consensus that sulphur vacancies (V_S) improve catalytic activity, the optimum density of vacancies is unknown. We therefore studied the modification of the electronic properties as a function of the number of vacancies. We identify spectral features specific to the elimination of sulphur, such as changes in the tail of the valence band and the S *p* bands. Furthermore, we observe that low vacancy densities play an active role in the dissociation and adsorption of H_2. We also observe that the interaction of the surface with H_2 depends strongly on the exposure pressure. Hydrogenation at high pressure results in metallisation of the surface. On the other hand, we find that a high density of defects leads to an inert surface, probably due to agglomeration of the defects.

Título: Modificaciones de las propiedades electrónicas de sistemas de baja dimensionalidad inducidas estructuralmente: dicalcogenuros de metales de transición y diantimónidos de tierras raras

Palabras clave: ARPES, $LaSb_2$, onda de densidad de carga (ODC), MoS_2, estados de pozo cuántico, reacción de evolución del hidrógeno (HER).

Resumen: La llegada de los materiales bidimensionales (2D) ofrece una plataforma única para el estudio de los sólidos a escala atómica. Sin embargo, la manipulación de materiales 2D es compleja y sigue siendo un inconveniente para el que no se ha encontrado una solución práctica para la producción masiva de dispositivos. Los materiales cuasi-2D son más fáciles de manipular y, en ocasiones, conservan las propiedades esenciales de los materiales estrictamente bidimensionales. Esta tesis presenta tres sistemas que ilustran cómo puede modificarse la estructura electrónica de los materiales cuasi-2D mediante cambios inducidos en la estructura atómica.

Los materiales cuasi-2D son susceptibles a las inestabilidades de la superficie de Fermi (SF), que pueden inducir transiciones de fase. En este contexto, la magnetorresistencia lineal de $LaSb_2$ se ha explicado mediante una posible onda de densidad de carga (ODC). En efecto, la estructura anisotrópica de $LaSb_2$ da lugar a una SF poco dispersiva en k_z que presenta regiones favorables al anidamiento. Utilizando espectroscopia de fotoemisión resuelta en ángulo (ARPES), observamos cambios significativos en la estructura electrónica a 13 K, como réplicas de la SF y plegamiento de bandas, signos claros de la presencia de una periodicidad adicional en la fase CDW, que en algunos casos pueden conducir a la apertura de un *gap*. Estas características espectrales nos permiten identificar el vector de anidamiento *q* y proponer un modelo teórico para la distorsión periódica de la red.

Otra manera de controlar las propiedades electrónicas de los materiales es el confinamiento cuántico. Cuando el espesor del material se reduce a una escala comparable a la longitud de onda de Fermi, como ocurre precisamente en los sistemas cuasi-2D, los electrones quedan confinados y aparecen estados cuánticos discretos. Como los dicalcogenuros de metales de transición (TMD) son cuasi-2D, son materiales favorables para estudiar el confinamiento cuántico. Hemos observado una serie de estados de pozo cuántico en diferentes muestras de MoS_2. Hemos estudiado su naturaleza confinada considerando su dispersión k_z y las tendencias de la energía de enlace de sus estados básicos. Estos estados también están igualmente espaciados en energía, lo que implica que el pozo de potencial en su origen es más suave que el del pozo cuántico infinito. Proponemos que el confinamiento aparece en un conjunto desacoplado de unas pocas capas de MoS_2 sobre el cristal de volumen, después de su exfoliación.

Por último, la inclusión de defectos en la estructura también permite ajustar las propiedades electrónicas de los materiales cuasi-2D. Hemos estudiado este aspecto en MoS_2 en el contexto de la catálisis de la reacción de evolución del hidrógeno (HER). Aunque existe consenso en que las vacantes de azufre (V_S) mejoran la actividad catalítica, se desconoce la densidad óptima de vacantes. Por ello, estudiamos la modificación de las propiedades electrónicas en función del número de vacantes. Identificamos características espectrales específicas de la eliminación del azufre, como cambios en la cola de la banda de valencia y en las bandas S *p*. Por un lado, hemos observado que las bajas densidades de vacantes tienen un papel activo en la disociación y adsorción del H_2. También observamos que la interacción de la superficie con el H_2 depende en gran medida de la presión de exposición. La hidrogenación a alta presión provoca la metalización de la superficie. Por otro lado, observamos que una alta densidad de defectos da lugar a una superficie inerte, probablemente debido a la aglomeración de los defectos.

Acknowledgements

I would like to thank everyone who has been part of this *process*. Although my name is prominently featured on the cover, I have consistently felt that this work is a collective effort. This sentiment, viewing it as something shared, has been fostered by the passion and dedication that all those involved have poured into this project.

First and foremost, I express my gratitude to my advisors, Arantzazu Mascaraque and Antonio Tejeda. Standing atop this pinnacle of knowledge we have constructed, I can reflect and recognize the substantial growth I've experienced as a scientist. On numerous occasions, I find myself surprised by an inner voice that challenges the reasoning I am developing or attempting to comprehend. This **critical** voice often echoes yours, championing noble values such as pure scientific curiosity, rigour and honesty. However, I am aware that at times, this voice also contradicts and questions you. For both aspects, I am profoundly thankful to you. I understand that the ultimate objective of doctoral training is to nurture an autonomous individual, capable of critical analysis. In essence, thank you for consistently encouraging me to develop my *own* voice.

This *process* has taken place in two distinct locations: Madrid, Spain, and Orsay, France. Consequently, my expressions of gratitude are organized accordingly. In Madrid, within the Department of Materials Physics at UCM, my heartfelt thanks go to the Surface Physics and Nanostructures Group, which warmly welcomed me. I would like to extend special appreciation to Miguel Ángel González Barrio, for your generosity in dedicating time to enhance the ideas of this manuscript, enriching it significantly. Among all your virtues, I am deeply grateful to you for always offering me an honest and constructive opinion. I am also indebted to Álvaro González for his expertise in Python, developing code for the theoretical band structures plots presented in Chap.4 and Chap.5. Additionally, I want to acknowledge your support in spending long hours with me in the late-night sessions at the synchrotron. Lastly, within the group, I express my gratitude to Lucas Pérez and Óscar Rodríguez. Your consistent support has been indispensable.

Within the Department of Materials Physics at UCM, I extend my heartfelt gratitude to César González for his contribution. His theoretical calculations presented in Chap.4 and Chap.5 have immensely facilitated the interpretation of the results. Thank you for your invaluable assistance. I would also like to acknowledge Carlos Romero for his dedicated technical support. Your contribution has been greatly appreciated.

Still in Madrid, I would like to acknowledge Juan de la Figuera and José Emilio Prieto. I deeply appreciate your educational guidance in the field of electron microscopy. The work carried out at its LEEM has been of great help in characterising surface preparations. Thank you for your expertise and support.

In Orsay, France, I express my thanks to the permanent members of the LUTECE group: Vincent Jacques, David Le Bolloc'h, Luc Ortega, Olivier Plantevin, and Sylvain Ravy for their unwavering support. I want to extend special thanks to Olivier Plantevin for entrusting me with his experimental setup on numerous occasions. My gratitude also goes to the non-permanent members I had the privilege of working with during my time in Orsay, Abraham Campos and Lipin Chen. Abraham Campos, your willingness to share knowledge and explore the intricacies of ultra-high vacuum techniques together has been invaluable. To Lipin Chen, I extend my thanks for your theoretical calculations in Chap.3, which significantly complemented our measurement interpretation.

Within LPS, I owe a debt of gratitude to my *comité de suivi*, composed of Emmanuelle Rio and Fabrice Bert, for their invaluable time and mentorship provided year after year.

The *process* encompassed not only Madrid and Orsay but also several synchrotrons across the globe, including SOLARIS in Poland, ELETTRA in Italy, and SOLEIL in France. My sincere gratitude extends to all the staff at SOLARIS, especially Natalia Olszowska and Marcin Rosmus from the URANOS beamline, who provided support, allowing me to focus solely on the measurements. I am equally thankful to the staff at ELETTRA, with special mention to Jun Fujii from the APE_LE beamline, who consistently ensured our measurements ran seamlessly. Lastly, I express my appreciation to the SOLEIL staff, particularly Francois Bertran and Patrick Le Fèvre from the CASSIOPÉE line, for their invaluable assistance, significantly simplifying our tasks. Your support has been pivotal to the success of my work.

On a more personal note, I want to express my heartfelt gratitude to my colleagues in the office at UCM. Ana Parente, Laura Álvaro, Alejandra Guedeja-Marrón and Matilde Saura (the order is inconsequential because I appreciate each of you equally). Meeting all of you has been a wonderful experience, and I am deeply thankful for it. I can only hope that as you read these words in the future, you remember the way we perceived science and remain true to that vision. Doing things differently, although difficult, is possible. I wish that all the influence you exert (if you choose to continue) is harnessed to enhance the present. I look forward to being there to witness these positive changes. And if ever I fail in that purpose, I hope you'll be there to remind me of our shared ideals.

This journey would have been profoundly different if it weren't for Lidia Flores, my wife. I am deeply grateful for your endless emotional and material support. Your support has considerably lightened the burden that sometimes comes with doing science. Doing so, without giving up following your own path, is at least twice as hard. I'm very proud of you. Moving forward together, for our mutual benefit and the common good, has been (and still is) our greatest strength. I hope that this *process*, as it comes to an end, fills you with a sense of pride. I love you.

Lastly, I want to express my gratitude to my family and friends, even though they may never read these words. Thank you for putting in every conceivable effort to ensure I never stopped doing what I wanted, even when it meant taking my (our) studies lightly. Life's whimsy never ceases to amaze me, as in the end, studying just for the pleasure of knowledge turned out to be one of the most meaningful pursuits in my life.

Synthèse

Pendant près d'un siècle, le consensus scientifique dominant a nié la possibilité d'un ordre cristallin dans les matériaux unidimensionnels (1D) et bidimensionnels (2D). Ce paradigme a radicalement changé en 2004 lorsque A. Geim et K. Novoselov ont réussi à isoler des feuilles de graphène atomiquement épaisses, prouvant ainsi que les croyances établies étaient fausses. Cette avancée a déclenché une quête de matériaux similaires, conduisant à la découverte de nombreuses familles de matériaux 2D. Cette thèse passe en revue les dernières tendances en matière de matériaux 2D, commentant en détail les possibilités qu'ils offrent, ainsi que les difficultés de leur potentielle mise en œuvre. Nous soulignons en particulier comment les matériaux quasi-bidimensionnels sont plus faciles à manipuler et sont parfois capables de conserver certaines propriétés bidimensionnelles. Les matériaux quasi-2D sont constitués d'un nombre variable de couches 2D et se caractérisent par une liaison hautement anisotrope. Au sein de ces matériaux, les couches 2D sont fortement liées le long de la couche mais seulement faiblement liées aux couches adjacentes. Ainsi, un ensemble de structures 2D presque indépendantes composent le cristal 3D. Dans notre étude, nous tournons notre attention vers l'$LaSb_2$ et le MoS_2, des matériaux qui nous servent à illustrer comment l'induction de changements dans la structure atomique modifie la structure électronique des matériaux quasi-2D.

Pour élucider les changements induits dans les structures électroniques, nous avons utilisé la spectroscopie de photoémission à résolution angulaire (ARPES) basée sur le synchrotron. L'ARPES possède une capacité unique de mesurer directement les énergies et les impulsions des électrons et de remonter à partir de ces informations à la structure de bande. Cela fournit un aperçu sans précédent de la complexité des propriétés électroniques d'un matériau. L'ARPES est basé sur l'émission de photoélectrons depuis la surface d'un cristal irradié par la lumière (voir Fig.1a). Lorsqu'ils sont émis, ces électrons conservent des informations concernant l'énergie, l'impulsion et le spin à l'intérieur du solide. La détection de ces photoélectrons permet de reconstruire la structure de bande (voir Fig.1b). De plus, l'ARPES est non destructif et fonctionne dans des conditions d'ultravide, garantissant l'intégrité et la propreté des expériences.

Notre première cas d'étude est le $LaSb_2$, un membre de la famille des diantimoniures légers des terres rares. Le $LaSb_2$ a attiré une attention considérable en raison de sa magnétorésistance linéaire (MRL) non conventionnelle. Le mécanisme à l'origine du MRL est méconnu; cependant, il est supposé que la stabilisation des ondes de densité de charge (ODC) pourrait modifier la topologie de la surface de

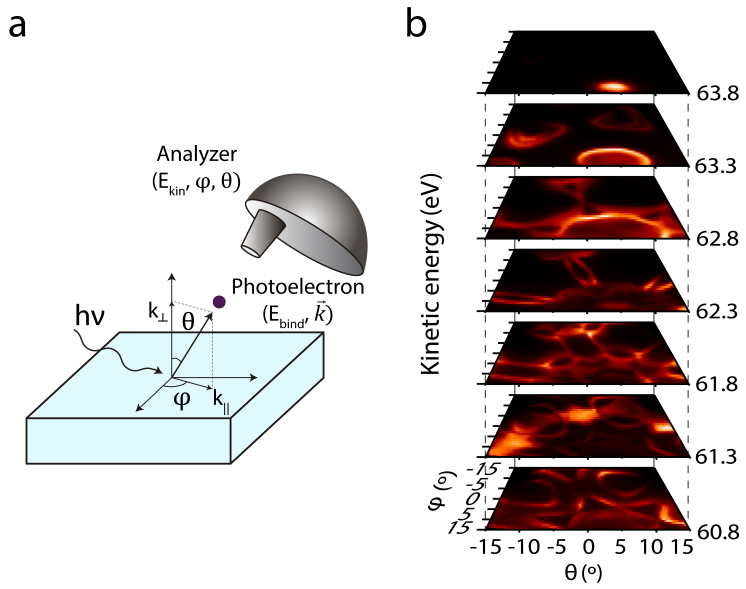

Figure 1: (a) Schéma de la photoémission résolue en angle (ARPES). Les observables mesurés grâce à l'analyseur (E_k, φ, θ) permettent de déterminer les propriétés des électrons à l'intérieur du solide (E_b, $\mathbf{k}$).(b) Cartes d'énergie constante du $MoSe_2$ à différentes énergies cinétiques montrant l'intensité ARPES dans le plan en fonction des angles polaires détectés (φ et θ). Les données ont été prises à 110 K et avec $h\nu = 70$ eV d'énergie de photon.

Fermi (SF), créant ainsi des régions espacées en raison d'une emboîtement imparfaite. Ces régions donnent naissance à de petites poches caractérisées par des courbures importantes dans les trajectoires des électrons, entraînant des modifications dans leur dispersion. Ce phénomène pourrait fournir une explication au MRL observé. Dans le $LaSb_2$, l'anisotropie de la structure atomique se traduit dans la SF par de feuilles parallèles de faible dispersion en k_z, lesquelles favorisent la stabilisation d'une éventuelle ODC par emboîtement. Pour explorer si une telle transition de phase existe, nous avons mesuré la structure électronique à 200 K et 13 K (voir Fig.2). Nous observons des changements significatifs à 13 K, tels que des répliques FS et le repliement des bandes, des indications claires de la présence d'une ODC (voir Fig.2b et c). Les changements dans la structure électronique à basse température sont liés à un vecteur d'emboîtement *q* ($q = 0,25 \pm 0,02$ Å^{-1}) le long de la direction $\overline{\Gamma Y}$ qui relie les régions de la SF *en forme de lunettes* du FS. Ensuite, en utilisant DFT, nous modélisons une périodique du réseau (PLD par son acronyme en anglais) par un déplacement de 0,02 Å le long de la direction *b'* de tous les atomes au sein d'une supercellule de taille 3*b'*. Le modèle apparaît comme le PLD le plus probable accompagnant l'ODC car il reproduit assez bien le repliement des bandes expérimentales et la redistribution du poids spectrale expérimentale.

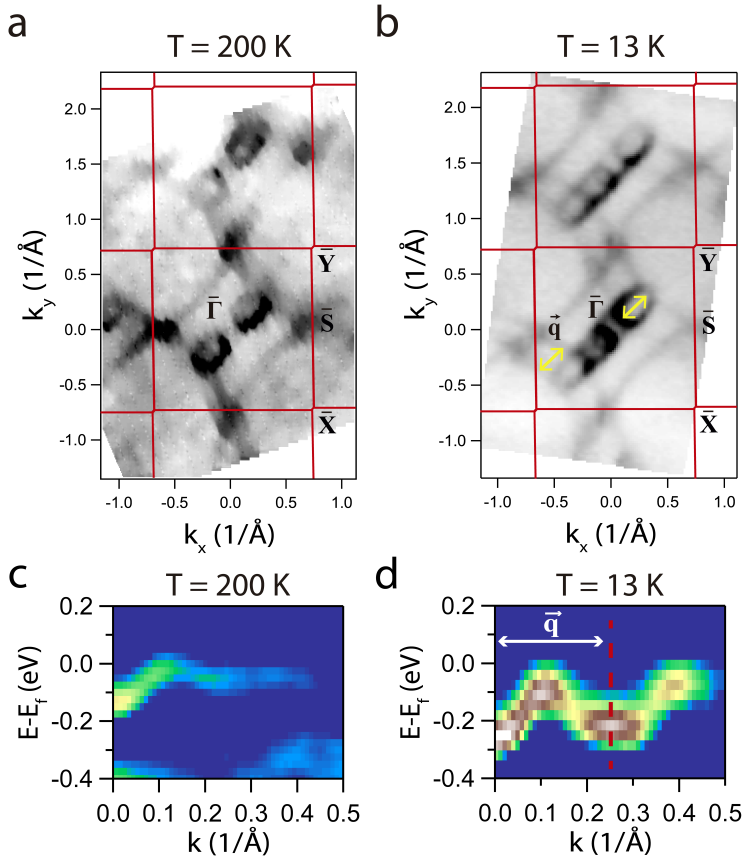

Figure 2: Cartographie expérimentale de la surface de Fermi de $LaSb_2$, obtenue à partir de l'intensité ARPES au niveau de Fermi en fonction des vecteurs k_x et k_y. Les panneaux présentent les première et deuxième zone de Brillouin. Mesures effectuées à (a) T = 200 K et (b) T = 13 K et prises avec $h\nu = 118$ eV d'énergie de photon. Structure de bande le long de la direction de haute symétrie $\overline{\Gamma Y}$ à (c) 200 K et (d) 13 K. Le repliement de la bande est visible sur (d).

Par la suite nous avons étudié le MoS_2, un système paradigmatique des dichalcogénures de métaux de transition (TMD). Nous avons y observé comment le confinement quantique permet de modifier la structure électronique. Lorsque l'épaisseur du matériau est réduit à une échelle comparable à la longueur d'onde de Fermi, les électrons sont quantifiés, donnant naissance à des états de puits quantiques (QWS) discrets. La réduction de l'épaisseur après exfoliation mécanique peut être relativement facile à réaliser en MoS_2, en raison de la faible liaison intercalaire de Van der Waals. Nous observons une série de QWS, sur différents échantillons MoS_2, situés sous le maximum de la bande de valence à $\overline{\Gamma}$ (voir Fig.3a-b). Leur nature confinée est étudiée en mesurant l'absence de dispersion k_z et l'évolution de l'énergie de es tendances énergétiques de liaison des états fondamentaux ($n = 1$). Fait intéressant, nous avons constaté que les QWS sont équiespacés, montrant une différence d'énergie constante entre les états n et $n + 1$. Cette situation indique

que le potentiel à l'origine des QWS est plus doux que celui du modèle de puits quantique infini. Nous proposons que le confinement apparaît dans un assemblage de quelques couches au sommet du cristal massif et découplé de celui-ci après exfoliation mécanique (voir Fig.3c). Nos résultats mettent en évidence comment il est possible d'ajuster l'énergie des niveaux, dans le cas du MoS_2.

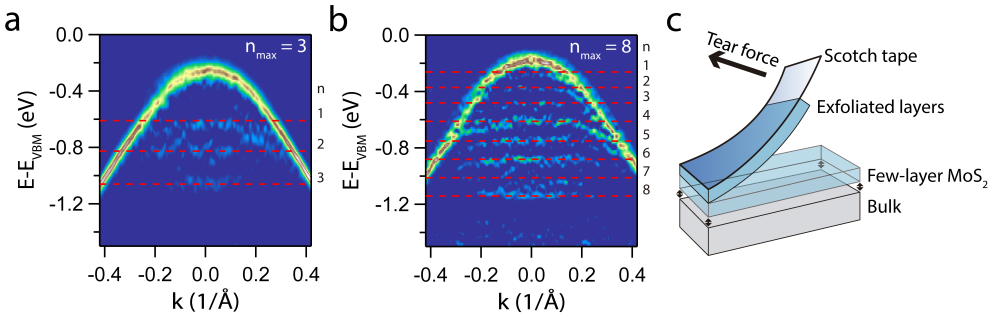

Figure 3: Dispersion parabolique convexe autour de $\overline{\Gamma}$ le long de la direction $\overline{\Gamma K}$, pour différents échantillons MoS_2. (a-b) $n_{max} = 3, 8$, respectivement. Les données ont été prises avec une énergie de photon de $h\nu = 70$ eV, en conservant la même géométrie expérimentale. (c) Représentation schématique de l'exfoliation dans un matériau vdW. Pendant le processus d'exfoliation, plusieurs couches adhèrent au ruban. Cependant, en raison de la faible liaison entre les couches de vdW, la force appliquée peut entraîner le détachement d'un ensemble de quelques couches du substrat.

Enfin la thèse étudie comment la structure électronique du MoS_2 peut être adaptée en introduisant des défauts structurels dans le cristal. Le MoS_2 est un matériau durable pour la réaction de catalyse de dégagement d'hydrogène (HER, selon son acronyme en anglais), une réaction clé pour la production d'hydrogène propre. Cependant, bien qu'il existe un consensus sur l'inclusion de défauts monosoufre (V_S) pour augmenter son activité catalytique, il n'y a pas d'accord sur la quantité de V_S à introduire pour optimiser le HER. En effet l'augmentation de la densité de V_S pourrait compromettre l'activité intrinsèque de chaque V_S, limitant le HER. Pour éclaircir cette question, nos travaux visent à établir une corrélation entre les structures atomiques et électroniques, y compris les défauts dus à l'adsorption d'hydrogène. Premièrement, nous induisons des défauts sur des surfaces MoS_2 grâce à des méthodes in situ, telles que le recuit sous ultravide et le bombardement ionique avec de l'Ar^+ à faible énergie. Nous identifions des caractéristiques spectroscopiques liées à l'élimination du soufre sur la bande de valence (BV), telles que des modifications de la queue de la bande de valence et des bandes S *p* (voir Fig.4a). De plus, nos résultats sur les interactions entre les défauts et l'hydrogène démontrent qu'une faible densité de V_S exposée à une hydrogénation à haute pression stimule la dissociation et l'adsorption de H_2 (voir Fig.3b-c). Dans ces conditions, nous observons la métallisation de la surface (initialement semiconductrice), un déplacement vers le bas du BV de type n de 0,17 eV et le rétablissement de l'ordre cristallin perdu après l'introduction de défauts (voir Fig.

3d-e). Ces résultats démontrent qu'une faible densité de défauts dans le MoS2 améliore l'absorption d'hydrogène sur la surface.

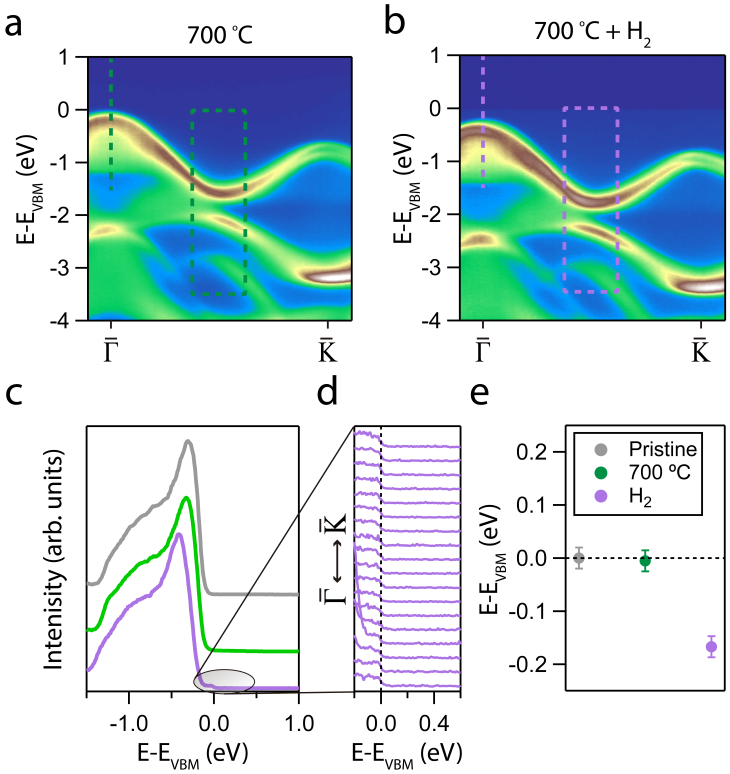

Figure 4: Intensité ARPES montrant l'évolution de la dispersion MoS_2 le long de la direction $\overline{\Gamma K}$ après (a) recuit de 700 °C, (b) après hydrogénation. Les lignes pointillées vertes et violettes indiquent où les profils montrés en (c) ont été effectués. (c) Profils centrés sur $\overline{\Gamma}$. (d) Zoom des profiles le long de $\overline{\Gamma K}$ montrant la métallisation de la surface après hydrogénation. (e) Bilan de la variation du VBM après chaque traitement de surface.

Contents

1 Introduction **19**

1.1 2D materials landscape . . . 20

1.1.1 The graphene family . . . 20

1.1.2 Transition metal dichalcogenides . . . 21

1.1.3 Layered materials . . . 22

1.1.4 Non-van der Waals materials . . . 24

1.2 Recent advantages and new directions . . . 24

1.3 Outline . . . 27

2 Experimental methods **29**

2.1 Photoemission Spectroscopy . . . 29

2.1.1 Overview . . . 29

2.1.2 Theoretical description: The three-step model . . . 31

2.1.3 Electron momentum . . . 34

2.1.4 Interpretation of a photoemission spectrum: the spectral function . . . 36

2.2 Acquiring and analysing an ARPES spectrum . . . 38

2.2.1 Light sources: synchrotron beamlines . . . 39

2.2.2 The electron analyser: angle detection . . . 42

2.2.3 Data analysis: methods and procedures . . . 43

2.3 Sample preparation methods . . . 44

2.3.1 Lanthanum diantimonide: $LaSb_2$ . . . 44

2.3.2 Transition-metal dichalcogenides: MoS_2 . . . 45

3 A CDW transition in $LaSb_2$ **49**

3.1 CDW phases in quasi-2D materials . . . 51

3.1.1 CDW in $LaSb_2$ related layered compounds . . . 52

3.2 Direct observation of a CDW transition . . . 53
3.2.1 Fermi surface . . . 53
3.2.2 Band structure . . . 55
3.3 Theoretical model of the PLD . . . 59
3.4 Conclusions . . . 62

4 Novel quantum well states in MoS_2 63

4.1 Crystalline structure . . . 64
4.1.1 Doping . . . 65
4.2 Electronic structure . . . 67
4.2.1 Valance band . . . 67
4.2.2 Core-levels . . . 73
4.3 Quantum well states . . . 75
4.4 Conclusions . . . 80

5 Boosting MoS_2 hydrogen adsorption 83

5.1 Hydrogen evolution reaction . . . 85
5.2 MoS_2 catalytic centres . . . 87
5.2.1 Molybdenum edges . . . 87
5.2.2 Basal plane . . . 88
5.3 Producing defects on the basal plane . . . 90
5.3.1 Annealing & low-energy ion sputtering . . . 90
5.3.2 Valence Band evolution . . . 91
5.3.3 Interaction of hydrogen with surfaces containing defects . . . 97
5.4 Conclusions . . . 101

6 Conclusions and perspectives 103

6.1 Conclusions . . . 103
6.2 Perspectives . . . 105

A Appendix **107**

A.1 Details of the DFT calculations for $LaSb_2$ 107

A.2 EDCs normalisation and EDCs overlapping representation 107

A.3 Details of the DFT calculations for MoS_2 108

List of abbreviations **111**

Bibliography **113**

1 - Introduction

It was not always believed that isolated two-dimensional (2D) materials had any chance of existing. Almost a century ago, through various arguments, Landau [1] and Peierls [2] both concluded the impossibility of crystalline order in one and two dimensions. Based on the harmonic crystal approximation, Peierls [2] demonstrated that a particle's mean-square displacement from its equilibrium position should grow infinitely in the thermodynamic limit. In essence, thermal fluctuations at finite temperatures would produce atom displacements large enough to compromise the long-range order and structural stability of a low-dimensional crystal.

Over the years, efforts have been made to challenge these ideas put forth by Landau and Peierls [3, 4], as well as to consolidate them [5–7]. However, the acceptance of theoretical works in favour of consolidation and the experimental observation of a decrease of the melting point with decreasing thickness [8] reinforced the notion of the impossibility of low-dimensional crystals and made it prevalent until a few years ago.

The impossible became possible in 2004 when Novoselov et al. [9] reported, for the first time, the isolation and characterization of atomically thick graphene sheets at room temperature. Although the work of Novoselov et al. was a paradigm shift in recent physics, it should be noted that 2D structures as ultra-thin films and graphene have been known for some decades. Ultra-thin films include any material that has been thinned down to a few nanometers or atomic thickness (monolayer), regardless of its original crystalline structure. Ultra-thin films grown for instance with atomic layer deposition (ALD) [10] or molecular beam epitaxy (MBE) [11] have been present since the 1960s, driven by the development of vacuum techniques and constitute a widely used element in surface science. In contrast, 2D materials, such as graphene, specifically denote materials with inherent 2D crystalline structures. Graphene was first treated theoretically by Wallace [12] in 1930 and probably observed by Boehm et al. [13] in 1962. However, the resolution of the microscopes did not allow the identification of the number of layers. In 2001, reliable identification of a chemically prepared graphene sheet was carried out by Shioyama [14], but since the preparation method does not allow for precise control of the sheet, the work did not attract much interest. Given the context, the significance of the Novoselov et al. work lies in their use of a straightforward mechanical method for graphene isolation, their demonstration of individual sheet manipulation and their precise thickness identification. Catalyzed by the isolation of graphene, the scientific community experienced an intensive surge in 2D materials research. This pivotal moment marked the commencement of an era dedicated

to the exploration and understanding of various 2D materials.

1.1 . 2D materials landscape

The successful isolation of graphene sparked interest in investigating whether isolating other 2D materials was possible, leading to the discovery of several families of 2D materials. Fig.1.1 presents some of the most important 2D families that have been discovered. These materials share a common characteristic: strong bonding within individual 2D planes and weak (usually van der Waals (vdW) like) bonding between these planes. VdW forces are weak attractions between neutral atoms, which hold the 2D planes together when stacked to form thicker layered structures [15, 16]. It is the vdW bonding that ultimately allows for relatively easy isolation of individual macroscopic 2D layers from 3D lamellar structures by exfoliation.

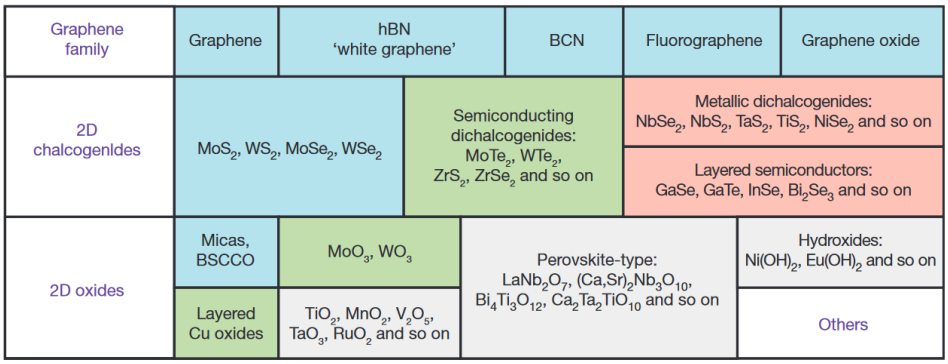

Figure 1.1: Library of 2D materials. The category *Others* includes different types of borides, carbides and nitrides. Table adapted from [16].

1.1.1 . The graphene family

The graphene family of Fig.1.1 includes materials whose thickness is strictly one atom. The realisation of relevant graphene-like materials of the group-IV such as silicene [17], germanene [18], stanene [19], plumbene [20] has been reported. Unlike graphene, layered forms of these materials are not available due to an energetically more favourable sp^3 hybridization than a planar sp^2 [21]. As a consequence, isolated free-standing layers cannot be obtained by exfoliation. However, they can be synthesized employing precise substrates and deposition processes for epitaxial growth and structure stabilization.

Materials from the graphene family have unique Dirac-like electronic band structures, characterized by a linear energy dispersion relation near the Fermi level. For instance, phenomena such as the anomalous quantum Hall effect [22], the

fractional quantum Hall effect [23], Klein tunnelling [24], or the Berry phase [25], are only a few examples of the exciting physics that these materials have revealed. In particular, silicene and germanene are envisioned as 2D materials optimum for integration in the Si semiconductor industry. Stanene and plumbene, with the heavier atomic weights of the group, are predicted to be topological insulators with a spin-orbit coupling (SOC) induced gap of ~ 100 meV [26] and ~ 200 meV [27], respectively. The band gap sizes allow for topological properties, such as the spin quantum hall effect, to occur at room temperature. The graphene family is broader and includes systems with more than one element, such as hexagonal boron nitride (h-BN), whose alternating boron and nitrogen atoms form a honeycomb lattice. It is a suitable insulating material for deep UV photonics due to its ~ 6 eV band gap and is also used as an inert substrate for graphene [28].

Although the graphene family holds promising applications, the synthesis process is a major drawback for its implementation. Advancements in synthesizing graphene layers through chemical vapour deposition (CVD) have reached a level of quality comparable to mechanically exfoliated samples [29]. However, to preserve carrier mobility, graphene encapsulation is necessary, with h-BN being the optimal choice. The large-scale synthesis of h-BN is a current challenge for the implementation of graphene technologies [30, 31]. Owing to the substrate requirements, the implementation of 2D materials of group IV is even more complex. Current efforts are focused on reducing the substrate interactions since free-standing layers are required to not break the topological order [21].

1.1.2 . Transition metal dichalcogenides

The transition metal dichalcogenides (TMDs) are a family of materials that consist of layers of transition metal atoms (such as Mo, W, among others) sandwiched between two layers of chalcogen atoms (such as S, Se, or Te), forming a hexagonal lattice. The chemical formula is MX_2, where M represents a transition metal atom and X represents a chalcogen atom. These three layers are tightly bonded by covalent forces and do not separate during exfoliation. Therefore, both in the literature (and so in this study), when referring to a TMD layer, we encompass all three layers together.

Early studies concerning the dimensionality of TMDs used MoS_2 owing to the natural availability of samples with high crystalline quality. The work of Frindt [32], pioneering the thinning of bulk MoS_2 into several layers using the adhesive tape method in 1965. Also, the work of Joensen, Frindt, and Morrison [33] should be mentioned, in which the isolation of a single MoS_2 layer by Li intercalation is reported; however, it was not possible to provide microscopic evidence at that time. Research on TMDs started actively after the isolation of graphene [9]. The application of the knowledge acquired through the exfoliation of graphene led to

gaining rapid control of the number of layers in a TMD [15]. Layer control in TMDs is crucial since the bandgap size and position depend on the number of layers. In consequence, the electronic and optical properties are layer dependent [34, 35]. Furthermore, the electronic structure of MoS_2 is extremely sensitive to structural modifications. Part of this work is dedicated to modifying the structure of this material through defect engineering. Moreover, the possibility of combining different elements and crystalline structures results in materials with a rich set of electronic properties. For instance, TMDs can be found as insulators, semiconductors, semimetals, metals [36] and in more exotic phases such as superconductors [37], CDW [38] and Mott insulators [39]. The strong SOC in TMDs enables the exploration of electron quantum degrees of freedom, including spin, layer and valley pseudospins [40, 41].

1.1.3 . Layered materials

1.1.3.1 Quasi-2D materials

The observation of layer-dependent properties in TMDs indicates that low-dimensional physics extends beyond single-atom-thick structures. This observation not only paves the way for exploring novel 2D materials but also provides an opportunity to reevaluate existing materials from a fresh perspective. Instead of exclusively searching for single-atom-thick materials, the focus is shifting towards anisotropic materials that possess 2D or 1D substructures, regardless of their thickness, capable of exhibiting low-dimensional properties. Such materials are referred to as quasi-2D materials. The versatility of these materials is higher compared to pure 2D, as the isolation of a 2D layer is not a prerequisite, but is available when required.

To identify new materials under this paradigm, recent approaches involve methods like high throughput screening and data mining [42, 43]. Figure 1.2a schematically illustrates the screening processes used for identifying quasi-2D materials. This process involves evaluating the atomic bonds of 3D crystals to identify potential 2D substructures. Quasi-2D candidates are then sorted based on exfoliability criteria, assessing both intralayer and interlayer bond strengths. Candidates with low interlayer and high intralayer bonding are considered the best options. Fig. 1.2b shows the most common 2D crystalline substructures found when screening 3D crystals. Mounet et al. [42] point out that the number of 2D materials can increase to 1036 easily exfoliable materials and 789 potentially exfoliable materials. In this sense, the work of Frisenda et al. [44] provides an interesting insight that highlights the abundance of unexplored natural layered minerals. Numerous elements documented in this study have gone unnoticed, presenting an opportunity for future exploration and research.

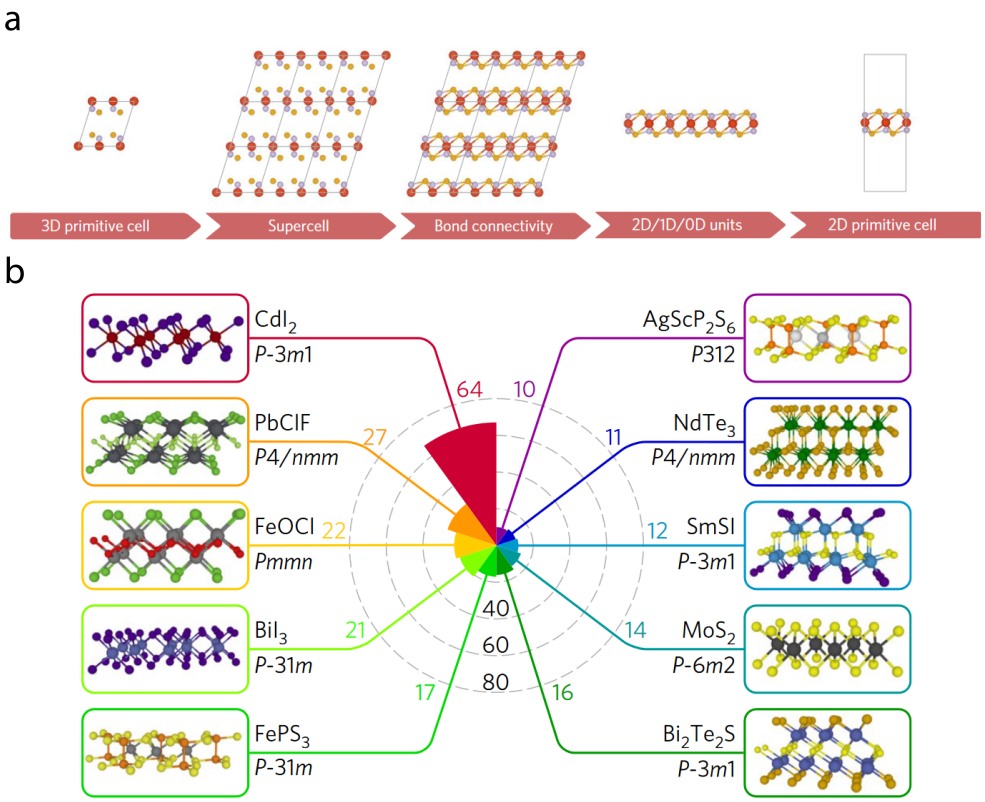

Figure 1.2: (a) Scheme showing the identification of low-dimensional units in a parent $MgPS_3$ three-dimensional crystal structures.(b) Polar histogram displaying the frequency of the top ten most common 2D structural prototypes. Each prototype is accompanied by its parent structure-type formula and the space group of the respective 2D prototype. Images adapted from [42].

1.1.3.2 Examples of layered materials

Some examples of layered material families in which the 2D substructure plays a key role are included in Fig.1.1. For instance, the high-temperature superconducting copper oxides (cuprates) are included since their structure hosts a series of 2D lattices formed by copper and oxygen atoms in which superconductivity and related phenomena such as charge density wave (CDW) and pseudogap take place [45]. 2D perovskites are also included. In these materials the organic cations are sandwiched by the inorganic perovskite layers, causing strong quantum confinement in the out-of-plane direction. This confinement alters the electronic structure, leading to tunable bandgaps that make them suitable for optoelectronics in solar energy harvesting [46]. Another remarkable group of layered materials are the rare-earth diantimonides. These materials crystallize in a large orthorhombic cell that contains barely interacting 2D layers. This situation leads to a highly anisotropic transport that prompts 2D-related phenomena in the materials. For instance, $LaSb_2$, a

material under study in this work, shows an unusual 2D to bulk superconducting regime transition [47]. Also, owing to its layered structure, nesting-driven CDW has been proposed to occur in this material to explain its magnetoresistive behaviour [48]. Part of this work is devoted to exploring the nesting-driven CDW order in this material.

1.1.4 . Non-van der Waals materials

Strategies for the identification of quasi-2D materials, such as those described by Mounet et al. [42], have even more reaching potential if the latest advances in liquid-phase exfoliation (LPE) are taken into account. Until now, the exploration of 2D materials has been limited to those whose two-dimensional substructures were weakly bound by vdW forces. Recently, however, a new field has opened up that seeks to exfoliate the previously non-exfoliable, under the name of non van der Waals (n-vdW) materials [49–51]. Candidates having 2D sub-structures bonded covalent or ionic bonds can be isolated by LPE using an adequate solvent. According to Balan et al. [49], the LPE of n-vdW solids yields a distribution of thin layers whose preferential orientation matches with the crystalline slip planes. This observation allows defining the cleavage planes as the planes along which exfoliation is most likely to occur. It has been found that when a 3D n-vdW crystal has more than one cleavage plane, the probability of cleavage through a given plane depends on the plane atomic packing factor; exfoliation is more likely in densely packed planes.

Another important aspect of n-vdW solids has to do with the existence of dangling bonds which can lead to undesired surface activity and instabilities of the isolated 2D material. Part of vdW materials stability comes from the absence of these bonds. On the one hand, it is required to find a way to limit the dangling bond activity for applications that exploit the electronic properties of the material. On the other hand, the existence of dangling bonds and surface activity can result beneficial for catalytic applications. The inherent instability of the n-vdW 2D can lead to a non-negligible existence of uncoordinated atoms in the form of defects or grain boundaries that greatly benefit the catalytic activity.

1.2 . Recent advantages and new directions

From a fundamental standpoint, the transition from 3D to 2D implies crossing a critical threshold where quantization and electron correlation become dominant. The dimensionality reduction breaks down the non-interacting framework used to describe electron dynamics [52]. In a 3D solid, the non-interacting framework is assumed because electrons have plenty of room to move around and screen the

electric field they generate (Coulomb screening). In 2D materials, electrons are restricted from moving perpendicular to the plane of the material by the positive charge of lattice ions. This restriction leaves the electric field unscreened, forcing electrons to interact electrostatically with each other. Consequently, correlations are inherent to 2D materials, giving rise to novel and collective quantum phenomena [53].

In practice, strategies such as regulating the number of layers, combining layers of different materials, functionalising surfaces, applying gate potentials, and inducing strain are frequently employed to uncover novel phenomena. Simultaneously, efforts are underway to develop scalable synthesis methods, integrate these materials into existing technologies, and explore applications in fields like electronics, optoelectronics, energy storage, and quantum technologies. In this context, we would like to emphasise the following areas of interest.

Spin-valley-layer coupling: 2D materials allow the exploration of different electron quantum degrees of freedom not available in their 3D counterparts. One such degree of freedom is the valley pseudospin. The valley degree of freedom emerges in hexagonal crystals, such as TMDs, when the symmetry between the band edges at the K points is broken due to the lack of inversion symmetry. This leads to the presence of non-equivalent K and K' valleys. In TMDs, which inherently have a non-centrosymmetric structure, this condition is met. Furthermore, the strong SOC in TMDs ensures spin-valley correlations. When inversion symmetry is broken, electrons in the two valleys exhibit finite orbital contributions to their magnetic moments, which are of equal magnitude but have opposite signs due to time-reversal symmetry [41, 54]. Resulting in unique valley-related phenomena such as valley optical selection rules, the valley Hall effect, and valley Zeeman splitting [55–57]. Current trends in pseudospin manipulation aim to replace dynamic methods of pseudospin control, such as optical pumping, with static methods like gating or layer stacking [58]. As an example of the latter, the persistence of spin-polarized states, observed even in bulk TMDs [59, 60], suggests that when the SOC is stronger than the interlayer coupling, layers can be assumed as decoupled, maintaining valley contrast [61].

Tuning properties in VdW heterostructures: Unlike traditional heterostructures, which are formed through strong covalent bonds, vdW heterostructures can assembled layer by layer due to the absence of dangling bonds. This makes it possible to combine several 2D materials regardless of their lattice mismatch or crystal structure. Combining layers with different lattice parameters or rotating stacked layers of the same material allows for adjusting the periodicity of the heterostructure and tailoring its band structure. On this basis, a wide range of captivating phenomena has been unveiled in 2D heterostructures such as moiré superconductivity [62], moiré excitons, Mott insulator states [63], or a Wigner crystal [64].

Among these phenomena, moiré superconductivity stands out as particularly intriguing. This effect has been observed in twisted bilayer [62], twisted trilayer [65] and up to twisted pentalayer graphene [66]. The layer misalignment due to the twist creates a moiré pattern with a spatial period much larger than the atomic unit cell. The resulting band structure, due to this new periodicity, exhibits flat-band regions near the Fermi level in some cases, leading to enhanced correlations. Furthermore, because the electron filling is highly sensitive to the twist angle, it can be used to shift the material's phase across a broad range of electronic regimes owing to the presence of flat bands near the Fermi level. However, presently, the underlying mechanism of moiré superconductivity remains unclear [67].

2D magnetism: Long-range magnetism in 2D depends on the spin dimensionality, a parameter describing the number of spin components [68]. Unlike in 3D materials, magnetism in 2D materials is only possible when the spins have one single component and, thus, are described by the Ising model, i.e., spins oriented perpendicular to the plane (an orientation possible due to strong SOC and magneto-crystalline anisotropy). Onsager's solution to the Ising model proves that magnetic order exists at finite temperatures. For spin ordering different from the Ising model, such as the isotropic Heisenberg model, where spins have no constraints, the Mermin-Wagner-Hohenberg theorem forbids magnetic long-range order at finite temperatures. 2D magnetism was observed for the first time in vdW materials such as CrI_3 [69] and $Cr_2Ge_2Te_6$ [70]; the study of these systems opened the gate for an increasing number of vdW 2D magnets [71]. Although the field of vdW magnets is relatively young, the search for 2D magnets in n-vdW materials has gained significant attention in recent years [72, 73]. This early search is justified owing to the limitations of vdW magnets, such as poor stability under ambient conditions, low Curie temperatures and a limited number of vdW structures compared to all known crystals [42]. In this regard, Puthirath Balan et al. reported achieved by LPE 2D sub-structures of bulk hematite and ilmenite, both materials coming from the mineral ore. The sub-unit cells, called hematene [74] and ilmenene [72], exhibit ferromagnetic order at room temperature.

New catalytic approaches: The significance of 2D materials in heterogeneous catalysis lies in their unique ability to tune both structural and electronic properties. The high surface area of 2D materials provides more active sites for catalytic reactions, enhancing their catalytic efficiency. Consequently, 2D materials have been instrumental in the development of highly efficient and selective catalytic systems for crucial processes like hydrogen evolution, oxygen reduction, water splitting (WS), and carbon dioxide reduction [75–78]. Over the past decade, extensive research has been conducted on catalysis in graphene and single-layer TMDs [79]. However, despite gradual progress in synthesis methods [29], the harsh conditions required for catalysis significantly limit the potential of purely 2D materials. Utilizing quasi-2D structures offers two main advantages: stability under

harsh conditions and the ability of interlayer interactions to create additional active sites, both on the material surface and in the interlayer region where reactants can be intercalated and subjected to confinement modulations [80].

In the context of the hydrogen evolution reaction (HER), a process thoroughly studied in this work, emerging materials like MXenes (a family of layered transition metal carbides, nitrides, and carbonitrides) [81] and selected non-van der Waals (n-vdW) materials (such as Co_3O_4 and hematene) [49] are gaining prominence due to their exceptional electrical conductivity, a characteristic challenging to find in other 2D materials. However, as discussed in the following, MoS_2 remains the leading candidate to replace the platinum group metals (PGM) in the HER given its wide availability, low cost and relatively environmentally friendly manufacture.

1.3 . Outline

In this work, our focus is on $LaSb_2$ and MoS_2, both quasi-2D systems serving as unique playgrounds for manipulating electronic properties through induced atomic structural changes. The manuscript is structured as follows:

Chapter 2: "Experimental Methods" offers a detailed account of angle-resolved photoemission spectroscopy (ARPES), the technique extensively utilized in this work for exploring the electronic structures of $LaSb_2$ and MoS_2. This chapter provides a historical perspective on the development of the technique, delves into its theoretical foundations, introduces the synchrotron lines used in this thesis, and presents the methods for sample preparation and data analysis.

Chapter 3: "A CDW Transition in $LaSb_2$" initiates presenting the observation of anomalous behaviours in $LaSb_2$, such as a wide superconducting transition and linear magnetoresistance (LMR). Considering the significance of LMR in condensed matter, this chapter explores proposed LMR mechanisms. It then presents experimental results, including Fermi surface (FS) and band structures at 200 K and 13 K, identifying a CDW phase at 13 K. Subsequently, a theoretical model for the periodic lattice distortion (PLD) associated with the CDW is introduced.

Chapter 4: "Novel Quantum Well States in MoS_2" begins by introducing MoS_2 crystalline polytypes and discussing sample doping specifics. It subsequently delves into key concepts related to experimental and theoretical electronic structures. Both, doping and electronic structure discussions serve as a foundation for this and the following chapters. The chapter concludes with the identification and elucidation of novel quantum well states (QWS) in MoS_2.

Chapter 5: "Boosting MoS_2 Hydrogen Adsorption" contextualizes MoS_2 as

a catalytic material for the HER. It reviews HER mechanisms, emphasizing the importance of the hydrogen intermediate in the process. The catalytic centres of MoS_2 are then presented, focusing on the basal plane centres. The chapter details the experimental strategy for inducing defects in the basal plane using annealing and low-energy ion sputtering (LEIS). A comparative study of the electronic structure evolution after defect introduction using both methods is conducted. Finally, samples containing defects are dosed with hydrogen to gain insights into the hydrogen-defect interaction, discussing the influence of defect density and dosing pressure on the dissociative adsorption of hydrogen.

Chap.6: "Conclusions and perspectives" synthesizes the conclusions drawn in the thesis. It then presents an overview of the lines of work that are still open, showing their status as well as the expected results.

2 - Experimental methods

This chapter provides an in-depth exploration of the experimental methods utilized to investigate structural modifications within the materials under study in this work. It offers historical context by tracing the development of the photoemission technique and delves into the theoretical framework underlying the photoemission process. Subsequently, the chapter presents the core components of the experimental approach, such as the synchrotron beamlines employed, the operational principles of the spectrometer, methodologies for data analysis, and techniques for preparing samples. The objective is to provide readers with a complete grasp of the current state of the photoemission technique.

2.1 . Photoemission Spectroscopy

2.1.1 . Overview

The terms photoemission or photoelectron spectroscopy (PES) encompass a wide range of experimental methods that have their roots in the photoelectric effect [82–84]. In 1887 Heinrich Hertz carried out an experiment in which a pulse travelling along a circuit eventually generated a spark between two separate metal spheres. Thus, experimentally demonstrating Maxwell's electromagnetic theory by witnessing the formation of electromagnetic waves.

During the course of his experiment, Hertz made an intriguing observation – the intensity of the spark he generated appeared to be linked to the intensity of the light source he used. A noteworthy aspect was that the spark's size notably diminished when he repeated the experiment in complete darkness. This suggested a significant connection between light and the spark phenomenon. Despite the importance of this discovery, Hertz did not proceed to formalize or provide a detailed explanation for these observations at that time.

Some years later, following the experiments of J. J. Thompson in 1899, P. von Lenard made a notable observation during these studies. When ultraviolet radiation impinged upon one of the electrodes enclosed within an evacuated glass tube, an electric current began to flow through the setup. This current, however, ceased its flow as soon as the supply of ultraviolet radiation was cut off. This pivotal observation marked the genesis of the concept now known as photoelectric emission.

Furthermore, he observed that the kinetic energy of the electrons composing the photocurrent was not influenced by the intensity of the light source. Instead, he noted a clear increase in the kinetic energy of electrons with the frequency of the light. This discovery challenged the well-accepted relationship between energy flux and intensity, as described by the Poynting vector, thereby underscoring a significant gap in the understanding of light-matter interaction.

During his *annus mirabilis* A. Einstein published a description of the photoelectric effect that will settle the foundations of the quantum theory. The breakthrough assumption was that light energy distribution is made up of discrete energy quanta rather than being a continuum. Only in this way, it was possible to elegantly explain the previous photoelectric evidence by the following expression:

$$E_k = h\nu - \Phi - E_b \tag{2.1}$$

Where E_k is the kinetic energy of the electrons coming out from the material, $h\nu$ is the photon energy of excitation with h the Planck's constant and ν the frequency of the incident light, Φ is the material work function (a surface's potential barrier that prevents electrons from escaping) and E_b is the binding energy (for a solid is referred as the energy difference between the considered electron energy level and the Fermi level; for free atoms or molecules, to the vacuum level). Eq.2.1 is a milestone in the foundations of quantum mechanics. It implies a change in the mental paradigm of that time by establishing the idea that light, hitherto accepted as a continuum, is divided into quanta.

Nowadays, when examining Eq.2.1, the spectroscopic capabilities of the photoemission technique are immediately assumed. However, the establishment of the technique runs parallel to the development of the quantum theory. In this vein, the innovation of fixed energy photon sources in the X-ray and ultraviolet (UV) spectrum, as well as advancements in vacuum technology, promoted the availability of cleaner surfaces from which could be measured more precisely defined spectra. The outstanding contribution and development of the technique during the 60s was led by K. Siegbahn's group at Uppsala and W. Spicer at Stanford.

Given the resolution improvements in detectors, Siegbahn was able to distinguish photoelectrons from distinct oxidation states. This process, known as a chemical shift formed the basis for distinguishing between an element's various valence states [85]. Siegbahn proposed the Electron Spectroscopy for Chemical Analysis (ESCA) approach in light of the element-specific binding energies and chemical shift, resulting awarded with the 1981 Nobel Prize in Physics. Today ESCA is an outdated term, the scanning of electronic levels is now called X-ray photoemission spectroscopy (XPS).

Meanwhile, W. Spicer and colleagues measured the valence band (VB) of a metal for the first time in 1964. They also implemented the three-step model to describe the photoemission process [86, 87]. The decomposition of such a complex process in steps makes it extremely intuitive, yielding accurate results most of the time [87, 88].

Both schools among many others, laid the foundations of photoemission as an advanced spectroscopic technique. Since then photoemission has always been at the vanguard in the exploration of condensed matter phenomena. The following sections of this chapter will cover in detail the theoretical aspects of photoemission and present the current status of the technique.

2.1.2 . Theoretical description: The three-step model

Formally, the photoemission process consists of physically describing a many-body system after having interacted with a photon (Fig.2.1a). This task is extraordinarily complex and requires some legitimate approximations to tackle the problem. The three-step model greatly simplifies the process by artificially dividing the photoemission process into separated steps [87, 88]. The steps sequence is depicted in Fig.2.1b. Because of its utility, the three-step model is widely accepted. Although the one-step model is required for an accurate description of the photoemission process [89].

The steps of the model are detailed below:
1) Optical excitation. The first simplification consists of assuming an independent electron and disregarding the electronic correlations. Single-electron functions are therefore employed. In light of this, the probability of transition ($w_{f,i}$) for an optical excitation between an initial ($|\Phi_i\rangle$) and a final ($|\Phi_f\rangle$) monoelectronic state is given by the Fermi's golden rule:

$$w_{f,i} = \frac{2\pi}{\hbar}|\langle\Phi_f|H_{int}|\Phi_i\rangle|^2\delta(E_f - E_i - h\nu) \tag{2.2}$$

In this equation, the Dirac delta function reflects the energy conservation between the initial (E_i) and the final state (E_f), while $h\nu$ is the photon energy of excitation. H_{int} is the Hamiltonian of the optical interaction conveniently treated as a perturbation. Let H_0 be the Hamiltonian of an electron in the absence of external electric field, $H_0 = \frac{p^2}{2m} + V$, where p is the electron momentum, m the electron mass at rest and V the potential generated by other particles in the system. The derivation of H_{int} is obtained by inserting the vector ($\mathbf{A}$) and scalar (φ) potentials into H_0 so that the effects of an external electromagnetic field are included:

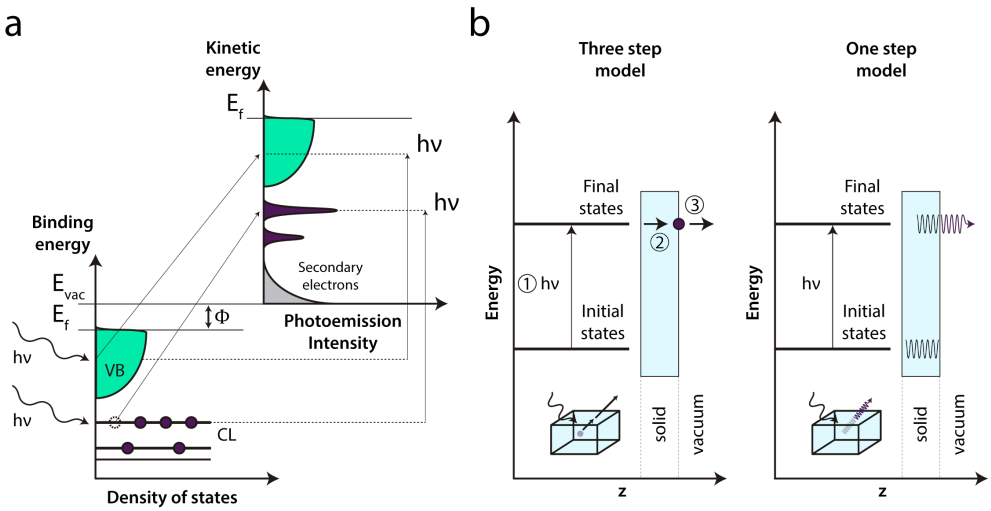

Figure 2.1: (a) Diagram of the relationship between the solid energy core-level (CL)s and VB and the distribution of photoelectrons. A photon with energy $h\nu$ extracts an electron from a state with binding energy E_b, following the energy conservation in Eq.2.1. Photoelectrons reaching the detector display a distribution related to the electronic states as a function of E_k. (b) Left, the three-step model. It consists of 1) Optical excitation, 2) Propagation of the photoelectron from the bulk towards the surface and 3) Escape of the photoelectron into the vacuum. Right, the one-step model. A solid's Bloch state is excited into a wave that propagates freely into the vacuum. This wave is attenuated within the solid. Initial, final and vacuum state wavefunctions must match simultaneously.

$$H = \frac{(\mathbf{p} - q\mathbf{A})^2}{2m} + q\varphi + V = \frac{p^2}{2m} - \frac{q}{2m}(\mathbf{A}\cdot\mathbf{p} + \mathbf{p}\cdot\mathbf{A}) + \frac{q^2}{2m}A^2 + q\varphi + V \\ = H_0 + H_{int} \tag{2.3}$$

The perturbation accounting for the optical excitation H_{int} can be simplified as:

$$H_{int} = -\frac{q}{2m}(\mathbf{A}\cdot\mathbf{p} + \mathbf{p}\cdot\mathbf{A}) + \frac{q^2}{2m}A^2 + q\varphi \\ = -\frac{q}{2m}(2\mathbf{p}\cdot\mathbf{A} + i\hbar\nabla\cdot\mathbf{A}) + \frac{q^2}{2mc}A^2 \approx -\frac{q}{m}\mathbf{A}\cdot\mathbf{p} \tag{2.4}$$

The following approximations have been considered to simplify H_{int}. First, the dipole approximation, since the excitation wavelengths employed in photoemission are larger than the inter-atomic distances. Thus, it is reasonable to assume a spatially homogeneous light field and consequently a constant vector potential, $\nabla\cdot\mathbf{A} = 0$. Also, possible variations in $\mathbf{A}$ due to the surface discontinuity at the interface are neglected in this approach. Secondly, the quadratic term of $\mathbf{A}$ can be dropped as it is only relevant at strong-field conditions (high photon intensities).

For instance, at a synchrotron, the samples are illuminated with typical photon flux values of 10^{14} ph./s/0.1%bw in a $100\mu\mathrm{m}$ x $100\mu\mathrm{m}$ area at 35 eV photon energy. Thus, yielding intensities ca. 10^4 W/cm^2 which are far below the strong-field conditions that occur around 10^{15} W/cm^2 [90]. Thirdly, selecting the Coulomb gauge as a work frame implies that $\varphi = 0$ [91]. Therefore, considering the above mentioned simplifications, Eq.2.2 can be expressed as:

$$\begin{aligned} w_{f,i} &= \frac{2\pi}{\hbar}|M_{f,i}|^2\delta(E_f - E_i - h\nu) \\ |M_{f,i}|^2 &= \frac{q^2}{m^2}|\langle\Phi_f|\mathbf{p}|\Phi_i\rangle\mathbf{A}|^2 \end{aligned} \tag{2.5}$$

the term $M_{f,i}$ is the photoemission matrix element. The element indicates that the electron-photon interaction induces a transition between the initial and a final monoelectronic state.

2) Propagation of the photoelectron from the bulk towards the surface. After the optical excitation the photoelectrons created in step 1) move in different directions. Those heading the surface are the ones with chances of escaping the solid. However, on their path, the electrons may scatter and change their momentum, losing the original information about the state where they come from (inelastic scattering). Among all the possible scattering interactions including those involving electrons, phonons, and plasmons, the electron-electron scattering stands out as the most dominant process.

The probability of an excited electron reaching the surface without experiencing any scattering event is determined by the inelastic mean free path (IMFP). The IMFP is mainly dependent on the electron's kinetic energy rather than being material-dependent. This dependence leads to the well-known "universal curve" [92]. The universality of the curve derives from considering a non-interacting electrons framework, which eliminates any material's feature. So, as a rule of thumb, the higher the kinetic energy the less time the electron stays in the solid and consequentially, the probability of having a scattering event is lower.

The analysis of the IMFP curve draws an important conclusion. Considering the typical excitation photon energies used in photoemission (below 1.5 keV), the origin of the elastically dispersed electrons that reach the surface can only be tens of an angstrom distance. As a result, photoemission is a surface-sensitive technique that requires atomically clean prepared surfaces within an ultra-high vacuum (UHV) environment to get high-quality spectra.

3) Escape of the photoelectron into the vacuum. once the photoelectrons reach the surface, only those with enough kinetic energy to overcome the material's

work function will effectively escape into the vacuum. This critical step is delineated in the following section.

2.1.3 . Electron momentum

When an electron leaves a crystal during a photoemission event, its exit direction from the surface normal is defined by the spherical angles φ and θ (see Fig.2.2a). In the technique called angle-resolved photoemission spectroscopy (ARPES), these two angles must be detected together with the kinetic energy of the photoelectron (see Fig.2.2b). These angles are related to the wavevectors within the solid. As a result, it is possible to reconstruct the electronic structure [93, 94].

Fig.2.2c shows the conservation of the parallel momentum when an electron crosses the interface between the solid and the vacuum. The energy in the vacuum measured by the detector is given by:

$$E_k = \hbar^2 k_{vac}^2 / 2m \tag{2.6}$$

When the electron crosses the interface the translational symmetry is preserved in the parallel direction, $k_{sol\parallel} = k_{vac\parallel}$. Thus, by simple geometrical considerations, it is possible to obtain:

$$k_{vac\parallel} = \sqrt{\frac{2mE_k}{\hbar^2}} \sin\theta \tag{2.7}$$

It is important to stress that the perpendicular momentum is not conserved due to the translational symmetry breaking (in the perpendicular direction), $k_{sol\perp} \neq k_{vac\perp}$. Nevertheless, the perpendicular momentum can be retrieved if the final state is parameterized as a free-electron dispersion offset by a potential, as it is represented in Fig.2.2d. This consideration leads to:

$$E_f(k) = \frac{\hbar^2 k_{sol}^2}{2m} - V_0 \tag{2.8}$$

V_0 is the inner potential, an average potential that electrons experience in the solid. Hence, following from this expression, the $k_{sol\perp}$ momentum can be expressed as:

$$\hbar^2 k_{vac\perp}^2 / 2m = \hbar^2 k_{sol\perp}^2 / 2m - V_0 \tag{2.9}$$

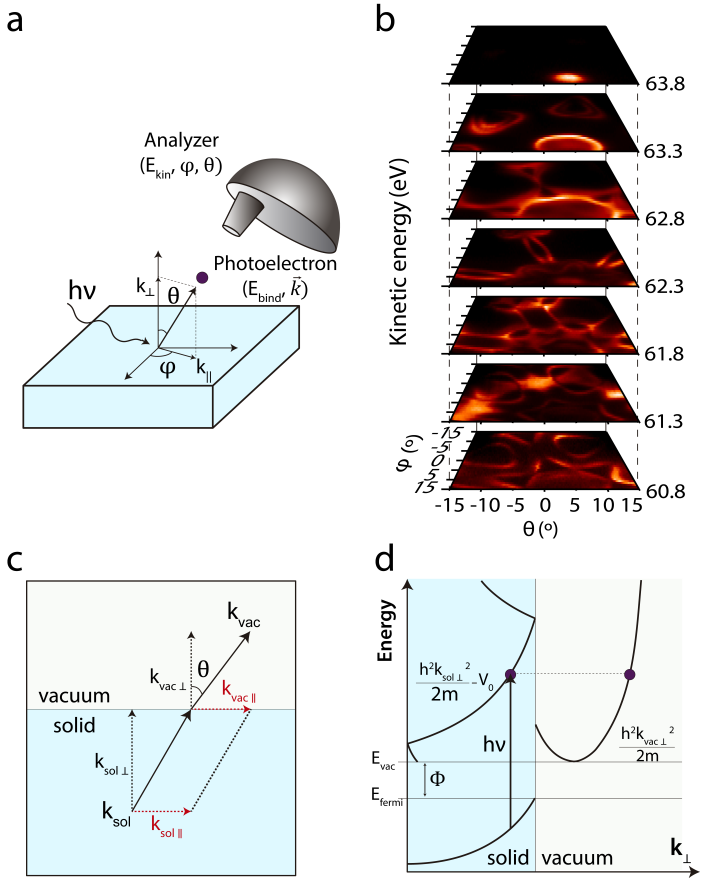

Figure 2.2: (a) ARPES experimental setup. The analyser observables (E_k, φ, θ) relate the photoelectron quantities (E_b, $\mathbf{k}$). (b) $MoSe_2$ CEMs at different kinetic energies showing in-plane ARPES intensity along the detected angles (φ and θ). Data was taken at 110 K and with $h\nu = 70$ eV photon energy. (c) Diagram showing the conservation of the parallel momentum between the solid momentum (initial) and vacuum momentum (final). The perpendicular momentum is not conserved. (d) Three-step model kinematics. A photon with energy $\hbar\nu$ excites an electron from an initial occupied state (with E_b) towards a free-electron dispersion state offset by the inner potential V_0. A band in the reduced zone scheme for the free electron approximation is shown in the diagram (blue region). The solid's work function Φ is a step potential that prevents the perpendicular momentum from being conserved at the photoelectron's surface transmission.

Recalling that $k^2_{vac\|} + k^2_{vac\perp} = k^2_{vac}$ and substituting with Eqs.2.6 and 2.7, the perpendicular momentum can be expressed as:

$$k_{sol\perp} = \sqrt{\frac{2m(E_k \cos^2\theta + V_0)}{\hbar^2}} \tag{2.10}$$

The inner potential value (V_0) is a priori an unknown parameter, however, well-known methods for its experimental determination are available [95]. For instance,

combining Eq. 2.1 and the periodicity along $k_\perp$:

$$E_b(k_{vac\parallel}, k_{sol\perp}) = E_b(k_{vac\parallel}, k_{sol\perp} + nG_\perp) \tag{2.11}$$

where n represents an integer and $G_\perp$ denotes a reciprocal lattice vector perpendicular to the surface. The strategy involves performing a photon energy scan covering at least one period in the $k_\perp$ direction. For instance, it is common to select the distance between two high-symmetry points ($\Delta k_{sol\perp} = nG_\perp$) as the range for the scan. At these points, the band structure typically experiences abrupt directional changes, aiding in precisely defining the positions of these points and their separation. The experimental $G_\perp$ determined this way is ill-defined given the V_0 uncertainty. However, the absolute value of $G_\perp$ is known from the lattice parameter. As a result, the value of V_0 can be determined by finding the value that matches the measured $G_\perp$ with its known absolute value.

Indeed, for the specific materials examined in this study, which are quasi-two-dimensional and layered materials, the precise determination of V_0 is not critical. The quasi-two-dimensional atomic structure guarantees little dispersion along the $\mathbf{k}_\perp$ direction. In practical terms, having a low dispersion in the $\mathbf{k}_\perp$ direction can be advantageous in experimental measurements, allowing measurements to be conducted using photon energies that are less affected by matrix element effects or have a higher photoionization cross-section, enhancing the signal-to-noise ratio and improving the quality of the collected spectra.

2.1.4 . Interpretation of a photoemission spectrum: the spectral function

Previously, the relationship between the ARPES spectrum and the band structure has been detailed. Nevertheless, the resulting spectrum is even richer and contains information relative to the many-body effects of the solid, i.e., it allows to characterize and quantify the electronic interactions. To interpret and unravel the spectrum's information, attention should be paid to Eq.2.5, from which the photoemission intensity can be estimated. To consider the system as a whole, the monoelectronic states defined above must be replaced by wavefunctions for an N electron system. Thus, we define the initial ground state ($|\Psi_i^N, 0\rangle$) and the possible final states ($|\Psi_f^N, s\rangle$). The final state can be expressed as:

$$|\Psi_f^N, s\rangle = K(|\varphi_\mathbf{k}\rangle \otimes |\Psi_f^{N-1}, s\rangle) \tag{2.12}$$

where K is an anti-symmetric operator, $\varphi_f^\mathbf{k}$ is a monoelectronic state of the photoelectron with momentum $\hbar\mathbf{k}$ (a free electron in the vacuum) and Ψ_f^{N-1} describes

the remaining N-1 system. This artificial decomposition is crucial and is known as the sudden approximation. Its validity holds under the assumption that the outgoing photoelectron is suddenly emitted at high enough kinetic energy so it does not interact with the N-1 remaining system.

Considering the second quantization formalism is useful in this context as it allows to easily deal with a system of N particles in which the number of particles varies. To account for particle variation the formalism employs the creation (a) and annihilation ($a^\dagger$) operators. Thus, Eq.2.12 can be expressed as:

$$|\Psi_f^N, s\rangle = K(|\varphi_{\mathbf{k}}\rangle \otimes |\Psi_f^{N-1}, s\rangle) = a_{\mathbf{k}}^\dagger |\Psi_f^{N-1}, s\rangle \tag{2.13}$$

and, following Eq.2.5, the total photoemission intensity $I = \sum_{s,k} w_{f,i}$ can be expressed as follows:

$$\begin{gathered} I(\mathbf{k}, E_k) = \sum_{s,k} \frac{2\pi}{\hbar} |M_{f,i}^{\mathbf{k}}|^2 \sum_m |\langle \Psi_f^{N-1}, s | a_{\mathbf{k}} | \Psi_i^N, 0 \rangle|^2 \delta(E_k + E_s^{N-1} - E_i^N - h\nu) \\ I(\mathbf{k}, E_k) = \sum_{f,i} \frac{2\pi}{\hbar} |M_{f,i}^{\mathbf{k}}|^2 \mathcal{A}^- \end{gathered} \tag{2.14}$$

By examining the photoemission intensity in the last expression we can note that the matrix element is modulating the second term, $\mathcal{A}^-$, the single particle removal spectral function. The modulation of the matrix element takes into account the nature of the optical excitation, i.e., photon energy and polarisation and the orbital character of the wavefunctions. On the other hand and within the Green function formalism $\mathcal{A}^-$:

$$\mathcal{A}^-(\mathbf{k}, w) = \sum_s |\langle \Psi_s^{N-1} | a_{\mathbf{k}} | \Psi_i^N \rangle|^2 \delta(w - E_s^{N-1} + E_i^N) \tag{2.15}$$

is related to the Green function as $\mathcal{A}^- = -(1/\pi)\mathrm{Im}\mathcal{G}(\mathbf{k}, w)$. The removal spectral function $\mathcal{A}^-$ expresses the probability, of the N-1 system, of changing the energy (w) when an electron with momentum k is removed. It is important to note that, due to Heisenberg's uncertainty relation, the particle's energy is distributed around a mean value. This distribution is precisely described by the spectral function. Indeed, the final state wavefunction results from the overlap of the s possible final states. The peak is no longer described by a delta but it consists of a broadened line together with satellites. From a spectroscopist perspective, a photoemission experiment ultimately probes the system's response to the sudden annihilation of

an electron, and thus, gives information about the collective excitations within the many-body system [84]. Rigorously speaking, these excitations conceptually differ from the actual band structure and only when the electronic correlations are weak a strict comparison between photoemission spectra and band structure calculations is feasible.

2.2 . Acquiring and analysing an ARPES spectrum

The technical aspects of measuring an ARPES spectrum will be covered in this subsection. A well-prepared sample, an excitation light source and an electron analyser are necessary for conducting an experiment.

The sample should meet strict cleanliness conditions since the signal (the photoemitted electrons) comes from the topmost part of the sample. Working under UHV ($\sim 10^{-10}$ mbar) guarantees a surface free from adsorbed residual species at least for the signal collection period (a few hours for an entire BZ survey). Ideally, the sample should be a single crystal with a flat-terminated surface. Before data collection, surface preparation techniques should be used to obtain atomically clean and well-ordered samples. The most common methods include mechanical exfoliation, annealing, ion-sputtering, etching, *in-situ* epitaxial growing. These methods seek to either remove the surface adsorbates, expose a fresh surface by peeling off the first layers or grow a clean surface directly in UHV conditions. A detailed description of the sample preparation methods employed in this work can be found at Sec.2.3.

About the photon sources, the extensively used ones are helium lamps, lasers and synchrotron radiation. The first two sources are home-lab-based solutions working at fixed photon energy, thus fixing $\mathbf{k}_{\perp}$. The use of synchrotron radiation as an excitation source has the advantage that it is possible to monochromatise its broad energy spectrum, allowing for precise photon energy tuning. As the experimental data of this thesis comprises exclusively the use of synchrotron radiation, a description of the used beamlines can be found at Sec.2.2.1.

Since the sample emits a large number of photoelectrons with varying kinetic energies and take-off angles, an electron analyser sensitive to these two parameters is needed. The working principles of photoelectron measurement with a hemispherical analyser are reviewed in Sec.2.2.2. Also, the procedures for analysing the resulting ARPES spectrum are presented in Sec.2.2.3.

2.2.1 . Light sources: synchrotron beamlines

A synchrotron light source is a close-loop particle accelerator used for radiation production. Most accelerators consist of three parts[1]: linear accelerator (*linac*), booster ring and storage ring. In the linear accelerator, electrons are created from a cathode and accelerated up to relativistic speeds (up to 99.99996 % of the speed of light).

At the end of the *linac* electrons enter into the booster ring. Within the booster ring, the electrons follow a loop pattern getting a boost in energy on each turn thanks to an accelerating radiofrequency cavity. The energy is increased from several hundreds of MeV (at the end of the linac) up to several GeV. Moreover, the booster ring allows the synchrotron to work in top-up mode. In this mode, the storage ring is periodically supplied with accelerated electrons to maintain a constant current.

In its final stage, the electrons are transferred to the storage ring loop. Here is where the phenomenon of synchrotron radiation is exploited. Bending the electron's trajectory leads to electromagnetic radiation emission, resulting in a remarkable photon beam with high brilliance (10^{20} photons/s/0.1%bw/mm^2/mrad^2), very broad emission spectrum (sub-eV up to the MeV), adjustable polarisation, high collimation and temporal structure (photon pulses of one nanosecond or lower). The ARPES experiments covered in this thesis use a variety of beamlines, each with unique characteristics. The diagram shown in Fig.2.3 captures the essential features of these beamlines, where the optics arrangement from the insertion device to the end station is similar to the beamlines described below.

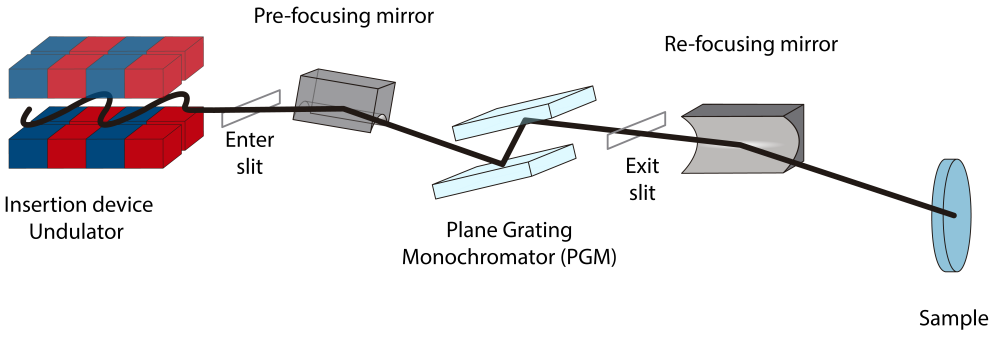

Figure 2.3: Scheme showing the arrangement of the optical elements composing a beamline. The insertion device modifies the trajectory of the electrons in the storage ring producing light towards the end station. A combination of mirrors and gratings focuses and monochromes the light. The light is finally directed to illuminate the sample in the analysis chamber.

[1]except SOLARIS (described below) which only has two parts: linear accelerator and storage ring.

2.2.1.1 SOLEIL synchrotron: CASSIOPÉE beamline

The SOLEIL synchrotron located in France is a 2.75 GeV electron ring, with a beam current up to 500 mA. It feeds the Cassiopée beamline, which works with photon energies between 8 to 1500 eV provided by two undulators, a HU256 undulator (8-155 eV) or an Apple-II HU60 undulator (100-1500 eV), both able to adjust the light polarization. More precise photon energy selection is achieved by a plane-grating monochromator (PGM) with variable line spacing and variable groove depth grating. Once the beam has been monochromatized, it can be directed towards two end-stations: the high-resolution angle-resolved photoemission or the spin-resolved photoemission. Both branches are connected via a preparation chamber.

The high-resolution angle-resolved photoemission end station offers a beam spot ranging from 40 µm x 20 µm to 100 µm x 100 µm, depending on the energy. Its electron analyser was a Scienta R4000 ($\Delta\varphi = \pm 15^{\circ}$ acceptance angle). In the analysis chamber, the sample can be fully oriented using a six-axis cryogenic manipulator (3 translations, 3 rotations). The working temperature can be in the range of 13 to 350 K, low temperatures are achieved and stabilized with a liquid helium cryostat.

An experiment concerning the CDW stabilization in $LaSb_2$ at low temperature (detailed in Chap.3) was carried out in this end station. Sample preparation methods carried out in this end station can be found at Sec.2.3. In particular, mechanical exfoliation of the samples took place in the analysis chamber at 13 K and at a base pressure below 10^{-10} mbar.

2.2.1.2 SOLARIS synchrotron: URANOS beamline

The SOLARIS National Synchrotron Radiation Centre is located in Krakow, Poland. The single-ring synchrotron works at 1.5 GeV, offering a current of 500 mA in decay mode. There, the URANOS beamline (former UARPES) is powered by an Apple-II type undulator, covering a photon energy range of 8 to 500 eV. High photon flux, high resolution, variable polarization and minimal harmonic contamination are achieved with a quasi-periodic arrangement of the magnets. Beam monochromatization is achieved with a normal incidence monochromator (NIM) for low-energy photons (8-30 eV) and with a PGM for higher energies (14-500 eV).

In the end station a beam size of 60 µm x 150 µm is obtained (it is possible to reduce it down to 60 µm x 60 µm but losing some photon flux). The spectrometer consists of an Omicron-Scienta DA30-L deflector electron analyser (30° full cone acceptance) and the automated cryogenic five-axis sample manipulator (3 translations, 2 rotations) works in a temperature range of 6.5 to 500 K.

Most of the work related to the MoS_2 defect production and the boosting of its hydrogen catalytic activity was performed in this beamline (Chap.5). The end station is especially efficient in dealing with a large number of samples and treatments. The preparation chamber has a base pressure $\sim 2 \cdot 10^{-10}$ mbar and is suitable for sample exfoliation, annealing, sputtering and hydrogenation. The treatment effects on the sample's quality can be readily examined using the available low-energy electron diffraction (LEED). Sample hydrogenation, sputtering, and annealing may all be done in the preparation chamber. Once the sample is prepared, it can be directly transferred to the analysis chamber for ARPES measuring (base pressure below 10^{-10} mbar) or stored in the parking. This large parking is conveniently placed halfway between the analysis and the preparation chamber, considerably reducing the number of transfers to be done.

2.2.1.3 ELETTRA synchrotron: APE-LE beamline

The storage ring of the ELETTRA synchrotron at Basovizza, Italy, works at 2 and 2.4 GeV achieving a beam current of 140 and 310 mA, respectively, feeding up to 28 beamlines. Among them, the APE beamline is simultaneously supplied by two noncollinear insertion devices able to work independently. There is a high-energy branch (APE-HE) working between 200 to 1600 eV, dedicated to spectroscopies for magnetic materials. A low-energy branch (APE-LE) covering a range of 10 to 100 eV, devoted to high-resolution ARPES. The thesis experiments were conducted at the APE-LE branch. An Apple-II type undulator with a non-periodic array of permanent magnets acts as an insertion device and then, depending on the desired photon energy, a set of three different PGMs are available for monochromatization. Further beam focusing is done by combining a spherical mirror (vertical focus) and a toroidal mirror (horizontal mirror).

At the APE-LE end station, the focused beam has a beam spot size of 50 µm x 100 µm, the analysis chamber is equipped with an Omicron-Scienta DA30 deflector electron analyser. The sample position and temperature can be adjusted with a cryogenic five-axis sample manipulator (3 translations, 2 rotations) with a minimum temperature of 13 K, stabilized by a liquid helium cryostat.

The experiments at this beamline were devoted to the defect production in MoS_2 and the hydrogen adsorption on defective surfaces (Chap.5). The end station is well prepared for both purposes, the analysis chamber was cooled down to a 110 K temperature, with a pressure $\sim 10^{-10}$ mbar. The capabilities offered by the APE-LE end station are similar to those described in Sec.2.2.1.2. Therefore, the experiments were carried out in the same way.

2.2.2 . The electron analyser: angle detection

Photoelectrons leaving the sample have a certain distribution of kinetic energy and angles concerning the surface normal which are measured by a hemispheric electron analyser, conveniently placed in front of the sample to maximize photoelectron collection (see Fig.2.4a).

Before entering the hemisphere, the electrons go through a set of electrostatic lenses. The position of these electro-optical elements is represented in Fig.2.4b. These lenses are in charge of defining the acceptance angle, deflecting electrons of the photoemission cone into the optical axis, focusing between transmission or angle multiplexing modes and applying a delay to match the kinetic energy of the electrons according to the pass energy.

Concerning ARPES measurements, angle multiplexing is the proper mode for resolving the VB electronic structure. In this mode, the electron's trajectory through the hemisphere can be decomposed into two planes: dispersive and non-dispersive. Fig.2.4b shows how electrons with different energies disperse due to the voltage applied between the inner and outer hemispheres.

At the exit slit, the electrons are arranged according to their initial energy. The photoelectron angle information is preserved because the optical column focuses the electrons in such a way that it is maintained when they pass through both the entrance and exit slits (non-dispersive plane). Finally, a combination of microchannel plate, phosphorus screen and CCD camera are placed after the exit slit to amplify and record the electronic signal.

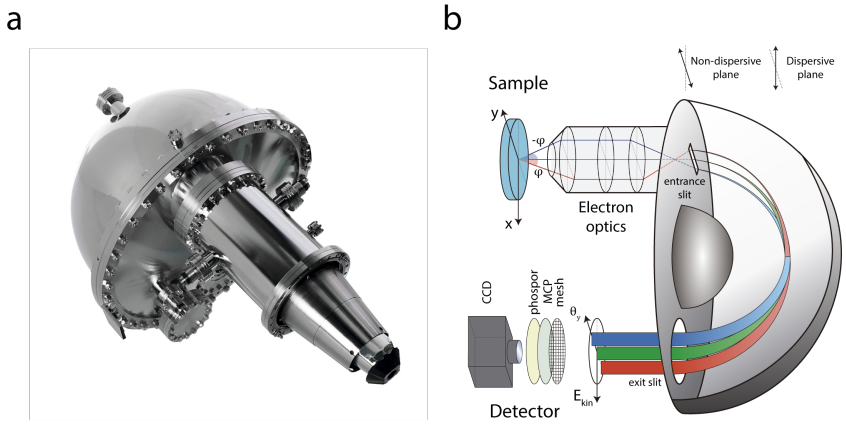

Figure 2.4: (a) Image of a ScientaOmicron DA30-L state-of-the-art hemispherical analyser. (b) Scheme of the analyser showing the acceptance angle (φ) and the internal trajectories of the electrons and the spatial orientation of the dispersive and non-dispersive planes. Once the electrons are momentum and energy sorted they are redirected towards the detector section.

2.2.3 . Data analysis: methods and procedures

The electronic structure is concisely represented by the bands dispersing along the crystalline high symmetry directions.

The whole electronic structure is acquired by ARPES through a volumetric dataset (E_k, φ, θ, Intensity) from which the desired information can be a posteriori extracted. The scientific software Igor Pro allows this type of data to be processed and it is often used by the photoemission community. There is a substantial amount of Igor Pro code and tools, often developed by the beamlines or users themselves, that are extremely helpful in data analysis.

An ARPES image offers, at a glance, a lot of qualitative information about the electronic properties of the sample. However, for a quantitative approach, the use of profiles is advised to extract the dispersion data. In Fig.2.5a two kinds of profiles are represented. An intensity profile as a function of the energy at constant momentum, which is known as an energy distribution curve (EDC) (white dashed lines) and an intensity profile as a function of the momentum at constant energy, which is known as a momentum distribution curve (MDC) (red dashed lines).

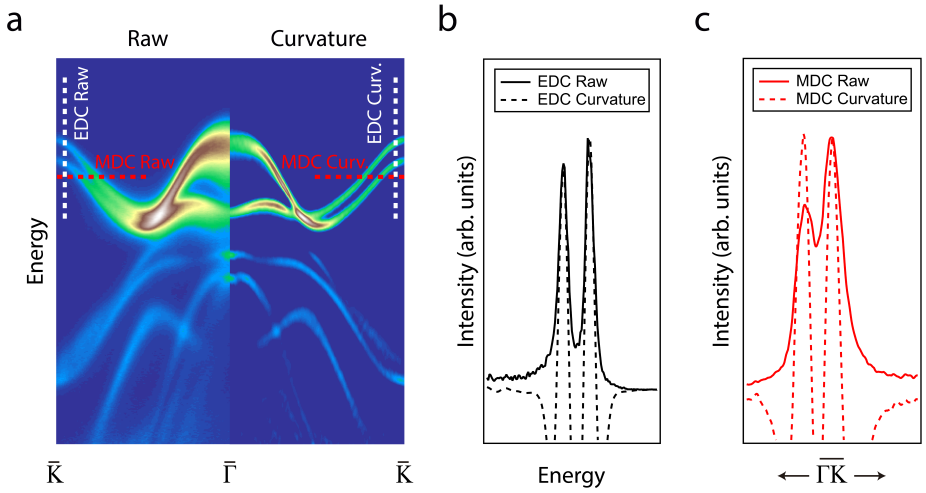

Figure 2.5: (a) Comparison between a raw ARPES image and the curvature image of $MoSe_2$ bands along $\overline{\Gamma K}$. In general, a sharper band structure is observed in with the curvature. The withe and red lines correspond to profiles shown in (b-c). (b-c) EDCs and MDCs profiles near the K point indicated in (a) show the $MoSe_2$ spin splitting (~ 186 meV). The peaks in the raw and the curvature image appear at the same energy and momentum showing that no shift is induced by applying the curvature method.

The EDCs have a clear physical meaning since they give specific details about the spectral function. For instance, EDC analysis allows observing the quasi-particle excitation peak, to extract the relatively small gap energy in a CDW transition or to resolve subtle changes near the Fermi level, such as slope changes due to the

presence of defect states. Yet, one inconvenience of using EDCs is that peak fitting is not easy. The curves are convoluted with an energy-dependent background (often approximated by a Shirley curve) and by the Fermi-Dirac distribution near the Fermi level, adding complexity to the fitting process. To overcome this, using MDCs rather than EDCs is preferred for certain purposes. Working with constant energy profiles removes the above-mentioned drawbacks since they are energy-dependent. Also, the MDC has a more symmetric line shape easier to fit by a Lorentzian function. Thus, the peak position and full width at half maximum (FWHM) can be easily extracted, allowing for dispersion tracking and quasi-particle lifetime determination. In addition, MDCs are useful for accurately determining the topographic details of a constant energy map (CEM), a map showing the ARPES intensity along both $\mathrm{k_x}$ and $\mathrm{k_y}$ parallel momenta at a certain binding energy.

In certain cases, visualizing raw ARPES data can be challenging due to significant image-blurring sources that can be present, namely, band overlapping, poor crystalline quality, surface dirtiness, matrix elements, low cross-section, etc. In such cases, the second derivative or the curvature of the intensity has been proven to be an extremely robust procedure to enhance the data visualization [96]. The curvature method is used in preference to the second derivative method in this work because it produces sharper ARPES images without shifting the peak positions (see Fig.2.5a). The EDC and MDC profiles drawn in Fig.2.5a are represented in Fig.2.5b,c and allow us to observe the effectiveness of the curvature method. Through this work, the most frequent use of this method is in the comparison of experimental and calculated band structures.

2.3 . Sample preparation methods

This work comprises the study of a light rare-earth diantimonide, $LaSb_2$, grown by the flux method [97] and MoS_2 a member of the TMDs family grown by chemical vapor transport (CVT) [98]. All the samples, in the form of large, flat, bulk crystals with metallic micaceous appearance, were produced from high-purity elements (see Fig.2.6a). The surface preparation methods of the samples in this work are described in the following.

2.3.1 . Lanthanum diantimonide: $LaSb_2$

Mechanical exfoliation. The layered nature of the $LaSb_2$ makes it especially suitable for selecting mechanical exfoliation as the best surface preparation technique. To achieve the best results when cleaving the top-post method was used at a pressure below 10^{-10} mbar in flat and homogeneous scraped surfaces. This method involves glueing a metallic or ceramic post to the surface and later

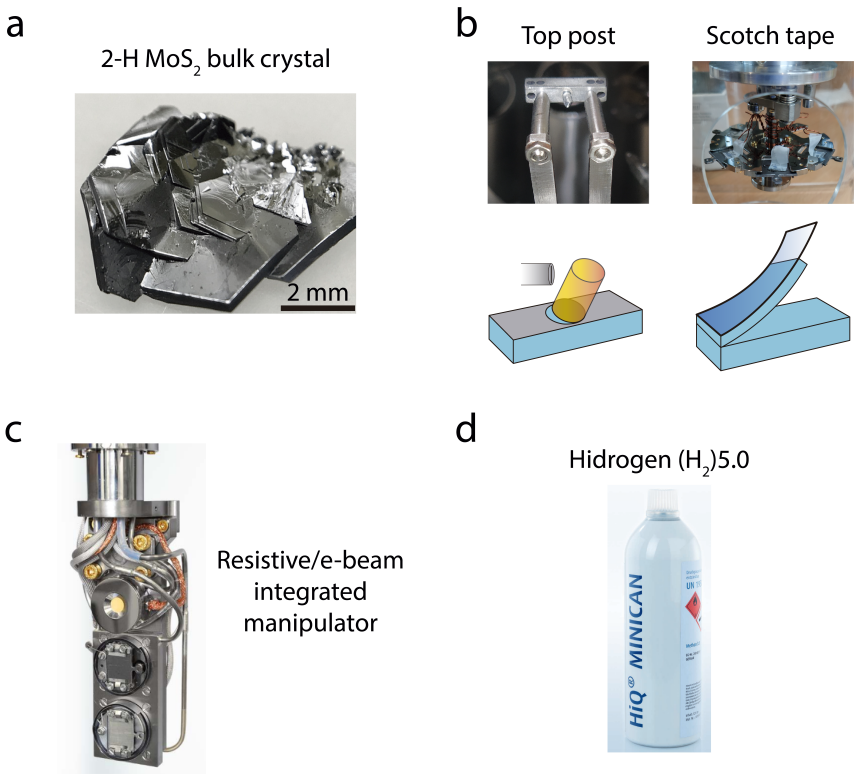

Figure 2.6: (a) Detail of the MoS_2 crystal layered nature. The scale bar (black line) indicates that the crystal size is $\sim$ 6 x 4 mm^2. Representative of all the samples used in this work. (b) Left up. Sample holder head loaded with samples ready for adhesive tape exfoliation. Left down. Adhesive tape exfoliation sketch, removing the tape creates a mechanical force that removes the topmost layers. Right up. Detail of a transfer arm holding a sample with a top post. Right down. Top-post exfoliation, the post is removed by a stroke exposing a fresh surface. (c) UHV sample manipulator with integrated resistive and e-beam. A thermocouple placed near the sample allows for an estimation of the temperature. (d) Left. Hydrogenation is done with pure hydrogen gas (99.999 %).

tearing it off using a stick (see Fig.2.6b). This operation can be done within the analysis chamber (in situ) since the post and the silver-epoxy glue employed are UHV-compatible.

The sample cleaves between the La/Sb bilayer, exposing a surface composed of (001) Sb atomic planes. The fresh surface region exposed after exfoliation is much larger than the photon beam size. It is important to emphasize that the highly reactive nature of rare earths (La) limits data collection in time, thus limiting the statistics of the measurements.

2.3.2 . Transition-metal dichalcogenides: MoS_2

The sample preparation methods for MoS_2 are described in the following.

Mechanical exfoliation. The featuring van der Waals-type interlayer bonding of MoS_2 allows for easy adhesive tape layer exfoliation. In this process, the adhesive side of the tape is glued over the sample surface to later peel off, exposing a new surface (see Fig.2.6b). It is highly recommended to perform the exfoliation within the load lock or the preparation chamber as the leftover tape spoils the vacuum. This will help to preserve the analysis chamber as it is usually the cleanest chamber.

The quality of the adhesive tape exfoliated surfaces has been examined carefully under an optical microscope. Large and flat single crystalline areas were spotted. After one exfoliation, the samples are often usable again. Once inside the vacuum, the characteristic low reactivity of MoS_2 allows it to be vacuum stored for large periods without any detectable ageing effect.

Annealing: The application of thermal annealing has a twofold purpose in the thesis. First, a mild annealing at 200°C for 5 minutes is applied to remove the surface adsorbates. Second, it is used to generate chalcogen defects in the crystalline structure. Chalcogen defect generation is thermodynamically the most feasible process since the formation energy for any transition-metal defect is much greater [99].

The UHV annealing is achieved using a resistive and electron-beam (e-beam) heating device that is usually integrated into the manipulator arms of the chamber. In Fig.2.6c an example of the device is shown. This built-in annealing solution is convenient since the samples are usually mounted on bare metallic plates. A closed-loop electronic controller is used to set a target temperature value, the loop is fed with temperature readings obtained by a thermocouple attached to the sample holder. At the same time, a pyrometer focused on the sample surface allows for a more precise estimation of the temperature. Each treatment consists of increasing the temperature up to 200 °C for 5 minutes to remove adsorbates and then flash the sample to the set-point temperature by ramping the temperature manually.

Low-energy ion sputtering (LEIS): The material surface can be cleaned by ion sputtering with non-reactive gases (e.g. argon, helium, neon). The accelerated ions strike the surface causing the sputtering of unwanted species. However, sputtering can also be used as an effective tool for producing defects in MoS_2 by properly selecting the non-reactive gas, as well as the ion's kinetic energy. Low-energy argon ion sputtering (70 eV) at room temperature (RT) was established for this work, looking for a compromise between effective defect production and preserving sample crystallinity. Loss of crystalline order is an unwanted effect since it greatly spoils the ARPES spectrum quality.

To quantify the sputtering effects, the number of ions impinging the sample per unit time (N/t (ions/s)) is calculated. This quantity is given by the following equation: $N/t = I_s/e$, where I_s is the ion current reaching the sample and t is the

exposition time. As mentioned, since the sample holder manipulator is properly wired it is easy to measure I_s with a multimeter. A current $I_s = 1.05$ (μA) is obtained for an ion's energy of 70 eV, an Ar pressure of $p_{Ar} = 1{\cdot}10^{-6}$ mbar and the sample oriented perpendicular to the ion beam ($\alpha = 90°$). For convenience, sample treatments are done maintaining N/t and varying the exposition time. Thus, the total number of ions (N) can be calculated from the following equation:

$$N\ (ions) = 6.56 \cdot 10^{12} \cdot \text{exposure time (s)} \tag{2.16}$$

since $N/t = I_s/e$ is maintained constant, the exposure time is indicated adjacent at each treatment for comparison between different treatments.

Hydrogenation: to explore how hydrogen interacts with sulfur defects in MoS_2, treated samples are further exposed to high purity hydrogen (H_2) (Fig.2.6d). Starting with a base pressure below $5{\cdot}10^{-10}$ mbar and at RT, the preparation chamber is filled through an inlet gas valve up to a target partial pressure. The partial pressure is appropriately determined with a mass spectrometer. For convenience, the hydrogenation treatments are achieved by maintaining a constant partial pressure while varying the exposure time. The exposure, in Langmuir units (L), is calculated from the following equation:

$$\text{Exposure}\ (L) = \frac{0.75}{10^{-6}} \cdot \text{pressure (mbar)} \cdot \text{exposure time (s)} \tag{2.17}$$

Exposure and pressure are indicated adjacent at each treatment for a better comparison.

3 - A CDW transition in $LaSb_2$

Light rare-earth diantimonides, RSb_2 (R=La-Nd), are a family of isostructural semimetals discovered approximately 60 years ago [100]. These layered compounds exhibit complex and fascinating physical behaviour. Unrecognised for some time, it was not until the 1990s that interest in studying these compounds flourished, thanks to improvements in the synthesis of single crystals [97]. Bud'ko et al. seminal work showed that diantimonides exhibit a complex set of magnetic phases, strong anisotropies and a large nonsaturating linear magnetoresistance (LMR) [101]. As mentioned in Chap.1, the phenomena observed in both diantimonides and closely related compounds have, at their core, a critical interplay between their layered nature (quasi-2D materials) and electronic structure. This chapter focuses on the non-magnetic member of the diantimonides group, $LaSb_2$. The lack of magnetic phases at low temperatures simplifies the identification of the mechanisms driving the observed anomalous properties.

The $LaSb_2$ crystalline structure is shown in Fig.3.1a. The crystal belongs to the orthorhombic *Cmce* space group with lattice parameter: $a' = 6.319$. $b' = 6.174$ Å and $c = 18.671$ Å(light blue lattice). The structure is formed by 2D sheets of Sb atoms sandwiched between La/Sb bilayers, stacked along the *c*-axis. Additionally, the primitive cell is presented with a smaller volume (red lattice) to correctly match the BZ symmetry. A top view of the primitive and conventional unit cells is shown in Fig.3.1b. In $LaSb_2$ the use of this conventional cell is more frequent than the primitive cell since it is more convenient for visualising the structure's 2-fold symmetry.

$LaSb_2$ is a superconductor with a critical temperature of 0.4 K [103], although the onset of the transition starts at 2.5 K (see Fig.3.1d). Such a wide transition is unlikely to be caused by phase coexistence or impurities, as a large mean-free path for carrier transport along the *ab* plane was found ($l \sim 3.5\ \mu m$) [47]. Moreover, the highly anisotropic character of the resistivity confirms the quasi-two-dimensionality of the structure ($\rho_c/\rho_{ab} \approx 200$ at 4 K) [101]. Because anisotropy produces poor coupling between layers, the transition to the superconducting phase does not occur uniformly throughout the material. First, the *ab* planes start to superconduct at 2.5 K, but incoherently concerning other planes. When the temperature is further reduced, coherent coupling between layers emerges. Full coupling is reached below 0.5 K, indicating that the bulk is superconducting [47].

The magnetoresistance of $LaSb_2$ exhibits puzzling behaviour. For close FS orbits, the semi-classical theory (Lifshitz theory) predicts two regimes for the MR

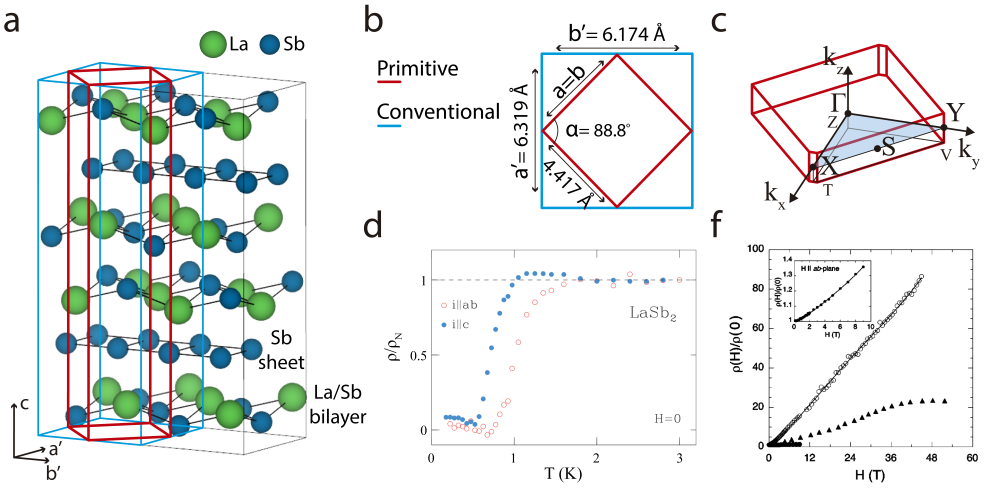

Figure 3.1: (a) Layered $LaSb_2$ crystalline structure, formed by Sb sheets and La/Sb bilayers. The primitive and conventional unit cells are drawn with red and blue lines, respectively. The bonds between planes were removed for clarity. (b) Top view of the cells primitive and conventional unit cells showing the lattice parameters. (c) The BZ corresponding to the primitive cell and the high-symmetry points, the light-blue plane indicates the surface Brillouin zone (SBZ) projection. (d) Resistivity, ρ, normalized to the normal-state resistivity, ρ_N, vs. temperature, T, for currents along the *ab* plane (red open dots) and the *c* axis (blue dots). The applied magnetic field (H) is zero. Adapted figure from [47]. (e) Transverse MR of $LaSb_2$ at 2 K with the current in the *ab* plane and magnetic field oriented parallel (closed dots) and perpendicular (open dots) to the *ab* plane. Inset: Low field MR with H parallel to the *ab* plane. The solid lines represent a least-squares fit to the data using a fourth-order polynomial. Adapted figure from [102].

dependence on the magnetic field: a low-field limit, where the MR has a quadratic dependence of the magnetic field and a high-field limit, where the MR saturates.

$$\frac{\Delta\rho}{\rho_0} \propto \begin{cases} (\Omega\tau)^2 & \Omega\tau \ll 1 \\ 1 & \Omega\tau \gg 1 \end{cases} \tag{3.1}$$

where $\Omega = eH/mc$, is the cyclotron frequency, τ is the electron relaxation time and ρ_0 is the resistance at zero field. In the case that open FS orbits are present, and the current flows parallel to them, MR does not saturate at high fields but continues to increase quadratically [104].

Fig.3.1f shows the transverse (longitudinal) MR at 2 K with the current in the *ab* plane and the magnetic field oriented perpendicular (parallel) to the *ab* plane. It is linear and very large (10,000 %), up to fields of at least 45 T, and with no signs of saturation [102]. This behaviour is in contradiction with the semi-classical theory of MR. LMR has been observed in different types of materials, the following mechanisms have been proposed:

1) Local fluctuations. LMR has been measured in 2D electron gas systems

[105] in which carrier concentrations are very low and mobility is extremely high. Possible local fluctuations in carrier density were proposed to hold the LMR [106]. These conditions are not satisfied in $LaSb_2$.

2) Inhomogeneities and disorder. In silver chalcogenides the LMR is due to inhomogeneities in the silver concentration across the sample, producing regions with high and low electron densities. [107]. Nevertheless, the magnetisation of $LaSb_2$ exhibits quantum oscillations [108], ruling out the existence of significant inhomogeneity and disorder.

3) Quantum LMR. Abrikosov [109] derived an expression for the LMR considering small carrier densities and that at certain regions of the momentum space a small effective mass can result from bands that disperse linearly (like in a Dirac-cone) close to the Fermi level [109]. Although a linear dispersion can be observed in $LaSb_2$ (see Sec.3.2.1), the carrier density, $n \sim 3 \cdot 10^{20}$ cm^{-3}, is far from being small [102] and therefore, criteria for quantum LMR in $LaSb_2$ is hardly satisfied.

4) LMR in CDW materials. It is frequently reported that CDW materials exhibit LMR in an extremely wide range of applied magnetic fields. The scattering mechanism that unifies the observed LMR and CDW considers that CDW stabilisation can lead to a change in the FS topology, generating so-called "hot spots" [110–112]. The CDW periodicity folds the FS according to the q vector and because nesting is usually imperfect, ungapped regions appear.

These ungapped regions form small pockets (the hot spots) with pronounced curvatures of the electron trajectories. Under high magnetic fields, the electron trajectories in these hot spots experience, not only scattering caused by CDW fluctuations but, possibly, magnetic breakdown effects, which is in agreement with the LMR observed at high magnetic fields. The CDW criteria presented fit very well with the nature of $LaSb_2$ and have motivated the experimental search for a CDW in the material.

3.1 . CDW phases in quasi-2D materials

A CDW occurs when electrons form a periodic spatial modulation in their charge distribution, resulting in a collective, ordered state with alternating regions of higher and lower electron densities. This periodic modulation often comes together with a periodic lattice distortion (PLD) [113].

As initially argued by Peierls, a half-filled 1D chain of evenly spaced atoms with a lattice constant a is unstable. The FS consist of two points located at $k_F = \pm\pi/2a$ and is perfectly nested because the points are connected by a single vector

(the nesting vector) $\vec{q} = 2k_F$. Electrons near the nested FS can be collectively excited and gain stability by periodically modulating the charge density along the chain. Consequently, a PLD accommodates the electronic modulation, setting up a (new) potential which opens a gap at $k_F = \pm\pi/2a$. The energy gained by reducing the occupied electron states must overcome the thermal fluctuations that disrupt the long-range ordering to stabilise the CDW. As a result, the CDW phase transition may occur at a critical temperature (T_{CDW}).

It is important to emphasize that ever since Peierls initially proposed a comprehensive elucidation of the CDW phenomena, the conditions for his theory to apply have been significantly relaxed and have been extrapolated to encompass systems beyond the original scope. In particular, it has been noted that the role of FS nesting appears to be less significant than other factors such as electron-phonon coupling [114], electronic correlations [115] or excitonic condensation [116] in the establishment of a CDW. Zhu et al. [117] extensively reviews this topic, revealing CDW as a complex phenomenon. First-principles calculations [118] showed that multiple mechanisms can generate CDW instabilities, the Peierls model is one of them, but there are also alternatives.

3.1.1 . CDW in $LaSb_2$ related layered compounds

Both CDW phases and LMR have been observed in rare-earth tritellurides [110, 119], $LaAgSb_2$ [120, 121] or $La_{1-x}Ce_xSb_2$ [122]. The nesting framework of the FS is essential for describing the CDW phase. When the Peierls picture is extended to real materials in two or three dimensions, perfect nesting conditions are only partially fulfilled. In this scenario, the signatures of CDW formation are smeared, although they endure near the nested regions in the form of ungapped fragments of the reconstructed FS [119].

Thus, a CDW may be the origin of the $LaSb_2$ LMR. Early band structure calculations predicted a FS with potentially nested sheets that would not be identifiable through de Haas–van Alphen (dHvA) oscillations [108]. A CDW phase in $LaSb_2$ has been actively sought, but its identification has proven so far to be elusive, so far. Previous PES experiments at 140 K [123] failed to resolve the dispersion relation close to the Fermi level, and scanning tunneling microscopy (STM) experiments at 0.15 K [124] did not find indications of CDW formation. X-ray diffraction (XRD) measurements [125] show that defects in the crystalline structure (twinning or stacking faults that mix the a and b directions) could be behind the CDW state as in the $La_{1-x}Ce_xSb_2$ case [122].

The primary motivation of this study is to gain a more comprehensive understanding of the $LaSb_2$ electronic structure. ARPES is a highly suitable technique for this endeavour, as it can reveal subtle details in the structure. The following

section presents experimental evidence of the stabilisation of a CDW in $LaSb_2$.

3.2 . Direct observation of a CDW transition

3.2.1 . Fermi surface

ARPES measurements were taken over a large area of the reciprocal space to search for changes in the electronic structure of $LaSb_2$ linked to a CDW. Measurements were taken at the CASSIOPEÉ beamline. The experimental details concerning the beamline are presented in Sec.2.2.1.1. Similarly, the sample preparation methods are described in Sec.2.3.

Fig.3.2a shows the $LaSb_2$ FS at 200 K (high-temperature) along the first and second BZ. Two main pieces feature the FS: a large diamond (warped square) with the corners touching the BZ at the $\overline{S}$ points, and a glasses-shaped pockets near the $\overline{\Gamma}$ point. The FS has 2-fold symmetry given the orthorhombic lattice, two mirror planes can be projected along the $\overline{\Gamma X}$ and $\overline{\Gamma Y}$ directions. Unlike other family compounds, such as $LaAgSb_2$, no FS sheets are centred at the $\overline{\Gamma}$ point [126, 127]. Furthermore, the inset of Fig.3.2a corresponding to a FS at a different photon energy ($h\nu$ = 100 eV) indicates a small dispersion along k_z. These FS measurements are in agreement with previous calculations and dHvA experiments [108]. On the other hand, Fig.3.2b shows a dramatic change of the FS shape when the temperature is reduced to 13 K (low-temperature). The entire FS is replicated along $\overline{\Gamma Y}$, matching the orientation of the glasses-shaped pockets.

To better understand these changes, several MDCs[1] at the Fermi level have been taken. Two sets of coloured lines (light-green and pink lines) for each temperature are drawn in Fig.3.3, indicating the regions of the reciprocal space where the MDCs have been taken. The coloured dots (blue and orange) mark the intensity maxima at each MDC. The MDCs across the edge of the *diamond* (light-green lines) are presented in Fig.3.4a-b for 200 K and 13 K, respectively. While at 200 K only one maximum appeared (blue dots); at 13 K, a replica is observed (orange dots). The separation between the two maxima is constant and corresponds to $q = 0.25 \pm 0.02$ Å^{-1}. Additional MDCs across the glasses-shaped pockets (pink lines) are presented in Fig.3.4c-d showing further *q*-interconnections.

[1] See Sec.2.2.3 for details about MDC analysis.

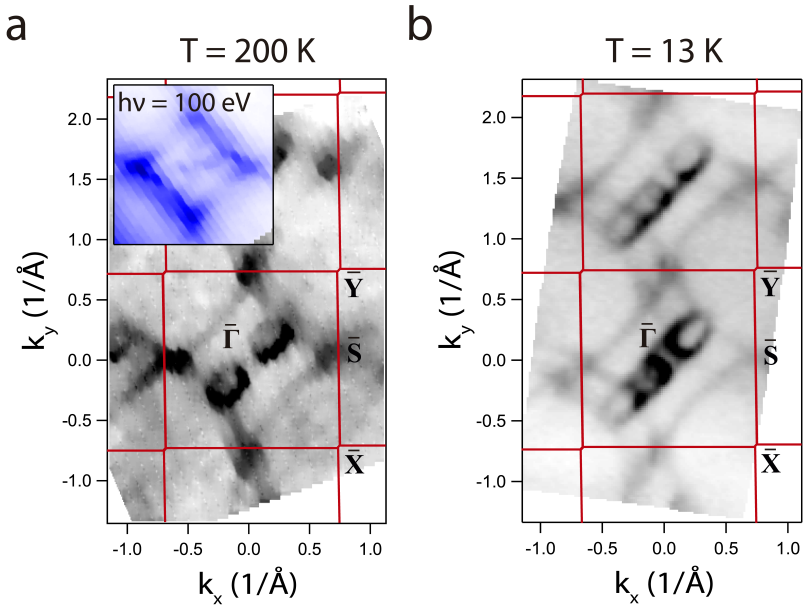

Figure 3.2: Experimental k-space mapping of the FS obtained from the plot of the ARPES intensity as a function of the k_x and k_y vectors at the Fermi level. The panels cover the first and second BZs. Measurements were done at (a) T = 200 K and (b) T = 13 K and taken with $h\nu$ = 118 eV photon energy. Inset: FS at T = 200 K taken with $h\nu$ = 100 eV photon energy.

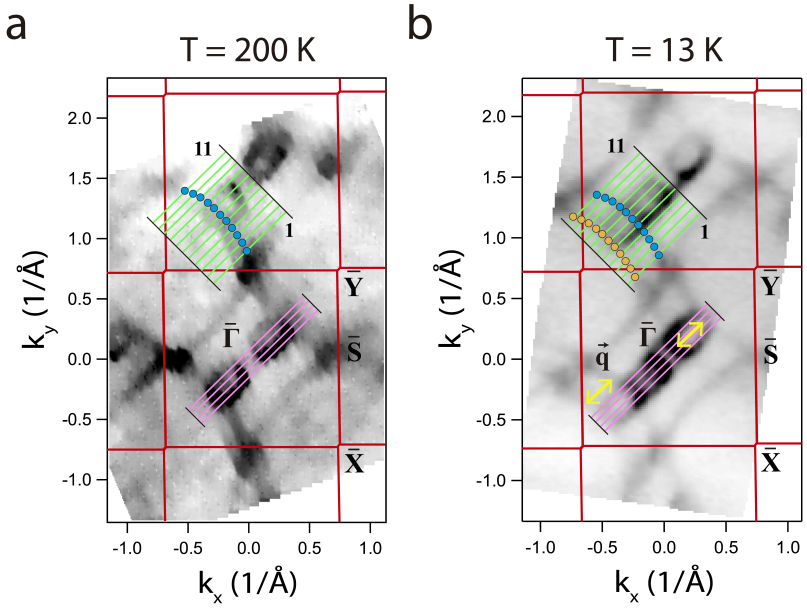

Figure 3.3: Experimental k-space mapping of the FS presented in Fig.3.2. The light-green and pink lines indicate the *k* at where the MDCs are taken. The MDCs are number-labelled and the blue and orange dots indicate the intensity maxima. The yellow arrow indicates the *q* length and direction.

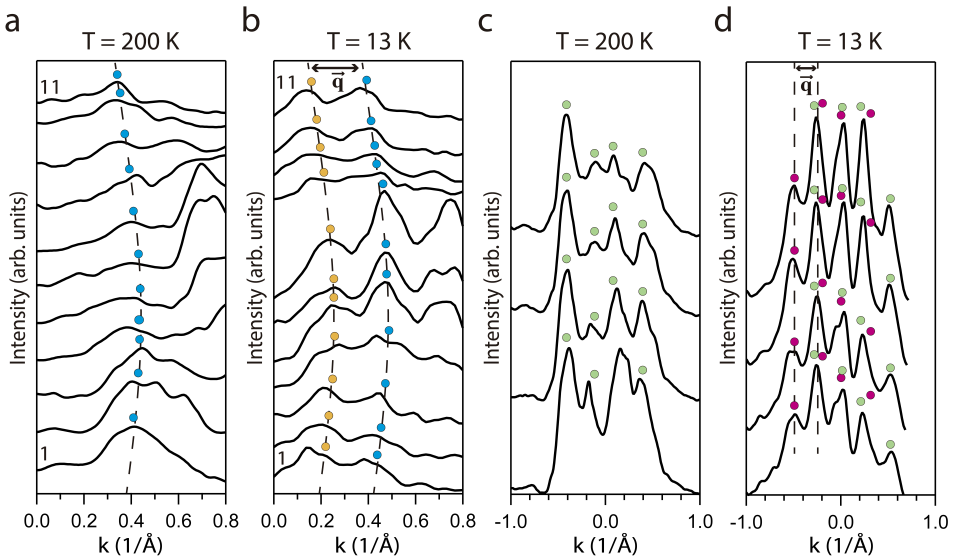

Figure 3.4: MDCs at the Fermi level, the locations of the curves in the reciprocal space are indicated in Fig.3.3, $k = 0$ corresponds to the line start. (a) and (b) 200 K and 13 K, respectively. The replica of the 200 K intensity maxima (blue dots) can be observed at 13 K (orange dots), separated by a distance q. Additional MDCs showing the replica at the first BZ are presented in (c) and (d), 200 K and 13 K, respectively. The green and magenta dots are a guide to the eye indicating the original and replicated FS, respectively.

The observation of the FS replica at low temperature is indicative of a modulation of the electron density in the direction of the q vector, suggesting the stabilisation of a CDW. Further information is obtained by analysing the band dispersion.

3.2.2 . Band structure

The complete ARPES $LaSb_2$ band structure along the $\overline{\Gamma Y S X \Gamma}$ high-symmetry directions path are presented in Fig.3.5a-b, measured at 200 K and 13 K. Given the notable intensity contrast between certain shallow bands and the Fermi level, the curvature analysis is utilized to accentuate the dispersive characteristics in proximity to the Fermi level.[2].

Fig.3.6a-b shows significant differences between 200 K and 13 K. Particularly noteworthy is the increased energy difference at low-temperature of the flat bands near -0.5 eV and -1 eV 200 K. This can be a manifestation of the renormalisation induced by electronic correlation effects in the low-temperature phase, which leads to a bandwidth (W) reduction of the bands.

Nevertheless, the most important difference occurs in the Fermi level region,

[2]See Sec.2.2.3 for more details about the curvature method.

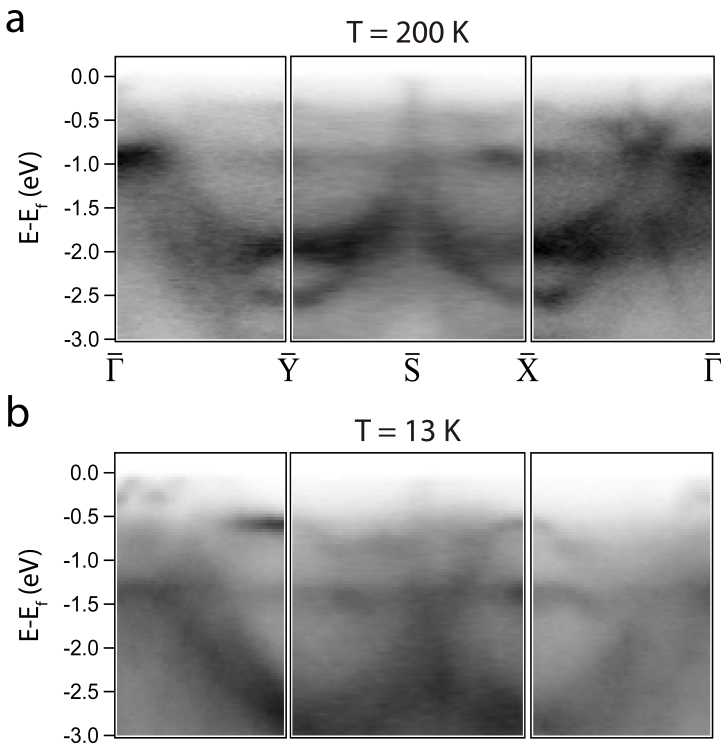

Figure 3.5: ARPES intensity showing the $LaSb_2$ band structure along the high-symmetry directions $\overline{\Gamma YSX\Gamma}$ at (a) 200 K and (b) 13 K. Data were taken with $h\nu = 118$ eV photon energy.

where electronic instabilities play a key role (see Fig.3.6c-d). At 13 K, the dispersion along $\overline{\Gamma Y}$ presents a strong folding of the bands giving rise to the *glasses-like* pockets, shifted by the $q = 0.25$ Å^{-1} nesting vector.

Experimentally, the presence of a CDW has three fingerprints in the electronic band structure: the existence of a nesting q vector, the opening of a gap, and band folding that is directly related to a PLD. The origin of the first two has been argued previously, but nothing has been stated regarding band folding. When a CDW phase is established, two competing period potentials coexist: periodicity related to the original network and periodicity related to the PLD. Despite the translational symmetry breaking, the spectral weight (and thus the ARPES intensity) remains concentrated in the original band structure but is modulated by the potentials (one due to the original lattice periodicity and the other one to the CDW periodicity). Consequently, energy gaps appear at certain wavevectors, generating folded bands whose weights are proportional to Δ/W (Δ being half the gap energy) [128, 129]. This is precisely what can be observed in Fig.3.6d, the W reduction in the FS causes a large spectral weight transfer to the folded band.

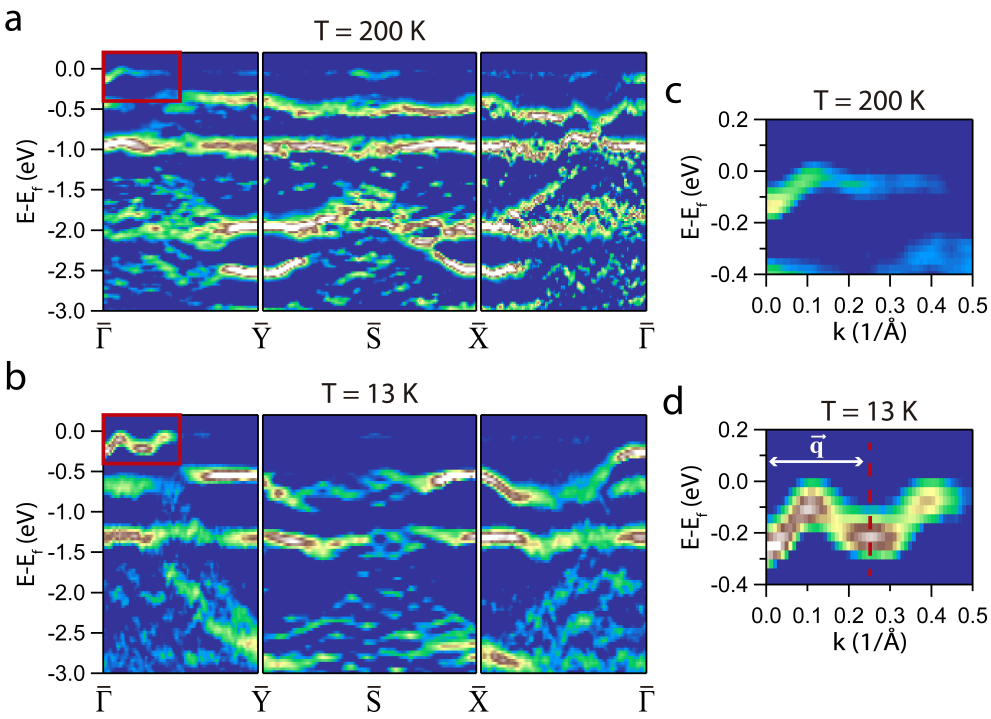

Figure 3.6: Curvature intensity showing the $LaSb_2$ band structure along the high-symmetry directions $\overline{\Gamma Y S X \Gamma}$ at (a) 200 K and (b) 13 K. Panels (c) and (d) are zooms of the areas indicated with a red rectangle in panels (a) and (b) respectively. Data were taken with $h\nu = 118$ eV photon energy.

Since the curvature plot potentially induces alterations in relative intensities, additional changes in the bands can be thoroughly examined in the raw ARPES spectra. By comparing Fig.3.7a-b, a significant reduction of the spectral weight near the Fermi level can be observed at 13K. This reduction is compatible with a Mott transition, the bandwidth reduction caused by the CDW pushes the W/U parameter into a favourable direction for Mott physics to take place [130].

By contrast, no signs of gap opening are observed in Fig.3.7b. For the gap to be observed, it should be larger than the band energy broadening (here ~ 100 meV). Since the CDW transition temperature is somewhere $13 \leq \mathrm{T_{CDW}} < 200$ K, the largest possible gap should be comparable to the thermal energy at 200 K, that is, 18 meV. Therefore, the band energy broadening difficult the observation of a gap opening at the FS. Moreover, CDW transitions are not always associated with a band gap opening [131].

It is worth comparing the changes in the electronic structure reported in this work and those reported in earlier research on related compounds such as $LaAgSb_2$ and $La_{1-x}Ce_xSb_2$. $LaAgSb_2$ has a PLD with a periodicity corresponding to 0.037 $Å^{-1}$ (0.026 $2\pi/a$) [120] considerably smaller than the 0.25 $Å^{-1}$ value obtained for

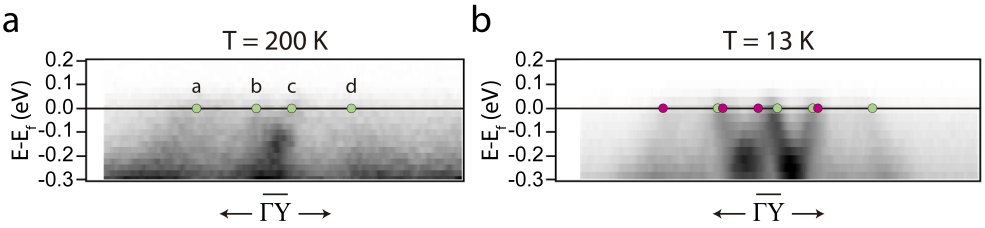

Figure 3.7: Experimental band structure along the $\overline{\Gamma Y}$ direction above and below the CDW phase transition temperature. Panels (a) and (b) depict the bands crossing the Fermi level that give rise to the *glasses-like* pockets. The crossing points (a, b, c, d) are roughly marked with green dots. The magenta dots in (b) mark the replica crossing points.

$LaSb_2$ in this thesis. The limited magnitude of the $LaAgSb_2$ q vector complicates the observation of modifications in the electronic structure. Specifically, Shi et al. observed that the effects associated with CDW stabilisation are confined only to a curvature intensity decrease near the Fermi energy [127].

CDW signatures have been observed in $La_{1-x}Ce_xSb_2$ [122]. In particular, stronger signatures suggestive of CDW occur at $x \approx 0.5$. The signatures consisted of a pronounced kink in the resistivity vs. temperature, as well as in the specific heat. One of the conclusions of this study is that, since the kink is present across most of the $La_{1-x}Ce_xSb_2$ series, the CDW signatures at $x \approx 0.5$ can be extrapolated to $LaSb_2$ and thus, an analogous kink in the resistivity for $LaSb_2$ would correspond to a CDW in this material at 355 K. However, as no specific PLD was reported for $La_{1-x}Ce_xSb_2$, it is hard to establish any relationship between the CDW at 355 K and the CDW observed in this thesis at 13 K. Since sequential CDW phases are quite common [120, 129, 132, 133], this seems to be the most likely scenario in $LaSb_2$.

However, it may seem inconsistent that no traces of CDW behaviour on transport measurements below 200 K could be found in Luccas et al., while clear signatures of CDW between 200 K and 13 K are reported in this work. Nevertheless, since the nested region shown in Fig.3.2b consists of a modest fraction of the FS, it may be hard for a transport measurement to show a kink. Certainly, it is not uncommon for macroscopic measurements to overlook the exact transition temperature or exhibit apparent discrepancies when compared to photoemission data [134–136]. Therefore, far from being inconsistent, the CDW at 13 K reported herein contributes to complete the knowledge of the $LaSb_2$ electronic nature.

3.3 . Theoretical model of the PLD

The experimental evidence at low temperature demonstrates the presence of a FS replica and strong band folding, both arising from the *glasses-like* pockets feature. The connection between the replica and the original spectral feature is made via the *q* vector, which matches the size of the pocket. After identifying the FS portion involved in the FS nesting, the question arises as to which atoms generate the nested FS sheets.

To this end, density functional theory (DFT) calculations of the $LaSb_2$ electronic band structure were carried out. The calculations were performed by Dr. Lipin Chen, a former member of the LUTECE group at the LPS, Orsay[3]. Fig.3.8a presents the theoretical 3D FS. In the figure, the sheets are highlighted using a colour code[4]. The band structure along the $\overline{\Gamma Y S X \Gamma}$ path is illustrated in Fig.3.8b following the same colour code. Both the FS and band structure calculations exhibit good agreement with the experimental data shown above (see Fig.3.3a and Fig.3.6a). Moreover, the 3D FS confirmed a small dispersion along k_z. To compare the calculations with the experimental bands more clearly, the energy range of the calculations was restricted to values around the Fermi energy. To better relate the band structure and the FS, the Fermi level band crossings are marked with points (labelled from a to f).

Further information on the FS sheets is provided by the atom-projected band structure. Fig.3.8c-e corresponds to the projection on the Sb atoms of the Sb sheets, on the La atoms of the La/Sb bilayers, and on the Sb atoms of the La/Sb bilayers, respectively. The *diamond* (warped square) is mainly originated from the cone-like dispersing bands associated with the Sb atoms in the Sb sheets (see Fig.3.8c). On the other hand, the *glasses-shaped* pockets in the FS arise from a mixture of La and Sb orbitals in the La/Sb bilayer (see Fig.3.8d-e). A close inspection of the FS reveals that the *glasses* have a significant sheet portion parallel to each other (non k_z dispersing) along ΓY. This nesting arrangement is favourable to trigger a CDW phase, as previously argued.

The experimentally determined *q* vector corresponds to one-third of the ΓY distance; therefore, in real space, the PLD length should be three times the **a** + **b** distance (i.e. 3*b'*). Thus, to model the PLD a supercell containing three conventional unit cells will be used. Because DFT is a static simulation, it is difficult to accomplish temperature-dependent changes. Hence, to simulate the low-temperature crystal structure, different structural modifications of the undistorted

[3]Details about the calculation methods can be found in Appx.A.1.

[4]The colour code in Fig.3.8a-b is not related to an orbital projection. It only indicates the different sheets composing the FS.

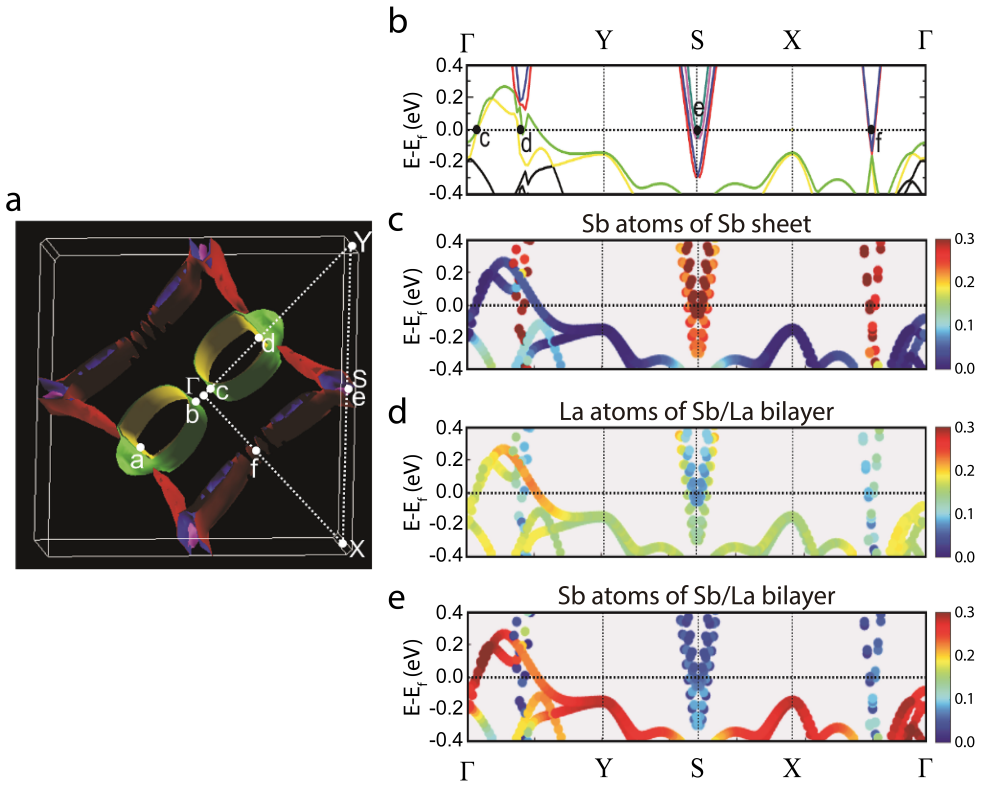

Figure 3.8: Theoretical electronic band structure of $LaSb_2$ using DFT. (a) Calculated 3D FS. *Diamond* sheets (blue, red), *glasses-like* pockets sheets (yellow, green). (b-e) Electronic band structures along the $\overline{\Gamma YSX\Gamma}$ path. The band structure is projected on the Sb atoms of the Sb-sheets (c), La atoms of the La/Sb bilayers (d), and Sb atoms of the La/Sb bilayers (e). The colour scale indicates the contribution of each atom to different bands. The crossing points of the bands with the Fermi level (a, b, c, d) are marked in panels a and b.

supercell were calculated. This procedure involves applying a specific distortion and then allowing the rest of the atoms in the structure to relax, thus inducing a CDW corresponding to a particular q vector. The following supercells and their unfolded band structures have been calculated:

The pristine supercell is shown in Fig.3.9a. In Fig.3.9c a 0.02 Å displacement along b' of half the atoms of the conventional cell is applied. Fig.3.9e correspond to a longitudinal wave-like modification of the Sb atoms within the Sb sheets. Two middle Sb atoms are displaced towards each other along b', reducing their distance by 0.03 Å. Fig.3.9g shows a wave-like distortion along b' displacing the whole middle conventional cell 0.02 Å. Fig.3.9b present the pristine bands in the region where folding was observed, the bands describe well the phase at 200 K. The bands corresponding to the described PLDs are shown in Fig.3.9d, f, h.

Among the three suggested PLDs, it can be noted that the latter model

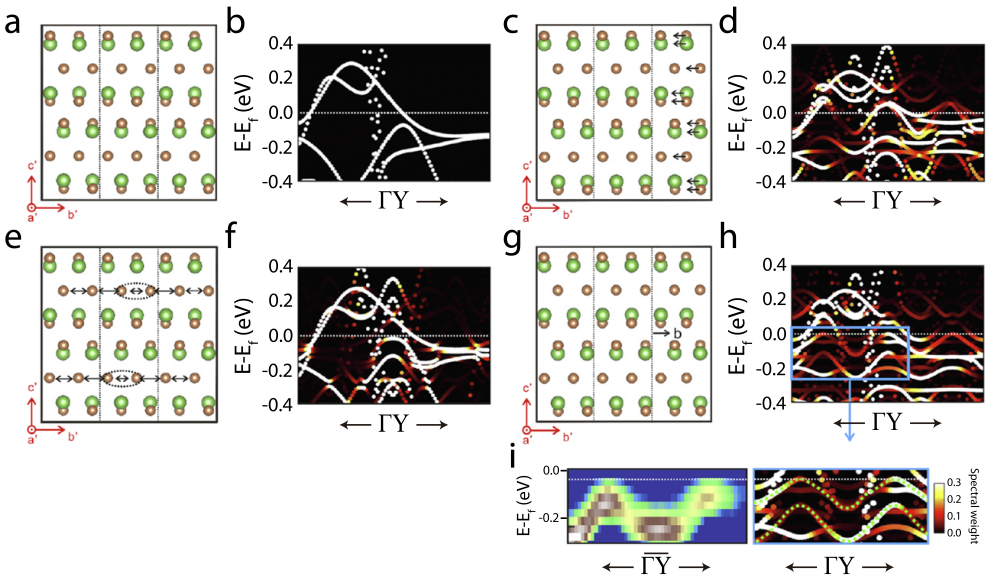

Figure 3.9: $LaSb_2$ supercells with modified atomic positions along the *b'* direction to simulate the CDW periodicity: (c) 0.02 Å displacement of half of the atoms in the cell (those in the right cell), (e) 0.03 Å displacement of the Sb atoms in Sb sheets to introduce a longitudinal-wave-like modification in the Sb sheet and (g) 0.02 Å displacement of the whole middle cell. (d), (f), (h) Unfolded band structures correspond to the modified supercells in (c), (e), and (g), respectively. (i) Comparative between the experimental band structure at 13 K (Fig.3.6d) and the calculated band structure (area indicated with a blue rectangle in panel h).

(Fig.3.9g) accurately models the experimental band folding. Fig.3.9i shows in detail the fair agreement with the experimental 13 K bands. Note the presence of band replicas just below the Fermi level with a dispersion similar to that of the experimental bands. The introduced atomic displacements were in the 0.02-0.03 Å range. Band replicas are difficult to observe for smaller displacements; for considerably larger displacements, the band structure deviates significantly from the original. Because the experimental 13 K bands and FS retain their original form, the structural alterations cannot deviate much from the above-mentioned values.

It is clear that, despite its roughness, the model captures the essential physics of the system. The temperature-driven CDW phase transition in $LaSb_2$ can be traced back to a PLD along the *b'* direction, involving most of the atoms of the conventional unit cell.

3.4 . Conclusions

ARPES measurements revealed changes in the electronic structure of the $LaSb_2$ surface between 200 K and 13 K, including band folding and replicas on the FS. All of these modifications are spectroscopic signatures of the stabilisation of a CDW appearing below 200 K and were observed at 13 K, which is above the temperature at which the superconducting transition starts (2.5 K). The changes in the electronic structure at low temperature are related to a *q* nesting vector ($q = 0.25 \pm 0.02$ Å^{-1}) that connects regions inside the *glasses-like* pockets of the FS along the $\overline{\Gamma Y}$ direction. The results of the DFT calculations allowed us to delve deeper into these findings. The band structure calculations showed that the *glasses-like* pockets, involved in the CDW transition, exhibit La-Sb character. On the other hand, to model the PLD that accompanies the CDW various distorted lattices matching the experimental *q* vector have been tested. A PLD consisting of a 0.02 Å displacement along the *b'* direction and affecting all the atoms in the centre of a 3*b'* supercell reproduced very well the experimental band folding and the spectral weight redistribution; thus, it can be concluded that it is the most probable PLD related to the electronic changes. Additionally, a significant bandwidth reduction was observed at 13 K, suggesting that CDW stabilisation might trigger a Mott transition at lower temperatures. $LaSb_2$ serves as an example of the remarkable strength of electron instabilities. This is illustrated by the fact that even a modest portion of nested FS can suffice to stabilise a CDW at low temperature.

4 - Novel quantum well states in MoS_2

The discovery of graphene and the exploration of its remarkable properties sparked a renewed interest in 2D materials and related layered materials [9]. Many of these 2D materials exist naturally in bulk form, with the bulk comprising a stack of layers held together by vdW interactions. Owing to the weak vdW interaction, these 2D materials are prone to exfoliation into atomically thin layers. As expected, in their monolayer form, these materials exhibit distinct properties compared to their bulk counterparts.

A significant advantage of TMDs compared to graphene is the presence of sizable bandgaps, typically around 1-2 eV, in contrast to the absence of a bandgap in graphene. This property is particularly valuable for applications such as field-effect transistors (FETs), where on/off switching is essential. While it is possible to induce a bandgap in graphene, it often leads to low on/off switching ratios, presenting challenges in graphene-based implementations. On the other hand, while this issue is naturally absent in TMD, they have lower carrier mobility than graphene, which requires further improvement for real applications. [137, 138].

As presented in Chap.1, MoS_2 lies at the core of the TMDs family. In terms of its electrical conductivity, MoS_2 behaves as a semiconductor whose properties are highly influenced by factors such as thickness, strain, stacking order and gating. The transition from bulk to monolayer MoS_2 results in a significant shift in its electronic properties. In its bulk form, MoS_2 is as an indirect bandgap semiconductor with a bandgap of 1.2 eV, while in its monolayer form, it is a direct bandgap semiconductor with a bandgap of 1.9 eV. This transition unlocks a realm of possibilities for optoelectronic applications, including photodetectors and light-emitting devices [139]. The precise tuning of energy levels near the Fermi level becomes crucial for optimizing the performance of these devices. This is evident in applications such as optical waveguides, where confinement is used to select propagating modes of light [140], and in solar cells, where MoS_2 can serve as a charge transport layer by engineering the band alignment [141–144].

Expanding our understanding of MoS_2 not only unveils fundamental insights into two-dimensional physics but also paves the way for transformative technological opportunities. For instance, the phenomenon of quantum confinement experienced by electrons in few-layer MoS_2 not only facilitates tunable bandgap engineering but also provides an avenue to investigate fundamental quantum phenomena. Quantum confinement arises in solid-state systems when one dimension of the material is of the order of the Fermi wavelength. In-plane quantum confinement has

been observed in various setups such as quantum corrals [145] and Fabry-Pérot resonators [146] using STM. Out-of-plane confinement in ultrathin films has also been observed, particularly through techniques like PES [147–151].

4.1 . Crystalline structure

MoS_2 exhibits various crystalline polytypes, each of them with distinct structural and electronic properties. Among these polytypes, the most well-known are the 2H, 1T and 3R phases (see Fig.4.1). Common to all these polytypes are the three honeycomb hexagonal sheets of Mo and S (S-Mo-S). These three sheets, with strong covalent bonds between them, form an indivisible unit. In the literature, and this work, we will refer to this assembly as a monolayer. When two or more monolayers are held together, they are weakly bound by vdW forces [152].

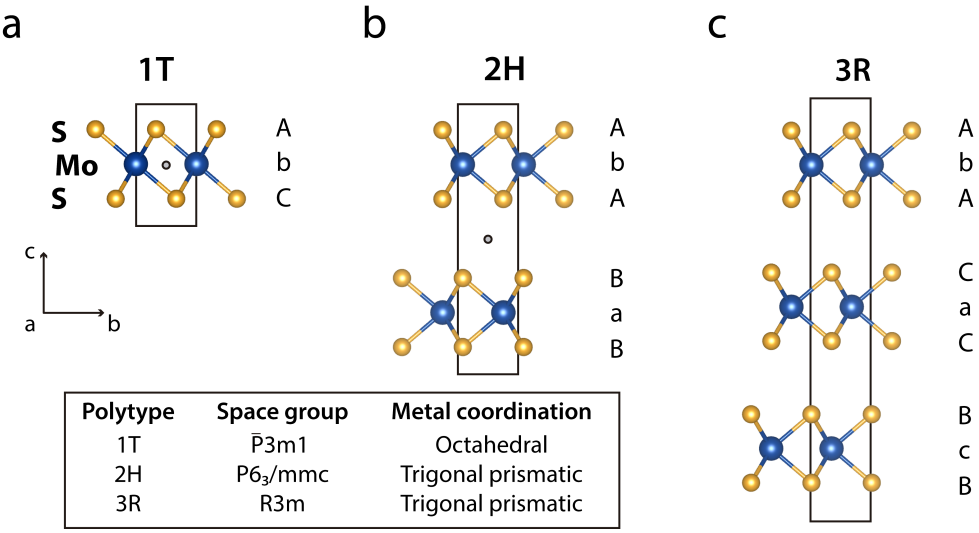

Polytype	Space group	Metal coordination
1T	$\bar{P}3m1$	Octahedral
2H	$P6_3/mmc$	Trigonal prismatic
3R	R3m	Trigonal prismatic

Figure 4.1: Scheme of the three most common MoS_2 crystalline polytypes. Mo atoms (blue), S atoms (orange) and inversion symmetry centre (grey dot). (a) Metallic 1T phase. The S lattices within the S-Mo-S are not vertically stacked, resulting in octahedral coordination. (b-c) Semiconducting 2H and 3R phases, respectively. The phases share an S-Mo-S slab, but the stacking sequence differs. Note that the 3R phase lacks an ISC irrespective of the number of layers considered, whereas in the 2H phase, the ISC exists only for an even number of layers.

As mentioned earlier, changes in layer thickness dramatically influence the electronic structure but beyond this, MoS_2 also responds to mechanical stress, resulting in bandgap size and carrier mobility tuning [153–155]. Its weak vdW forces allow for the engineering of heterostructures by stacking different TMDs or other 2D materials, leading to the creation of unique electronic properties and excitonic behaviours [16, 143, 156, 157]. Additionally, MoS_2 can be influenced

by external fields like electric and magnetic fields, providing control over carrier concentration and conductivity [158, 159]. The electronic properties can also be manipulated by introducing foreign atoms or molecules into the lattice, a crucial aspect for specific applications such as catalysis [160, 161].

The 1T phase (Fig.4.1a) is the least prominent phase among all because it is thermodynamically metastable. The crystalline ordering is formed by a trilayer slab with non-vertically aligned S lattice atoms forming a trigonal prismatic coordination around molybdenum, leading to a metallic electronic structure [162, 163]. It is possible to stabilise the 1T phase from the 2H [164], triggering an insulator-to-metal transition. For this reason, many efforts have been undertaken to control the phase modulation [164].

Fig.4.1 b-c show the 2H and 3R phases. Both structures share the same S-Mo-S slab but differ in the slab stacking sequence. Despite these differences and because Mo coordination is maintained, both polytypes are semiconducting. The 2H and 3R phases are naturally available, however, due to thermodynamic reasons almost all MoS_2 crystallises in the 2H phase. Therefore, many studies have been devoted to synthesising the 3R phase and, more interestingly, manipulating the widely available 2H phase by triggering the phase transformation [165].

In this work, we have centred our attention on the most commonly found 2H phase. 2H MoS_2 has the following lattice parameters: a = b = 3.161 Å, c = 12.295 Å with an interlayer distance of 6.15 Å [166, 167]. Bulk MoS_2 crystals, with micrometric-size domains, can be mined geologically and further prepared in the laboratory. Samples with a controlled thickness ranging from 1 monolayer to the bulk can be synthesised. The work of Sun et al. [168] reviews exhaustively a broad variety of available methods of synthesis.

4.1.1 . Doping

The majority of studies investigating the conductivity nature of MoS_2 frequently observe an n-type conductivity and emphasize its unipolar doping tendency [169–171]. These studies suggest that various factors contribute to this n-type conductivity, such as impurities [172], native defects [173] and Fermi level pinning [174]. Among these factors, native defects like sulfur vacancies have been identified as the primary cause of the observed conductivity, primarily attributed to their low formation energy [99, 175]. However, since the role of defects in electrical conductivity is not clear, the reported n-type conductivity has been controversial in the literature, occasionally showing both p-type and n-type conductivity (sometimes even within the same work [137, 138]).

Recent experimental [176–178] and theoretical [99, 175, 179–181] studies have

questioned the predominant explanation for n-type conductivity in MoS_2, suggesting that the presence of sulfur vacancies is not the cause of the n-type conductivity. Instead, these studies argue that the presence of carbon impurities is at the origin of the n-type conductivity. Furthermore, the studies demonstrate that a clean MoS_2 surface exhibits intrinsic behaviour and suggest that overlooking the carbon impurity has led to the erroneous assumption of n-type conductivity.

Despite this ongoing debate, there has been a pursuit to achieve controlled and stable p-type conduction in MoS_2 so that FETs can be realized [182–184]. Substituting the metal atom has been suggested theoretically [185] and emerged as an efficient path for this purpose [186–189], given its relative simplicity and avoidance of complex preparation processes that often lead to poor reproducibility. Particularly, Nb stands out as the most suitable substitutional acceptor dopant for MoS_2. This preference arises from the shared 2H structure between MoS_2 and NbS_2, resulting in nearly identical lattice parameters. Consequently, substituting Mo atoms with Nb atoms has a negligible impact on the overall crystalline order. The quality of the doped crystals has been thoroughly examined by XRD, Raman and scanning transmission electron microscope (STEM), resulting in an outstanding quality for dopant concentrations under $3.1 \cdot 10^{17}$ cm^{-3} [187].

This work extensively employs MoS_2-Nb doped crystals with $\sim 2 \cdot 10^{17}$ cm^{-3} of Nb concentration (i.e., $\sim$ 0.001 at.%). Fig.4.2a shows a low-energy electron microscope (LEEM) image of a MoS_2-Nb doped sample prepared via mechanical exfoliation. The uniform contrast observed throughout the image at a large field of view is indicative of a constant value of the crystal's work function. This demonstrates that the material's surface is electronically homogeneous after the preparation process. Fig.4.2b presents a LEED pattern in the selected area indicated in panel (a). The sharp hexagonal pattern, corresponding to the 2H phase, demonstrates the high quality of the crystal structure at the surface. As it will be explained later, the primary aim behind incorporating doped samples is to augment the catalytic activity of MoS_2, an aspect of critical importance described in Chap. 5.

In addition to catalytic enhancement, doping improves the sample's conductivity and consequently offers an additional advantage, which is to avoid sample charging effects. This is particularly relevant in PES experiments with semiconducting samples. Sample charging effects arise when photoelectrons leave the sample surface, creating a positive charge imbalance [190]. If not accounted for, this charge accumulation can distort experimental measurements mainly due to two effects: a reduction of the kinetic energy of the photoelectrons and a significant alteration of the peak shapes. The first effect causes misleading peak shifts. The shifts can be easily corrected by referencing the spectrum to the adventitious C 1s peak and/or to a feature of a metal in electrical contact with the sample (e.g., the

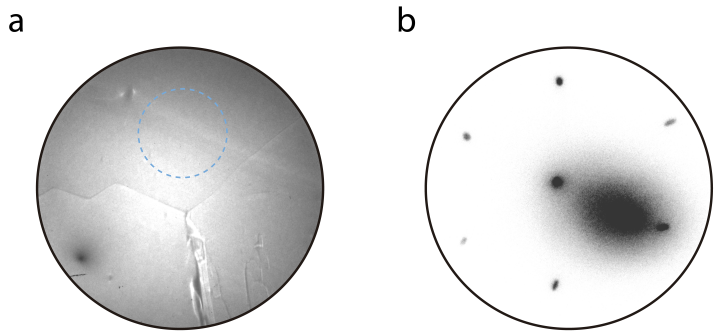

Figure 4.2: (a) LEEM image of a MoS_2-Nb doped sample. The LEEM image field of view is 50 µm and were acquired with a start voltage of 5 V. (b) Hexagonal LEED pattern at 45 eV of the area indicated by a dotted circle in (a). The LEEM image and LEED pattern were measured at the Instituto de Química Física Blas Cabrera (Madrid) with the collaboration of Dr. Juan de la Figuera and Dr. Jose Emilio Prieto.

Fermi level, Au $4f_{7/2}$). However, the second effect results in a meaningless and non-correctable spectrum.

Thus, the utilization of Nb-doped samples offers advantages by effectively addressing sample charge-related challenges. Additionally, given that conducting measurements at low temperatures is a common practice in PES to reduce thermal broadening, special consideration is needed when studying semiconductors with this technique at low temperatures, due to the inherent tendency of semiconductors to exhibit reduced conductivity at low temperatures. Consequently, employing Nb-doped samples can be beneficial, as it assists in mitigating sample charge issues, ensuring reliable and accurate PES measurements.

4.2 . Electronic structure

In this section, we present the ARPES electronic structure of both pristine and Nb-doped MoS_2. A comprehensive discussion of the pristine electronic structure is undertaken to establish a foundation for the following topics, such as the QWS presented in this chapter, as well as the boosting of the hydrogen adsorption in Chap.5.

4.2.1 . Valance band

4.2.1.1 Experimental determination

The measurements comprising the following sections were conducted at the URANOS and CASSIOPÉE beamlines, and the specific experimental details regard-

ing the beamlines can be found in Sec.2.2.1. Before measurements, the samples were prepared following the methods outlined in Sec.2.3. Both MoS_2 and Nb-doped MoS_2 (0001) crystals were mechanically exfoliated under Ultra-High Vacuum (UHV) conditions (at a pressure $\sim 2 \cdot 10^{-10}$ mbar). All spectra presented were obtained using light linearly polarised in the horizontal plane and conducted at a temperature of 110 K unless otherwise indicated.

Fig.4.3 displays the hexagonal bulk (BZ) and its high-symmetry points corresponding to the 2H crystalline structure. The associated surface Brillouin zone (SBZ) is presented at the top. The SBZ results of projecting the ARPES parallel momentum measured at a fixed perpendicular momentum onto a plane. Consequently, the choice of photon energy yields different flat sections of the BZ (see Eq.2.10).

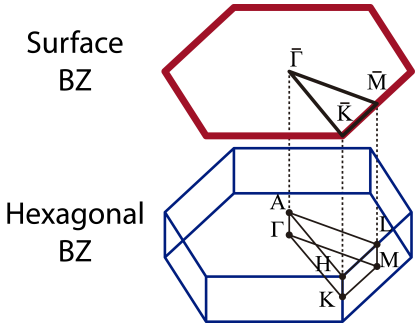

Figure 4.3: Hexagonal BZ (blue line) and its high-symmetry points. On top, is the projected SBZ (red line).

Fig.4.4a shows a three-dimensional representation of an undoped MoS_2 ARPES intensity across the entire scanned reciprocal space. The dispersion of the VB along high-symmetry directions is depicted in Fig.4.4b. Notably, the valence band maximum (VBM) is situated at $\overline{\Gamma}$ (-0.74 eV), whereas a local maximum occurs at $\overline{K}$ (-1.38 eV). The energy difference between these two maxima, $\Delta E = E^{\Gamma}_{max} - E^{K}_{max}$, is 0.64 eV, in accordance with expectations for a bulk-like sample [34]. Fig.4.5a-b presents a set of constant energy maps (CEMs) showing the MoS_2 electronic structure at higher binding energies. The CEMs highlight the hexagonal symmetry and the trigonal wrapping around the K-points.

As mentioned, the nature of MoS_2 conductivity has been a subject of controversy, which complicates comparisons with earlier ARPES findings. The sensitivity of MoS_2's band structure to preparation methods has led to a wide range of reported VBM values (-0.7 to 1.12 eV) in previous works [34, 176–178, 191, 192]. In this work, the MoS_2 samples have displayed a VBM trend that is consistent with the results reported in the work of Han et al. [176] and Park et al. [177]. Specifically, freshly exfoliated surfaces exhibit a VBM around -0.74 eV, resulting in fairly intrinsic behaviour given that the band gap is ~ 1.2 eV [192].

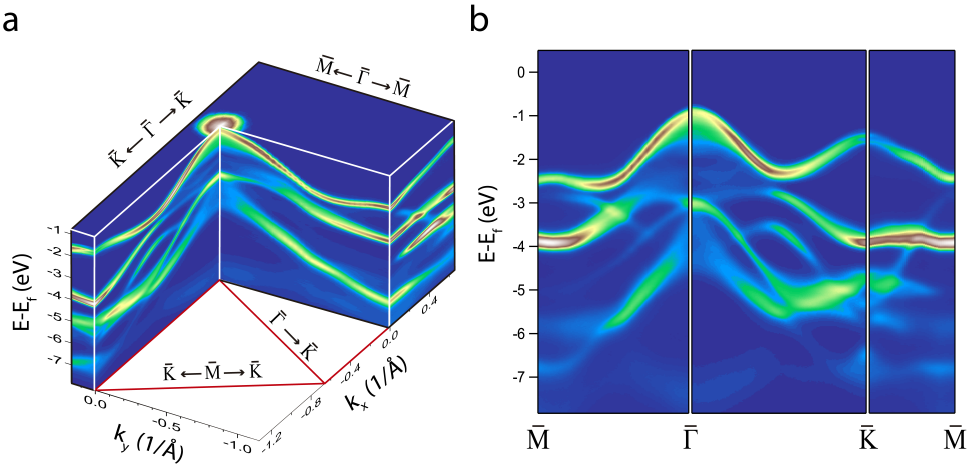

Figure 4.4: (a) MoS_2 3D ARPES intensity vs. energy and parallel momentum (k_x and k_y) centred at $\bar{\Gamma}$ (b) ARPES intensity showing the band structure along the $\overline{\text{M}\Gamma\text{KM}}$ high-symmetry points path. Data were taken at 12 K and with $h\nu = 70$ eV photon energy.

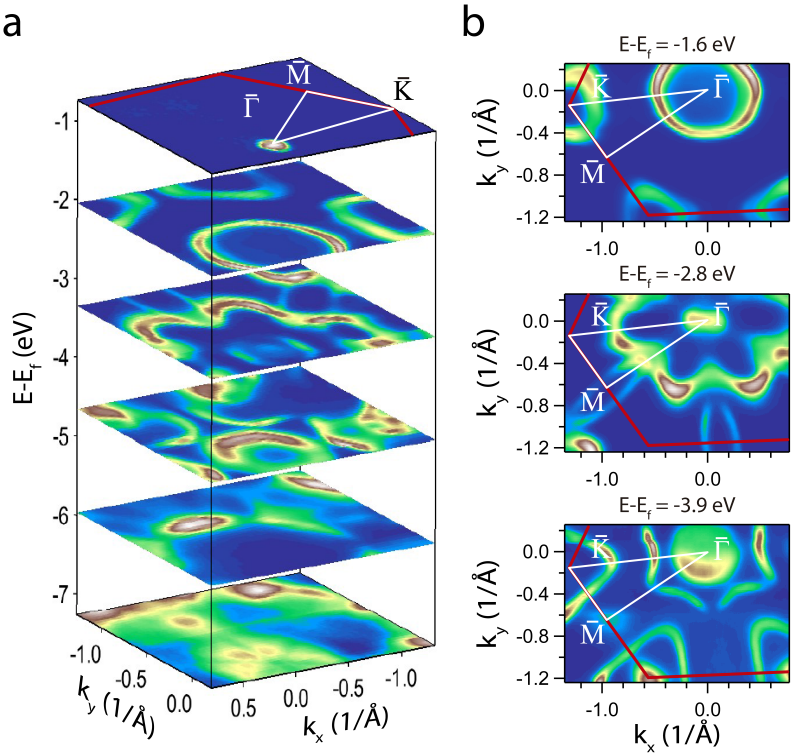

Figure 4.5: (a) Stack and (b) selection of CEMs at different binding energies extracted from the full ARPES map in Fig.4.4a. The red line indicates the SBZ. Data were taken at 12 K and with $h\nu = 70$ eV photon energy.

In Fig.4.6a-b, the ARPES dispersion of the VB along the $\overline{\Gamma K}$ direction is presented for both an undoped sample and an Nb-doped sample, respectively. As expected, the Nb doping produces a rigid shift of the VB towards the Fermi level, indicative of p-type doping. No significant alterations of the band shape are observed. The quantification of the rigid shift is presented in Fig.4.6c. To this end, an EDC at $\overline{\Gamma}$ was taken in the undoped (Nb-doped) sample. We found a VBM energy difference between the samples (ΔE_{VBM}) of 0.63 eV.

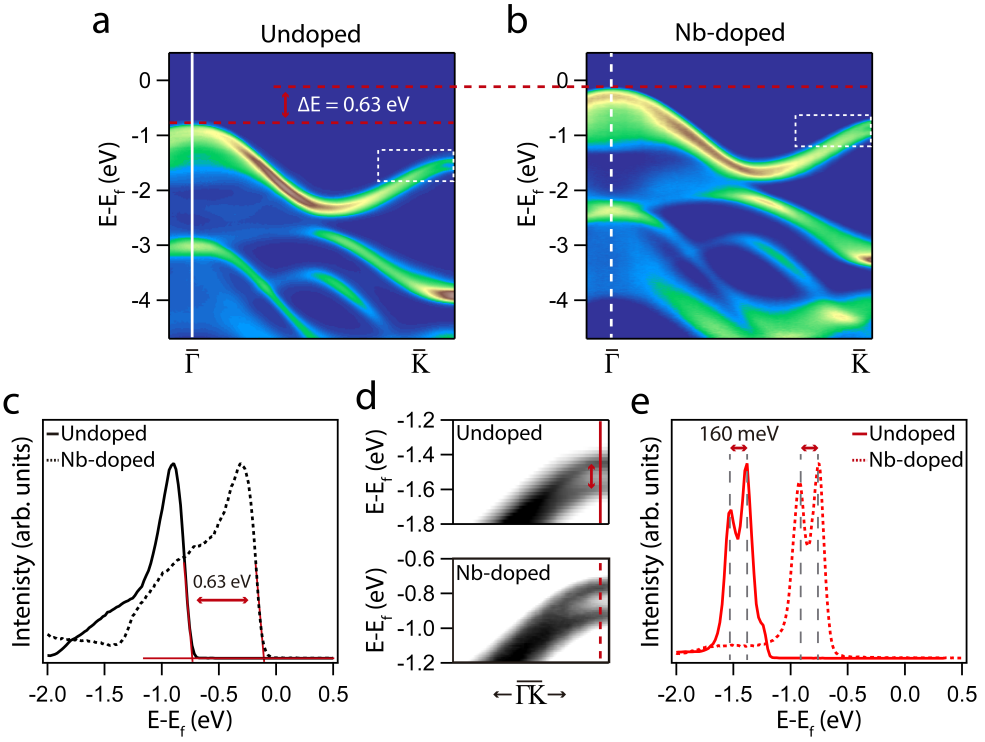

Figure 4.6: (a-b) ARPES intensity showing the dispersion along the $\overline{\Gamma K}$ direction for the undoped and Nb-doped samples, respectively. The aceptor dopant density is $N_a \sim 2 \cdot 10^{17}$ cm^{-3}. (c) EDCs at $\overline{\Gamma}$ marked in (a-b) showing the VBM determination of the undoped (white continuous line) and Nb-doped (white dashed line) samples. A rigid band shift (ΔE_{VBM}) of 0.63 eV towards the Fermi level is obtained. The EDCs integrates a $\Delta k_{\|} = 0.1$ Å^{-1} region centered at $\overline{\Gamma}$. The normalisation and VBM estimation were done according to Appx.A.2. (d) Detail of the ARPES intensity around $\overline{K}$ of the undoped (top) and Nb-doped (bottom) samples highlighting the splitting at this point. The displayed region corresponds to the white dashed boxes in panels (a-b). (e) EDCs at $\overline{K}$ marked in (d) showing a ΔE_{SOC} of 160 meV in the undoped (red continuous line) and Nb-doped (red dashed line) samples. The EDCs integrates a $\Delta k_{\|} = 0.06$ Å^{-1} region centered at $\overline{K}$.

The very high crystalline quality of the samples allowed us to observe the spin split bands around the K-point at an energy of -1.38 eV and -0.76 eV, in the undoped and Nb-doped sample, respectively (see Fig.4.6d). This characteristic split stands as a hallmark of the TMDs family, observing the splitting at $\overline{K}$ demonstrates

both high crystal quality and good sample preparation. Clean, flat surfaces are necessary to reduce scattering, preserving the angle-resolved information of the photoelectrons and consequently allowing well-resolved states with large parallel momentum. The magnitude of the splitting is proportional to the strength of the spin-orbit coupling (SOC) [159, 193]. Fig.4.6e shows the quantification of the spin splitting. For this purpose, an EDC was taken at $\overline{\text{K}}$ in the undoped (Nb-doped) sample, the EDC is marked as a red continuous (dashed) line in Fig.4.6a (Fig.4.6b). The observed spin splitting (ΔE_{SOC}) is 160 meV, in agreement with previous results [192].

4.2.1.2 Theoretical calculations

A solid understanding of the atomic orbitals that originate the VB of MoS_2 is essential for comprehending how the electronic structure changes due to the structural modifications pursued in this work. Initially, this understanding can be developed by considering the crystal field theory (CFT). According to the CFT, ligands in transition metal compounds break the degeneracy of d or f orbitals. For 2H MoS_2, where Mo is in trigonal prismatic coordination, the Mo $4d$ orbitals are split into five orbitals: dyz, dxz, d_{xy}, $d_{x^2-y^2}$, d_{z^2} (see Fig.4.7a). The framework of the CFT adequately accounts for the semiconducting character of MoS_2 and the metallic behaviour of neighbouring group VB chalcogenides with "one electron less" (e.g., NbS_2, TaS_2, etc.).

However, the predicted energy gap between the occupied d_{z^2} and unoccupied d_{xy}, $d_{x^2-y^2}$ states notably deviates from the experimentally observed gap values for several TMDs [194]. Furthermore, the CFT falls in explaining the thickness-dependent band gap and the direct-to-indirect band gap transition, consisting in a shift of the VBM from K (direct) to Γ (indirect). To attain a complete understanding of how interlayer interactions affect the VB structure, it is crucial to consider the hybridization of the Mo 3*d* and S 2*p* orbitals [194].

Before delving into the electronic structure details, understanding how the electronic orbitals are oriented in real space proves illustrative. Fig.4.7b shows the shape and orientation of the valence orbitals at three k-space points: Γ, M, and K for a MoS_2 monolayer. Two contrasting situations can be observed: the Γ-point is dominated by Mo d_{z^2} and S p_z orbitals that exhibit an out-of-plane orientation of the charge density, while the K-point is dominated by Mo $d_{x^2-y^2}$ orbital, exhibiting in-plane orientation of the charge. The M-point lies in the middle of these two situations combining Mo d_{z^2}, $d_{x^2-y^2}$ and S p_z orbitals. Therefore, an out-of-plane to in-plane change in the VB orbital character of the space charge density orientation is observed when going from Γ to M to K points.

Despite the weak nature of the vdW interaction, this interaction can substantially modify the electronic structure [153]. For instance, Fig.4.7c shows the changes in the orbital shape at Γ for a bilayer concerning a monolayer. The blue-dotted box highlights the changes in the orbital shape at the interlayer region. Given the localization of the d states, a bonding-anti-bonding state pair forms when the orbitals of the two layers overlap, splitting the upper VB at $\Gamma \sim 0.6$ eV [34]. The resulting overlapped orbitals retain a highly directional out-of-plane orientation, favouring interlayer electron sharing.

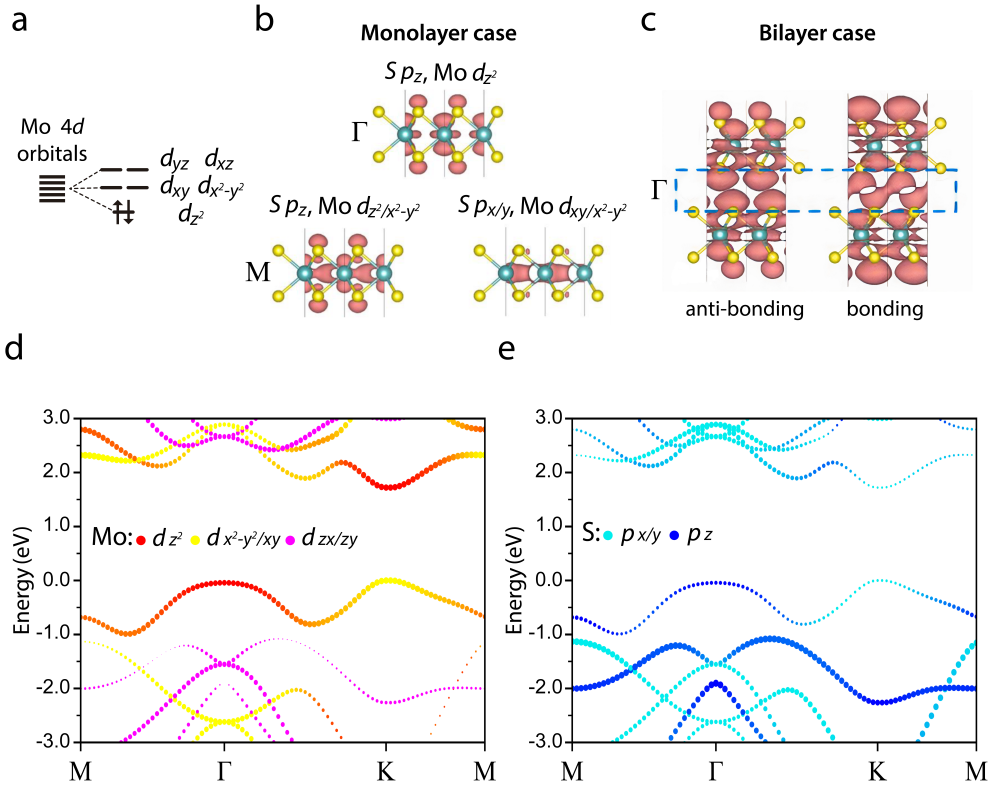

Figure 4.7: (a) Mo $4d$ energy level diagram showing the CFT splitting of the five levels. (b) Visualised wavefunction norms of the upper VB at the Γ, M and K points of a monolayer. The displayed Mo and S orbitals are labelled on each panel. (c) Visualised wavefunction norm of the upper VB at the Γ for a bilayer. A bonding and anti-bonding state is shown along a dotted blue box region that highlights the orbital modifications at the interlayer region. (d-e) DFT orbital-projected electronic band structures calculated for a MoS_2 monolayer along the MΓKM phat. The five Mo $4d$ orbitals are grouped as: d_{z^2} (red), $d_{x^2-y^2} + d_{xy}$ (yellow) and $dzx + dzy$ (magenta). The three S $2p$ orbitals are grouped as: $p_x + p_y$ (cyan) and p_z (blue). The symbol size is proportional to the weight of the state. The graphics in (b-c) are adapted from [195].

Each time a new layer is considered, a band splitting takes place to break the degeneracy. As a result of this, the number of split bands coincides with the number of layers [34]. Consequently, the band gap progressively decreases from

1.9 eV (monolayer) to 1.2 eV (bulk). The transition to the bulk bandgap value is fairly quick, taking place within approximately 3-4 monolayers. Simultaneously, the initial 1.9 eV energy separation between occupied and unoccupied states at K remains largely unaltered.

Fig.4.7d-e shows the DFT orbital-projected electronic structure of the Mo $4d$ and S $2p$ orbitals in a MoS_2 monolayer, respectively. The calculations were carried out by Dr. Cesar González, a collaborator from the Dto. de Física de Materiales, UCM, Madrid[1]. The mentioned change in the topmost VB orbital character is observed in the calculations, consistent with the description given for Fig.4.7b. The moderate presence of S p_z orbital is evident at Γ and M points while being minimal at K point. Despite its moderate contribution to the topmost VB states, the hybridized S p_z orbital plays a role in interlayer bonding.

Fig.4.7d-e illustrates that, for a monolayer, the band gap is direct and positioned at K. This straightforwardly arises from the dominance of in-plane character of the Mo $d_{x^2-y^2}/xy$ orbitals at K point, the preferred direction for transport due to two-dimensionality. Conversely, the states around Γ point, comprising of out-of-plane Mo d_{z^2} and S p_z orbitals (red dots) will bear with interlayer coupling effects. Finally, SOC was not included in the calculations explaining the absence of band splitting at the K-point. The splitting at K in a monolayer is explained based on SOC affecting the orbits of the electrons in the in-plane direction ($d_{x^2-y^2}/xy$) [193]. However, the presence of more than one layer complicates the description of this phenomenon, as interlayer coupling influences the spin splitting [196].

It is important to remark here that, while the MoS_2 band structures of this work were calculated for a monolayer, the ARPES measurements were done in bulk-like samples. Nevertheless, as can be seen, the overall band structure retains its fundamental characteristics in both cases and calculations for a monolayer are faster and computationally less costly, allowing for the investigation of a greater variety of scenarios.

4.2.2 . Core-levels

In Fig.4.8a-b we depict the X-ray photoemission spectroscopy (XPS) Mo $3d$ and S $2p$ series of CLs for both the undoped and Nb-doped samples. Three peaks are identified after fitting the spectrum of Fig.4.8a. In the undoped (Nb-doped) sample, the S $2s$ peak is observed at 226.41 eV (225.93 eV), the Mo $3d_{5/2}$ peak at 229.21 eV (228.73 eV), corresponding to Mo^{+4} oxidation state in MoS_2, and a minor peak, the Mo $3d_{3/5}$ at 232.35 eV (231.83 eV), due to Mo^{+6} oxidation state in MoO_3. The presence of MoO_3 can be attributed to the use of MoO_3 as a

[1]For detailed calculation methods, refer to Appx.A.3.

precursor agent during the CVT process. Fig.4.8b presents the S $2p$ peak and its corresponding fitting. In the undoped (Nb-doped) sample, the S $2p_{3/2}$ component is at 162.05 eV (161.54 eV).

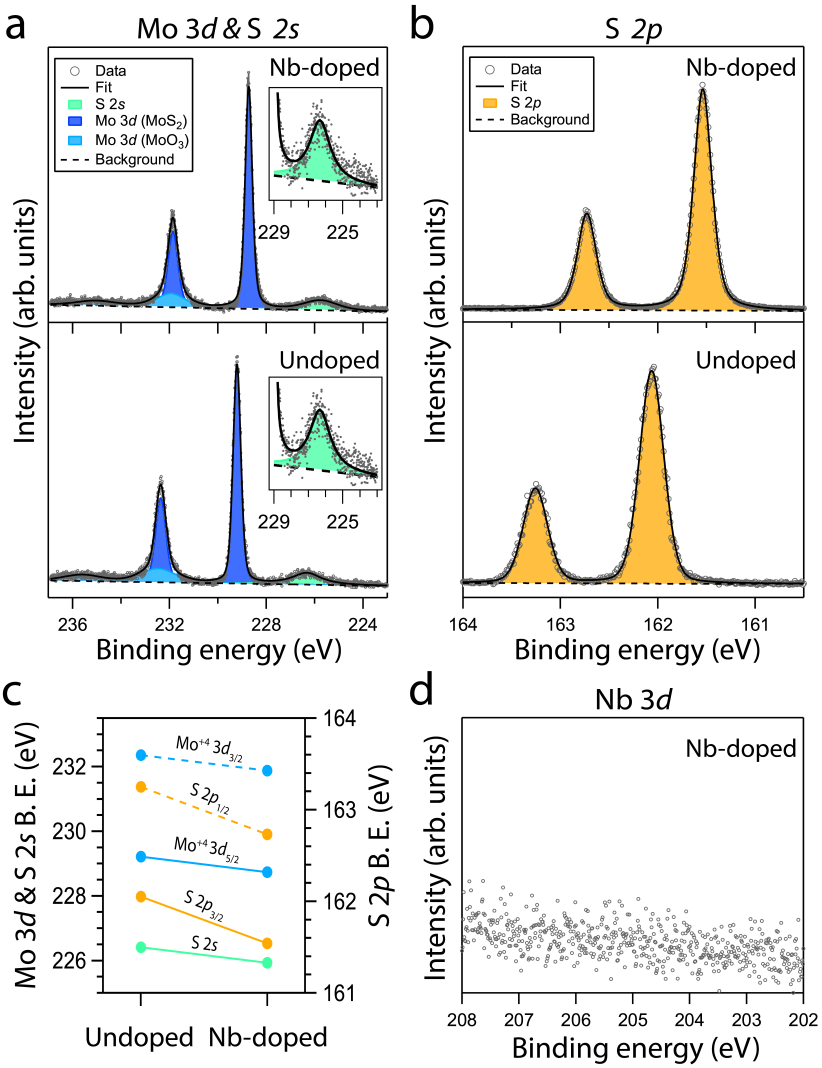

Figure 4.8: XPS CLs of the undoped and undoped MoS_2 samples. (a) Mo $3d$ & S $2s$. Inset: S $2s$ ($h\nu = 400$ eV). (b) S $2p$ ($h\nu = 200$ eV). (c) Summary of the peak shifts of the fitted components in (a-b). (d) Nb $3d$ ($h\nu = 400$ eV).

A summary of the peak shifts is presented in Fig.4.8c, for the main MoS_2 CL peaks: 0.48 eV for Mo $3d_{3/5}$ and 0.51 eV for S $2p$. The relatively low Nb concentration yields a p-type shift of similar magnitude to the ones in the referenced works [186, 187]. It is important to note that no Nb $3d$ signal was detected in any of the doped sample batches employed in this work (see Fig.4.8d). As said before, the Nb doping concentration is $\sim$0.001 at.% (i.e., $\sim 2 \cdot 10^{17}$ cm^{-3}), so it is notably lower in comparison to concentrations used in other works [186, 187].

In these studies, for a doping concentration of 0.5 at.% and higher, well-resolved Nb $3d$ CL is detected.

So, on this basis, and considering the very low level of Nb doping, we cannot expect changes in the VB due to Nb doping. Both undoped and doped samples exhibit similar characteristics regarding the VB shape.

4.3 . Quantum well states

In Sec.4.2.1.2 it was indicated that interlayer interaction induces band splitting around $\overline{\Gamma}$, resulting in the appearance of additional bands. These additional bands aroused around Γ since its states are mainly composed of out-of-plane oriented orbitals through which electron-hopping is possible. As a result, the topmost band around the Γ-point disperses in k_z. Furthermore, theoretical calculations performed for a specific number of layers also predict the presence of these additional features [154, 197–200].

Fig.4.9 presents the ARPES intensity of two samples prepared via mechanical exfoliation, the samples were obtained from the same crystal. Panel (a) exemplifies the pristine MoS_2 dispersion commonly found in the literature [34, 201–203]. An EDC at $\overline{\Gamma}$ is presented at the right side of panel (a), indicating the intensity maximum of the bulk band. Conversely, in panel (b), the emergence of a modulated spectral weight is observed at and in the vicinity of the $\overline{\Gamma}$ point. The EDC at the right side of panel (b) indicates that the spectral weigh has the form of additional discrete bands (ADBs).

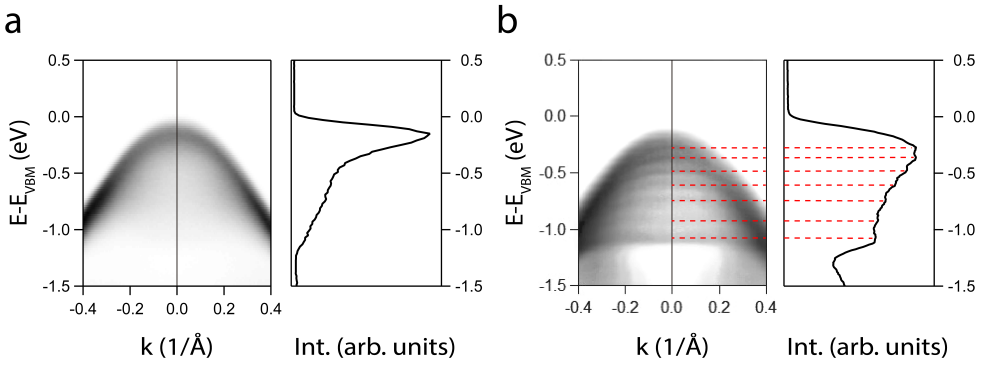

Figure 4.9: ARPES intensity of the VB parabolic convex dispersion of the bulk band centred at $\overline{\Gamma}$ along the $\overline{\Gamma K}$ direction for different MoS_2 samples. (a) Absence of ADBs. (b) Presence of ADBs. An EDC centered at $\overline{\Gamma}$ is presented at the right side of each panel. The data was taken with $h\nu = 70$ eV photon energy maintaining the same experimental geometry.

Fig.4.10 shows a series of curvature intensities[2] of the parabolic convex dispersion centred at the $\overline{\Gamma}$ point along the $\overline{\Gamma K}$ direction, of different samples. Panel (a) shows the absence of ADBs, while in panels (b-f) a different number of ADBs beneath the $\overline{\Gamma}$ parabola can be observed. This is surprising, as the sample origin, preparation and experimental measurement conditions were, at best, the same. An integer index (n) is used to label the ADBs, with increasing n corresponding to higher binding energies. A set of red dashed lines are drawn, marking the energy position of the ADBs at $\overline{\Gamma}$. The energy difference between adjacent ADBs is defined as $\Delta E = E_{n+1} - E_n$. The spectra are labelled and sorted according to the maximum number of ADBs observed (n_{max}). A trend can be observed as n_{max} increases: the ADBs ΔE decreases, while the $n = 1$ band becomes less bounded (lower binding energy). This behaviour is characteristic of a quantum well (QW), where a discrete set of energy levels (quantum well states (QWS)) occur. In this context, the number of QWS and their energy spacing are influenced by the well width (L). As L diminishes, the available states decrease, leading to greater separation between levels. Additionally, the energy of the fundamental state ($n = 1$) shifts as L decreases, resulting in a more bounded state.

To confirm that the ADBs are QWS we should check its k_z dispersion. It is possible to prove this aspect through ARPES measuring at different photon energies. In Fig.4.11a-c a photon energy of hν = 40, 70, and 100 eV for $n_{max} = 7$ was used to measure the ADBs, respectively. Similarly, Fig.4.11d-e presents the $n_{max} = 1$ case, where hν = 50 and 70 eV were used. Fig.4.11f provides a summary of the ADBs energies, which allows to quantify its behaviour. The energy error bar is estimated as the average of the full width at half maximum (FWHM) from the observed features, while the FWHMs were extracted from an intensity profile at $\overline{\Gamma}$. It can be seen that the energies of the ADBs do not significantly change with photon energy, implying that the ADBs do not disperse in k_z. Concomitantly, modulation of the intensity as the photon energy changes (matrix element) is noticeable when comparing the n_{max} cases at different photon energies. Particularly, Fig.4.11c show that the intensity of the ADB $n = 1$ is drastically reduced. Its energy, marked with a white dashed line, is deduced from the $n = 1$ in Fig.4.11a-b because the ADBs do not disperse. Thus, due to all the mentioned characteristics, the ADBs in Fig.4.10b-f can be recognized as QWS within a few-layer MoS_2 stack.

A relevant aspect concerning the QWS is its energy dependence on the quantum number, n, which directly depends on the potential profile of the QW. Fig.4.12a displays the energies of the QWS versus n of Fig.4.10. Interestingly, a linear relationship between E_n and n can be fitted for each n_{max} sample. Fig.4.12b displays the obtained ΔE values, showing that ΔE converge to roughly constant

[2]For clarity in visualizing spectroscopic characteristics with varying intensities, the data were processed using the curvature method (see Sec.2.2.3). The VBM is used as the energy reference for convenience, as is customary for semiconductors.

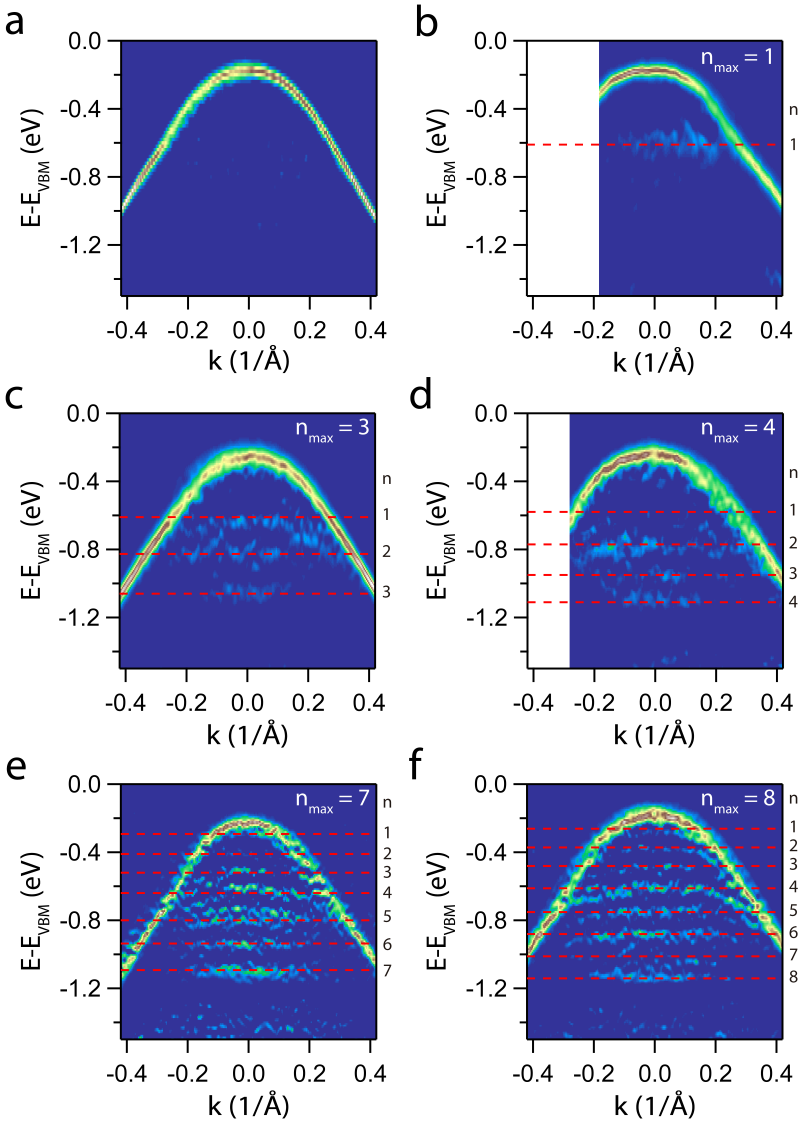

Figure 4.10: Curvature intensity of the VB parabolic convex dispersion of the bulk band centred at $\overline{\Gamma}$ along the $\overline{\Gamma K}$ direction for different MoS_2 samples. (a) "Perfect" sample. (b-f) Samples showing ADBs. The side integers correspond to the index n, used to count the ADBs. The spectra are sorted according to the maximum number of ADBs $n_{max} = 1, 3, 4, 7, 8$ respectively. The red dashed line marks the ADBs energy at $\overline{\Gamma}$ as a guide. The data was taken with $h\nu = 70$ eV photon energy maintaining the same experimental geometry.

energy, owing to the linear relationship between E_n and n previously fitted. Additionally, a dotted line is drawn to indicate that as n_{max} increases, ΔE monotonically decreases. This is a behaviour customary for QWS. In the present case, the linear dependence between E_n and n differs from that expected for a quantum well with infinite energy walls (i.e. an infinite quantum well). Indeed, in an infi-

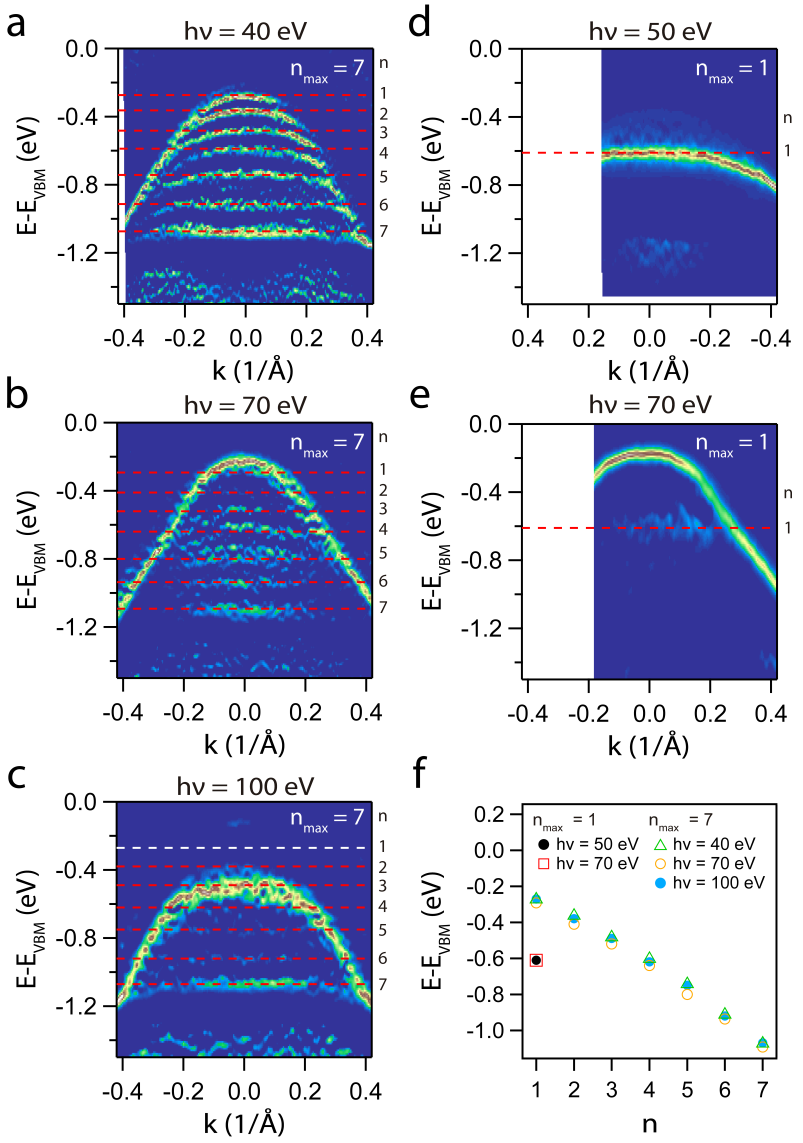

Figure 4.11: Curvature intensity of the parabolic band centered at $\overline{\Gamma}$ along the $\overline{\Gamma K}$ for different photon energies. The $n_{max} = 7$ assembly was measured at: (a) $h\nu = 40$ eV, b) $h\nu = 70$ eV, (c) $h\nu = 100$ eV. The $n_{max} = 1$ assembly was measured at: (d) $h\nu = 40$ eV and (e) $h\nu = 70$ eV. The side integers correspond to the index n, used to count the ADBs. The red dashed line marks the ADBs energy at $\overline{\Gamma}$ as a guide. The intensity of the $n = 1$ in (c) was reduced. The white dashed line marks its energy, deduced from (a-b). (f) Energy vs. ADBs for the $n_{max} = 1, 7$ cases at the indicated photon energies. In (f) the energy error is ± 150 meV, calculated as an average of the FWHM of all the QWS.

nite quantum well, the energy of the QWS holds the relationship: $E_n \propto n^2/L^2$, indicating a quadratic dependence between E_n and n.

Hence, the shape of the potential well within the few-layer MoS_2 assembly

deviates from the simple infinite QW model. On the other hand, a parabolic QW potential for electrons confined perpendicular to the surface would yield equally spaced QWS [204] such as those we have observed here. Allowing us to conclude that the potential profile of the few-layer assembly follows a parabolic shape.

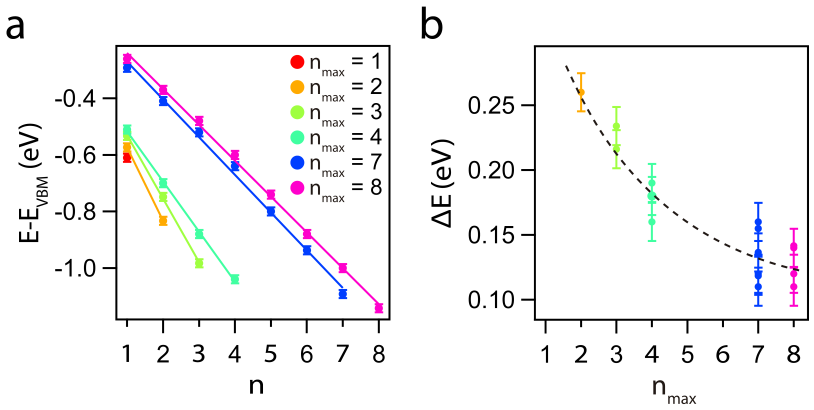

Figure 4.12: (a) QWS energy versus n, for the $n_{max} = 1-4, 7, 8$ cases. The coloured lines correspond to a linear fit for each of the n_{max} cases. (b) ΔE versus n_{max}. From each n_{max} sample it can be extracted $n_{max} - 1$ ΔE values. The dashed line is a guide indicating the decrease in ΔE as the number of QWS per n_{max} increase.

To explain the appearance of QWS in some samples, we propose that the formation of a few-layer MoS_2 assembly occurs naturally with the sample preparation method employed. Mechanical exfoliation is a straightforward sample preparation technique that has continued evolving since its first report [9] and has progressively become sophisticated [205]. Throughout this process, limited attention has been directed towards the original bulk material, assuming that retains its structural integrity after exfoliation. However, owing to the weak vdW layer interaction, the tear force applied to exfoliate can produce both a set of exfoliated layers attached to the tape and a few-layer assembly, decoupled from the underlying bulk. This situation is schematically depicted in Fig.4.13. Given the stochastic nature of exfoliation, the resulting assembly have a variable thickness and, therefore, a variable number of QWS as well.

This is precisely, what we have observed in Fig.4.10. Sometimes the exfoliation process leaves the bulk "perfect", with no traces of QWS beneath the parabola (see Fig.4.10a). At other times, we find that the exfoliation yields a variable set of QWS (see Fig.4.10b-f) whose origin is the result of an abrupt reduction of the dimensionality perpendicular to the surface. For instance, in a few-layer MoS_2 assembly, where electrons experience quantum confinement effects.

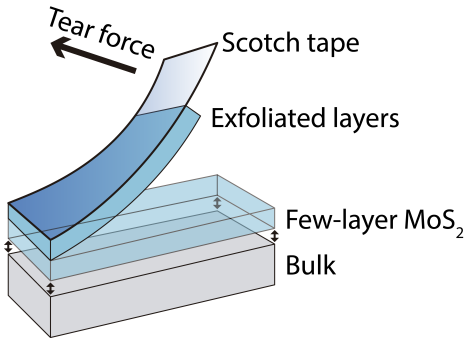

Figure 4.13: Schematic representation of the exfoliation in a vdW material. During the exfoliation process, multiple layers adhere to the tape. However, owing to the weak bonding between the vdW layers, the applied tearing force may result in the detachment of a few-layer assembly from the bulk material.

4.4 . Conclusions

In this chapter, we have centred our attention on the electronic structure of 2H MoS_2. When fresh surfaces of undoped MoS_2 are exposed in a clean UHV environment, the alignment of the VBM is more akin to that of an intrinsic semiconductor. It is important to note that the sample preparation method, mechanical exfoliation, inherently introduces some sulfur vacancies. Thus, our finding contrasts with the n-type conductivity often reported in the literature and is consistent with recent research that challenges sulfur vacancies as the primary cause of the observed n-type conductivity.

After analysing the VB and the CLs of the Nb-doped MoS_2 sample we have concluded that, for the explored doping level, the high quality of the spectra implies an integration of Nb within the crystal that does not affect the VB shape. Doping yields a p-type rigid shift in the range of 0.5-0.63 eV. Notably, no additional features emerged within the VB or peaks within the CLs that could be attributed to the presence of Nb.

Employing ARPES, we have resolved ADBs beneath the parabolic dispersion at $\overline{\Gamma}$ in various MoS_2 samples. These ADBs exhibited a consistent trend: a decrease in the energy difference for every case and a decrease in the $n = 1$ binding energy as the number of ADBs increased. Moreover, for the $n_{max} = 2$ and 7 cases, we have revealed that the ADBs' binding energy remained constant while changing the photon energy. This implies that the ADBs do not disperse in k_z, while the bulk band indeed exhibited k_z dispersion. These observations align with the expected behaviour of confined states, leading us to conclude that the ADBs are QWS.

We found that the energy spacing of the QWS for each n_{max} is roughly con-

stant, indicating that the potential well cannot be described by the usual infinite square well model but can fit a parabolic well model. The observed QWS occur due to a dimensionality reduction. We propose that the mechanical exfoliation yields a few-layer assembly decoupled from the bulk crystal, originating the confinement. This is very likely given the weakness of the vdW forces that bind the MoS_2 layers together. The stochastic nature of the exfoliation process results in a few-layer assembly of varying thickness, explaining the diversity in the number of QWS observed, and in some cases, the absence of QWS.

The experimental identification of these QWS reveals unreported phenomena within MoS_2, to our best knowledge. It is unusual to observe quantum behaviours in bulk-like samples. This indicates the ease with which quantum behaviours can emerge in TMDs. It also highlights the potential for tuning energy levels near Γ that MoS_2 offers.

5 - Boosting MoS_2 hydrogen adsorption

High-efficiency devices for renewable and sustainable energy conversion are essential for reducing the dependence on conventional fossil fuels and tackling global resource and environmental challenges [206, 207]. Catalysis plays an important role in improving the efficiency of such devices, accelerating the electrochemical processes and lowering the energy input required to carry out the reaction.

State-of-the-art catalysts often employ platinum group metals (PGM) given their exceptional performance in a wide range of applications. However, there is fervent interest in substituting PGM as catalysts because of the convergence of economic, environmental, and technological reasons [208, 209]. Efforts have been made to align catalysis with sustainability objectives, advocating for materials that are both efficient and responsible. In Chap.1 we have presented some of the novel materials that are being explored as PGM substitutes. In this context, we introduce several material groups with well-established research, each showcasing distinctive properties that render them promising for a range of catalytic applications:

1) Metal-organic frameworks. Consisting of porous structures composed of metal clusters and organic ligands (linkers). Their architecture enables the precise tuning of the catalytic sites. However, their synthesis can be energy-demanding and incorporate rare or valuable metals [210].

2) Carbon-based catalyst. This category includes graphene, nanotubes or carbon nitrides. These materials exhibit high stability and large surface areas. The synthesis may be energy-consuming; however, in return, carbon can come from sustainable sources such as biomass or waste [211, 212].

3) Perovskite oxides. The perovskite crystalline structure can accommodate approximately 90% of the metals; this diversity allows fine-tuning of catalytic properties and the use of elements that are more readily available than PGM and without energy-intensive synthesis [213].

4) Noble metal alloy nanostructures. This approach seeks to maintain the characteristic performance of PGM by alloying them with abundant elements and using nanostructures that significantly reduce the amount of material required [214].

5) TMDs. These materials offer a compromise between electronic tunability, large surface area, abundance and low production energy. To maintain a low

environmental impact, extraction and manufacturing procedures must be controlled [78].

TMDs have attracted significant attention in the field of heterogeneous catalysis [75, 215]. In particular, MoS_2 is of paramount interest in electrocatalytic water splitting (WS), a method for clean hydrogen production [216]. Hydrogen, a clean fuel and energy carrier, is a key element in an eco-friendly energy landscape. Its correct implementation is crucial for reducing greenhouse gas emissions, conserving natural resources, and mitigating environmental challenges (see Fig.5.1).

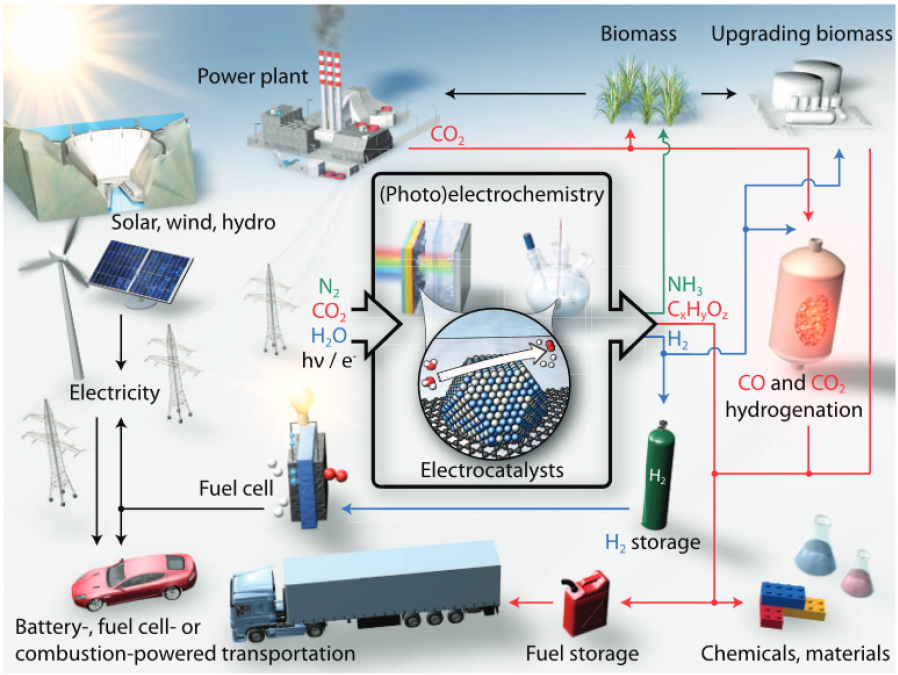

Figure 5.1: Scheme of a sustainable energy production landscape of key resources based on electrocatalysis and photocatalysis. Image adapted from [217].

The WS process involves two half-reactions: the hydrogen evolution reaction (HER) that occurs at the cathode and the oxygen evolution reaction (OER) at the anode [217]. MoS_2 has been explored as a potential substitute for PGM in the HER, driven by various advantageous features. Its catalytic activity can be tuned by manipulating its structure, such as by adjusting the number of layers, and introducing defects making it adaptable to specific requirements. Furthermore, MoS_2 exhibited stability under a broad range of electrochemical conditions, maintaining its catalytic performance even in harsh environments.

Extensive efforts have been made to enhance MoS_2's HER efficiency, particularly through defect engineering. However, relatively less emphasis has been placed on delving into the microscopic mechanisms that govern catalytic activity. For example, a comprehensive correlation between the atomic and electronic structures

in MoS_2 including defects has not yet been established. In this chapter, we aim to elucidate the influence of the sulfur defects on the electronic structure, with a specific focus on the evolution of the Mo d-band and its impact on hydrogen absorption. Defects are induced in the structure by applying simple and reliable in situ methods such as annealing and low-energy ion sputtering (LEIS), offering precise control over surface chemistry. To explore the interaction between defects and hydrogen adsorption, the surfaces with defects were subjected to in situ hydrogenation. The changes in the electronic structure after the introduction of defects and hydrogenation were followed by ARPES, which is highly suitable for this purpose. Simultaneously, the experimental results were compared with DFT calculations to better understand the underlying orbital origin of the observed changes.

5.1 . Hydrogen evolution reaction

As mentioned previously, MoS_2 has been proven to be a well-suited material for hydrogen production through the WS process. The two half-reactions encompass electrocatalytic WS, HER and OER. In the following, we concentrate solely on the HER. Further details regarding the OER and its interaction with MoS_2 can be found elsewhere [217–219].

The HER is conceived as a multistep reaction involving the transfer of two electrons via a catalytic intermediate (H^*). The reaction follows the Volmer-Heyrovsky and/or the Volmer-Tafel mechanism [220, 221]. Fig.5.2a-b shows a schematic representation of the HER in both acidic and neutral/alkaline solutions, respectively. The first step, known as the Volmer step, involves the absorption of a proton (H^+) at the electrode interface.

$$\text{Volmer (acidic): } H^+ + e^- + {}^* \longrightarrow H^*$$

$$\text{Volmer (alkaline): } H_2O + e^- + {}^* \longrightarrow H^* + OH^-$$

where * denotes a site on the electrode surface where H^+ ions can be subsequently bound to form an adsorbed hydrogen intermediate, H^*. In the alkaline solution, previous H-O breaking is required[1]. At this point, the reaction can continue following the Heyrovsky mechanism or the Tafel mechanism. In both cases, further

[1]Breaking the H-O bond requires 286 kJ/mol, 237 kJ/mol due to the standard Gibbs free energy of formation of water and 49 KJ/mol due to the change in entropy [212].

charge transfer occurs to form H_2. The characteristics of the Heyrovsky step depend on whether the solution is acidic or alkaline, while the Tafel is the same for the solution.

$$\text{Heyrovsky (acidic): } H^* + H^+ + e^- \longrightarrow H_2 + {}^*$$

$$\text{Heyrovsky (alkaline): } H^* + H_2O + e^- \longrightarrow H_2 + {}^* + OH^-$$

$$\text{Tafel (acidic or alkaline): } 2\,H^* \longrightarrow H_2 + 2\,{}^*$$

In the Heyrovsky (acidic) step, the previous H^* couples with another H^+ present in the solution, forming H_2. The Heyrovsky (alkaline) step follows the same pattern; however, additional H-O breaking is required to form H^+. On the other hand, in the Tafel step two adjacent H^* at the electrode surface combine to form H_2.

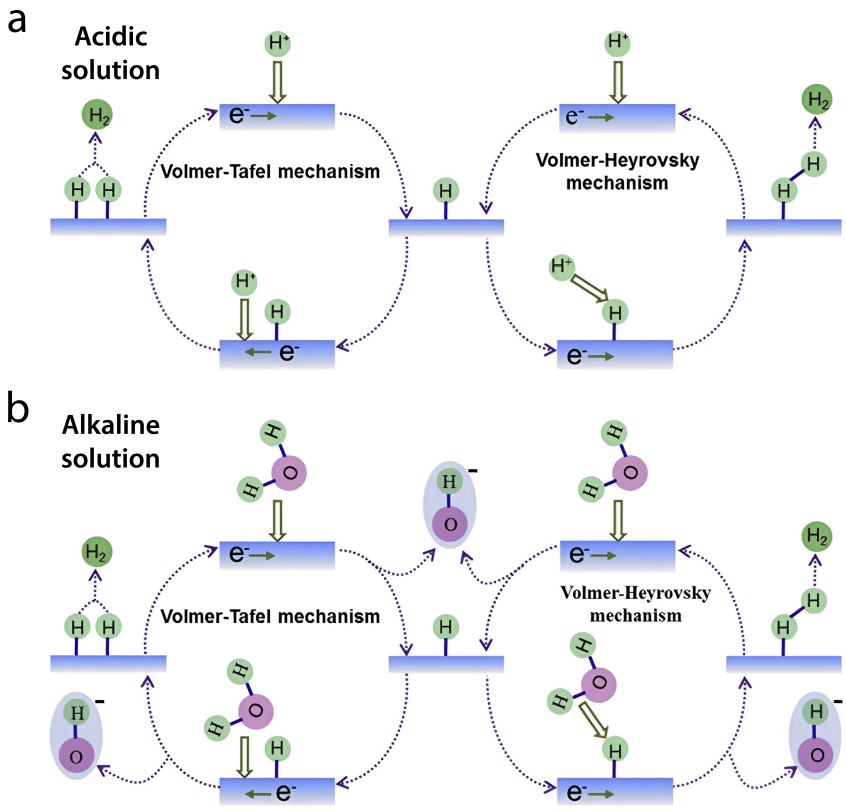

Figure 5.2: Schematic illustration of the HER steps in (a) acidic and (b) alkaline media. Image adapted from [77].

The intermediate H^* plays a crucial role in the HER, as it is involved in all reaction steps. Consequently, the free energy of hydrogen adsorption, ΔG_H, is

often used as a descriptor to evaluate the HER efficiency, following the Sabatier principle [222]. This principle, the golden rule in catalysis, can be summarised as follows: an ideal catalyst should bind the intermediate product neither too weakly, preventing activation of the reactant, nor too strongly, preventing over-binding of the product, which could poison the surface. A value of ΔG_{H} close to zero is ideally sought after for a catalyst, as it indicates a good balance between adsorption and desorption.

Therefore, as MoS_2 has been claimed to be a potentially useful material for the HER, the main open question is: what are the places in the crystal structure of MoS_2 that have a near-zero ΔG_{H} value. From a thermodynamic perspective, the MoS_2 HER is an uphill process ($\Delta G_{\mathsf{H}} > 0$) in the majority of its catalytic centres [223], implying that some energy input is always required to initiate the reaction. However, there are specific catalytic centres for which the energy requirement is very low ($\Delta G_{\mathsf{H}} \approx 0$). For instance, Mo-edges with $0.1 - 0.18$ eV and single sulfur vacancies (Vs) with $-0.08 - 0.08$ eV [181, 223].

5.2 . MoS_2 catalytic centres

5.2.1 . Molybdenum edges

The crystalline edges of MoS_2 are shown in Fig.5.3a-b. The atomic resolution allows the identification of Mo- and S-edges as well as different V_S (see Fig.5.3c-d). Mo-edge has been used as an active centre for hydrodesulfurization in the petroleum industry since the 1990s [224]. Nonetheless, Hinnemann et al. [225] broadened the scope of MoS_2's applicability by identifying its potential as a HER catalyst. They found that the $(10\bar{1}0)$ edge of MoS_2 was suitable for HER catalysis. DFT calculations showed strong initial hydrogen binding to Mo-edge, but as the coverage reached 0.25, the free energy for hydrogen absorption decreased dramatically to 0.1 eV. Jaramillo et al. [226] later confirmed experimentally that the edge is unequivocally an active centre for the HER.

Various strategies have been employed to enhance the edge density, including nanostructuring MoS_2 into shapes such as spiral pyramid shapes [229, 230], introducing nanopores [231], forming nanowires [232], and creating nanospheres [233]. In addition, changing the crystallographic orientation to expose the edges has been explored [234–236]. Nevertheless, these structural modifications can limit charge transport and harm the electrode efficiency. To overcome this limitation, efforts have been made to enhance the intrinsic activity of these centres, that is, tuning the ΔG_{H^*} parameter. Strategies for this enhancement include creating heterostructures by supporting MoS_2 with materials such as graphene [237], Au

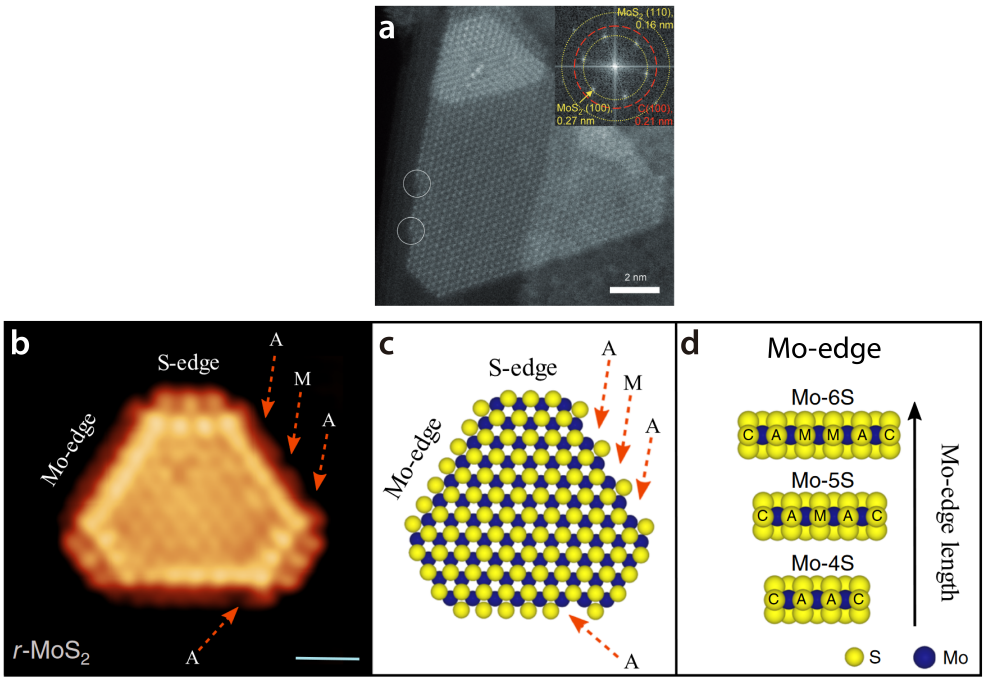

Figure 5.3: (a) High-resolution STEM image of a MoS_2 (0001) flake. Inset: fast Fourier transform (FFT) showing hexagonal spots corresponding to the (100) and (110) lattice planes. Image adapted from [227]. (b) Atomically resolved STM image of a MoS_2 (0001) nanocluster. The Mo-edge and the S-edge are identified. The red arrows indicate V_S positions, 1 V_S at A and 3 V_S at M (c) Ball model of (b), Mo atom (blue) and S atom (yellow). (d) Side view of the ball model highlighting Mo-edges of different lengths at 50 % S coverage. The labels are for atom positions on the edge: (C) for the corner, (A) for adjacent to the corner and (M) for the middle. Image adapted from [228].

[238] and nanoporous Au [239] as well as inducing lattice straining [155, 181]. Furthermore, the modification of the electronic environment through doping has also been tested [76]. We will address this issue below.

5.2.2 . Basal plane

The basal plane of MoS_2 constitutes the major part of its structure. Catalytically, the basal plane is inactive as it lacks catalytic centres ($\Delta G_{H^*} \sim 2$ eV). This inactivity is due to the presence of strong chemical bonds, the lack of exposed active centres, the large bandgap and the absence of states near the Fermi level [240–242]. Although significant attempts have been made to expose the Mo edges, they constitute only a small part of the structure. Therefore, to unleash the MoS_2 catalytic potential, it is highly desirable to realise the HER in the basal plane.

Modulation of MoS_2 into the 1T phase has been extensively explored. DFT calculations predict low values of ΔG_H for both edges and basal plane in the 1T

phase [243]. Additionally, the 1T phase exhibits metallic conductivity approximately five orders of magnitude higher than that of the 2H phase [164], greatly improving electrode kinetics and overall efficiency. Various methods have been examined to achieve the transition from 2H to 1T phase, with alkaline intercalation being a widely used approach [244]. Although the benefits are clear, the current synthesis of the 1T phase is challenging. The lack of precise phase control hinders upscaling, making large-scale production economically expensive and impractical. Additionally, the 1T phase tends to revert to the 2H phase, which limits its practical use [245].

Doping plays a pivotal role in tailoring the MoS_2 electronic properties and surface reactivity, ultimately enhancing its HER performance. The modifications induced by doping in the electronic band structure, along with their impact on catalytic activity, can be explained by the d-band model developed by Hammer and Nørskov [246, 247]. In this model, the electrons in the d-band are simplified into a single state located at the energy centre of the d-band (ϵ_d). The binding strength between the surface and adsorbate is determined by the energy of the antibonding states relative to the Fermi level. As the antibonding states are located above the d states, the energy of ϵ_d relative to the Fermi level serves as a "descriptor" of the binding strength in a catalytic process. The energy position of ϵ_d relative to the Fermi level indicates the bond strength. An ϵ_d close to the Fermi level means a stronger bond, and vice versa [247]. The statement "stronger bond" can be misleading in this context, as it is often also referred to as "binding energy reduction", which requires further clarification. In both cases, this implies a reduction in the free energy of adsorption (ΔG). When adsorption is not favourable ($\Delta G > 0$), a reduction makes the process more feasible. Conversely, when adsorption is already favourable ($\Delta G < 0$), a reduction certainly means a bond strengthening.

In contrast to the aforementioned strategies, doping has notable advantages like simpler synthesis methods for a wide range of available doping agents, including sulfur vacancies, metal atoms (e.g. Nb) [248, 249] and non-metal atoms [250, 251]. Among these dopants, the V_S stand out as catalytic centres for HER (see Fig.5.4a-f) [181, 223]. Controlling the generation of V_S represents a simple, highly efficient and cost-effective means of enhancing HER activity at the basal level. Extensive exploration of the catalytic role of V_S has been conducted, ranging from early investigations [252] to recent computational [253] and experimental studies [181, 223]. When V_S are introduced into the MoS_2 lattice, they give rise to new electronic states in the band gap and within the VB (see Fig.5.4g-h) [99, 173, 175, 179, 254]. Furthermore, a shift in the VB towards the Fermi level, which is proportional to the concentration of V_S, has been reported [99, 175, 179–181]. This VB shift closer to the Fermi level further reduces ΔG_{H}, thereby facilitating hydrogen adsorption and lowering the energy barrier required to break the H-O bond during WS.

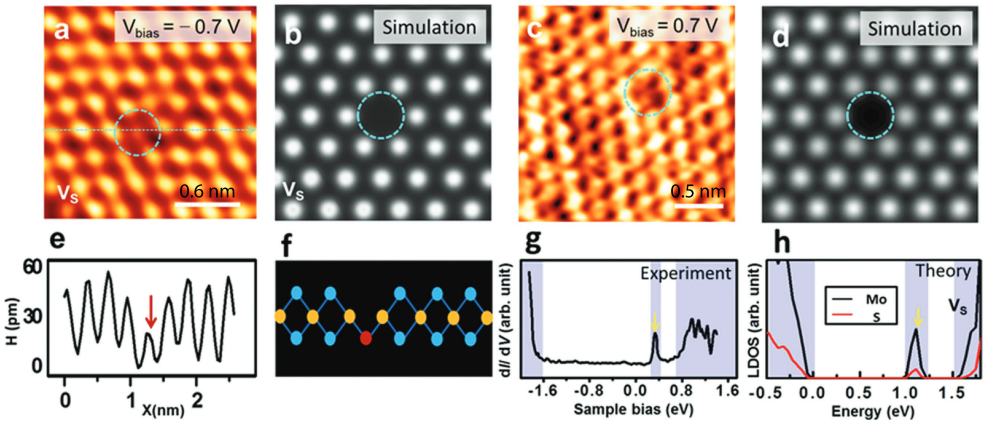

Figure 5.4: (a) and (c) Atomically resolved STM image of a V_S on a monolayer of MoS_2 under -0.7 V and 0.7 V biases, respectively. (b) and (d) STM simulations integrating the wavefunctions with energy below 0 V and 1.5 V, respectively. (e) Height profile along the V_S. A dashed line in (a) indicates the profile path. (f) 2H MoS $_2$ crystalline structure high lightning a V_S at the basal plane. (g-h) dI/dV and calculated local density of states (LDOS) spectra at the single vacancy, respectively. A yellow arrow marks a peak corresponding to the bandgap states induced by the V_S inclusion. Image adapted from [173].

However, there is currently no consensus on the optimal density of V_S for maximising the catalytic activity. Some studies have suggested that near-zero ΔG_{H} is achieved only at low V_S densities [181, 253, 255], indicating that the most effective V_S concentration is $\sim 12\%$. Beyond this point, increasing the density of V_S may diminish the intrinsic activity of the centres, resulting in lower HER efficiency. The exact reasons for this behaviour are not yet fully understood. However, other studies indicate that while low V_S concentrations promote the HER, the highest efficiency is achieved at higher concentrations when the centres form aggregates, such as linear vacancies [256, 257]. Much research is needed to fully comprehend the role of V_S and their interaction with hydrogen intermediates in catalytic processes.

5.3 . Producing defects on the basal plane

5.3.1 . Annealing & low-energy ion sputtering

In order to introduce defects on MoS_2 basal plane we have used thermal annealing and LEIS, as described in Sec.2.3. Thermal annealing is recognised as one of the simplest capable of generating V_S (see Fig.5.5a) [173, 258–261]. The experimental results are in line with theoretical calculations indicating the V_S energy of formation is the lowest among other defects [99, 175]. The rate and threshold

temperature at which S sublimates depend on many parameters [262], but the atmospheric conditions (pressure and gas species) at which the annealing is carried out are the most important determinants. The lower the pressure, the lower the S sublimation rate. A wide range of temperatures at which V_S are observed can be found in the literature. Most studies begin to observe S sublimation above 400 °C at UHV conditions. Thermal decomposition due to S removal was not observed until ~ 1200 °C owing to the strength of the Mo-S bond. However, these studies rarely exceed 900 °C.

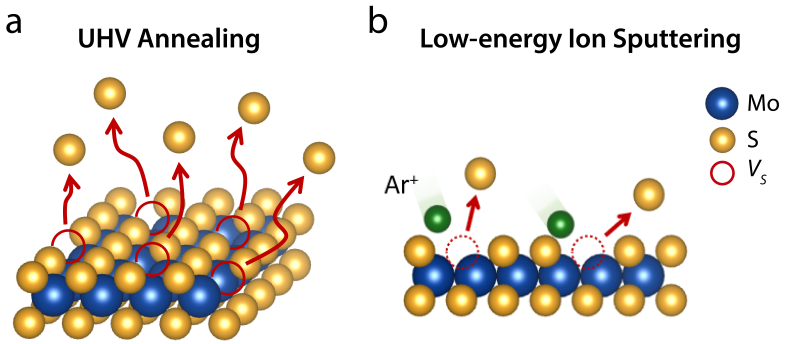

Figure 5.5: Schematic representation of V_S defects generation by (a) annealing and (b) LEIS.

LEIS is an effective approach for tailoring the morphology and properties of materials. In the MoS_2 HER context, ion sputtering has been actively used to augment the V_S density in the basal plane (see Fig.5.5b) [258, 263–268]. These studies showed that Ar^+ ions with low kinetic energy are the most effective for selectively removing sulfur from the basal plane of MoS_2. This selectivity is attributed to the fact that the displacement threshold energy (T_d) of S is about six times lower than that of Mo, using ion with low kinetic energy allows to maintain the Mo stoichiometry while removing S [266].

5.3.2 . Valence Band evolution

ARPES measurements in this section were taken at the URANOS and APE-LE beamlines. The specific experimental details regarding the beamlines can be found in Sec.2.2.1. Prior to measurements, Nb-doped MoS_2 (0001) ($\sim 2 \cdot 10^{17}$ cm^{-3} of Nb concentration) samples were exfoliated under UHV. The in situ annealing, LEIS and hydrogenation procedures were carried out following the methods outlined in Sec.2.3. All the spectra presented were measured using light linearly polarised in the horizontal plane and at a temperature of 110 K. The ARPES spectra were taken at a photon energy $h\nu = 70$ eV and the VBM is used as the energy reference for convenience, as it is customary for semiconductors.

EDC analysis[2] is carried out to get a deeper insight into the effect of annealing and LEIS. Through the following sections several EDCs will be represented, Appx.A.2 contains details about EDC normalisation and how the EDCs are shifted for comparison. To select a k-space region prone to show related changes upon the treatments we would like to recall the detailed analysis of the MoS_2 VB orbital composition that we carried out in Sec.4.2.1.2. If, as expected, the V_S defects are the most likely to form as a result of the treatments and therefore break the Mo-S bond, areas with S p_{xyz} and Mo $d_{z2}/d_{xz}/d_{yz}$ orbital contributions are more likely to display related modifications (see Fig.4.7).

Two regions fulfilling these characteristics are indicated in the ARPES spectra. EDCs centred at $\overline{\Gamma}$ are indicated with a dashed line and integrate a $\Delta k_{\parallel} = 0.1$ Å^{-1} region. The EDCs at $\overline{\Gamma}$ were used for intensity normalisation as described in Appx.A.2. EDCs sets within a 0.4 Å^{-1} region about half way between $\overline{\Gamma}$ and K are indicated with a dashed rectangle. Each EDC within the rectangle corresponds to a $\Delta k_{\parallel} = 0.03$ Å^{-1} region (twelve EDCs in a 0.4Å^{-1} region). Fig.5.6 displays ARPES intensity along the $\overline{\Gamma K}$ direction to follow the annealing and LEIS effects on MoS_2. Panels (a) and (d) correspond to the pristine cases, before each of the treatments. Panels (b-c) correspond to the band structure after annealing at 600 °C and 700 °C, respectively. At a glance, it can be noticed that annealing at these temperatures preserves the overall sample quality. This can be particularly noticed at the $\overline{K}$ point, where the spin splitting remains well resolved. Panels (e-f) show two LEIS treatments for which the ion sputtering time (t) was $t = 20$ s and $t = 150$ s, respectively. Through LEIS, a generalised smearing of the band structure sharpness can be clearly seen in the ARPES intensity, indicative of the disorder introduced by the ion sputtering. The smearing is gradual, increasing from the $\overline{\Gamma}$ point towards states at the $\overline{K}$ point. Additionally, a drastic decrease in the intensity of the band at -2 eV within the dashed rectangle is observed.

Although qualitative changes are evident, further information is obtained through EDC analysis. Fig.5.7a and 5.7d display the EDCs taken at $\overline{\Gamma}$ after annealing and LEIS, respectively. The EDCs of the annealed samples show a very sharp VB edge. The absence of broadening is an additional indication of the crystalline preservation upon the annealing treatments. Remarkably, the EDCs of the LEIS spectra show additional spectral weight near the VBM. In panels (b) and (e) an enlarged region around the VBM highlighting the grey area indicated in panels (a) and (d) is presented. While the pristine curves (black line) show a steep drop, the development of new spectral weight can be observed for each of the treatments. According to the Anderson model [269, 270] a disordered lattice structure, such as that found in amorphous semiconductors, causes the formation of localised electronic states immediately above and just below the extended states of the valence and conduction

[2]See Sec.2.2.3 for more details on EDC analysis.

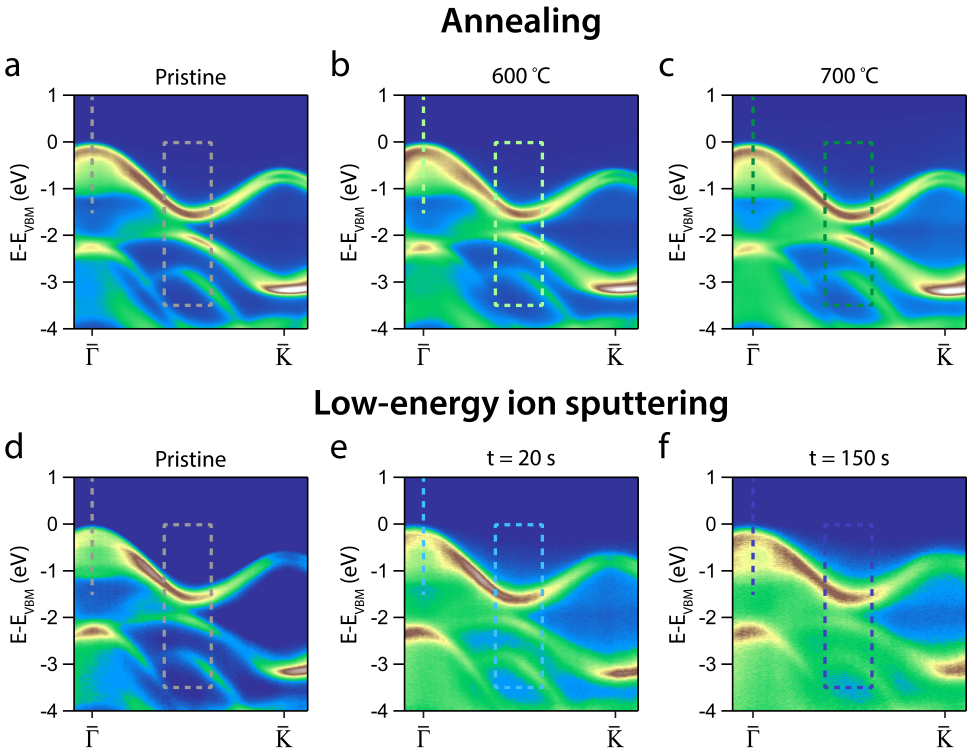

Figure 5.6: ARPES intensity showing the evolution of the MoS_2 dispersion along the $\overline{\Gamma K}$ direction after annealing: (a) pristine, (b) 600 °C, (c) 700 °C and after LEIS: (d) pristine, (e) $t = 20$ s and (f) $t = 150$ s. The dashed lines and rectangles mark the regions from which EDCs will taken. The colour code will be maintained throughout the following sections.

bands (see Fig.5.8a-b). These states, often referred to as band tails, constitute an exponentially decaying density of states that extends into the gap [270, 271]. The exponential shape of the distribution is inherent to the type of disorder (structural or compositional) and constitutes a universal characteristic of disorder. Examples of VB tail observations in PES[3] can be found in Refs. [275–277]. Thus, the observed VB tails, as shown in Fig.5.7b and e, are indicative of the development of new states in the bandgap due to the creation of structural defects upon annealing and LEIS. The VB tail size is considerably larger for LEIS than for annealing, and within each treatment, the VB tail is larger the more intense the treatment. Fig.5.7c and f indicate the VBM shifting upon annealing and LEIS.

Fig.5.9 comprises a set of EDCs taken at the rectangle areas (drawn in Fig.5.6).

[3]The VB tail is more frequently characterized through optical absorption and the so-called Tauc plot. The Urbach energy, which measures the width of the exponential absorption tail, can be estimated from the plot. Its size reflects the extent of the localised states in the bandgap. Refs. [272–274] are examples in which the VB tail of different disordered materials was observed.

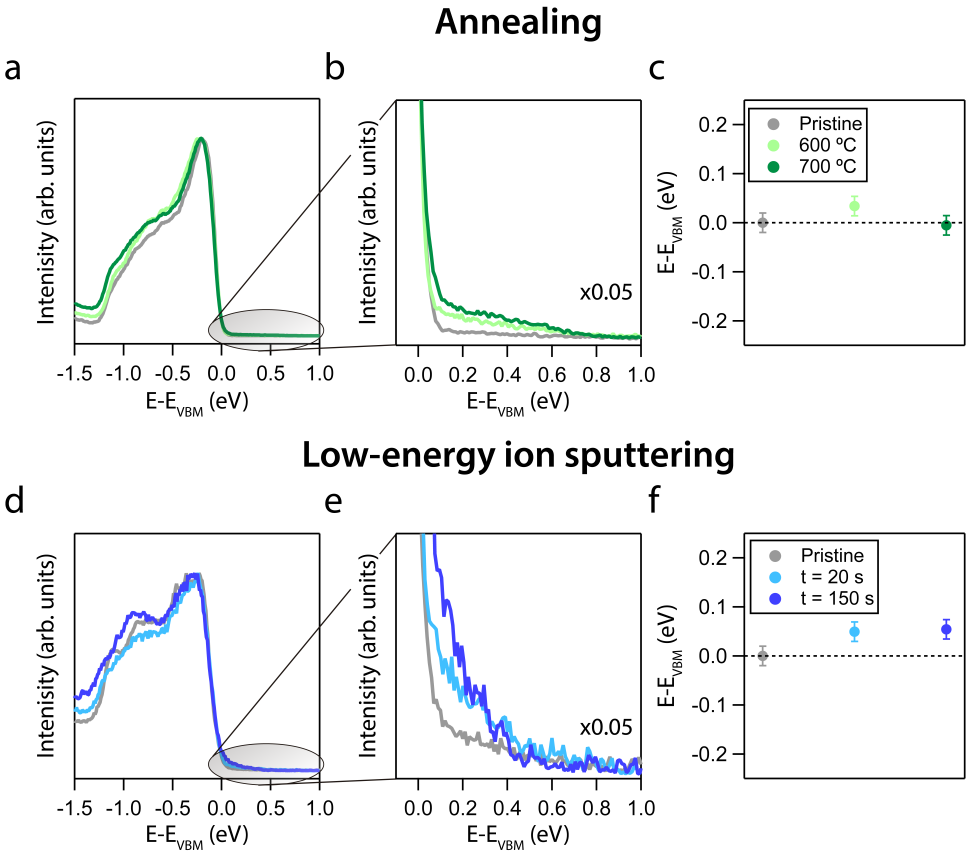

Figure 5.7: EDCs centred at $\overline{\Gamma}$ after (a) annealing and (b) LEIS. (b) and (e) Enlarged region near the VBM of (a) and (d), respectively All the EDCs are multiplied by 0.05. The EDCs in (a-b) and (d-e) were shifted towards their respective pristine VBM for comparison. (c) and (f) Summary of the VBM after annealing and LEIS, respectively.

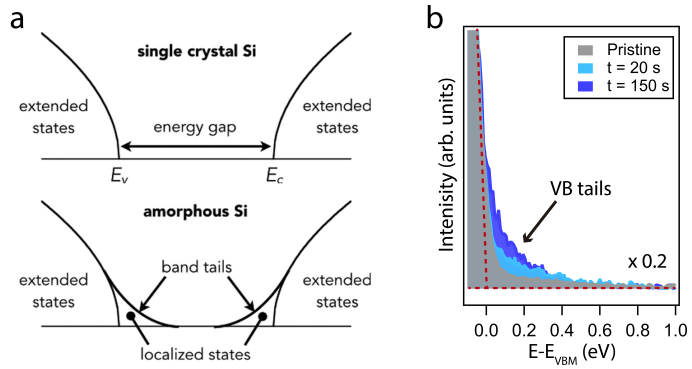

Figure 5.8: (a) Schematic of the DOS in single crystal and amorphous silicon showing the emergence of an exponential tail of localised states immediately above the VB and below the CB. Figure adapted from [278]. (b) EDCs from Fig.5.7e highlight the emergence of VB tails upon LEIS. all the EDCs are multiplied by 0.2.

Panels (a-b) correspond to the annealing at 600 °C and 700 °C, respectively. After annealing, intensity maxima shoulders appear both at lower and higher binding energies. Note that while the EDCs in Fig.5.7a-b showed subtle changes near the VBM, the EDCs at the present region unveil prominent features, indicating that the changes do not affect the entire band structure region equally. Panel (c) presents a comparison between 600 °C and 700 °C, showing that the shoulders are slightly more prominent at 700 °C.

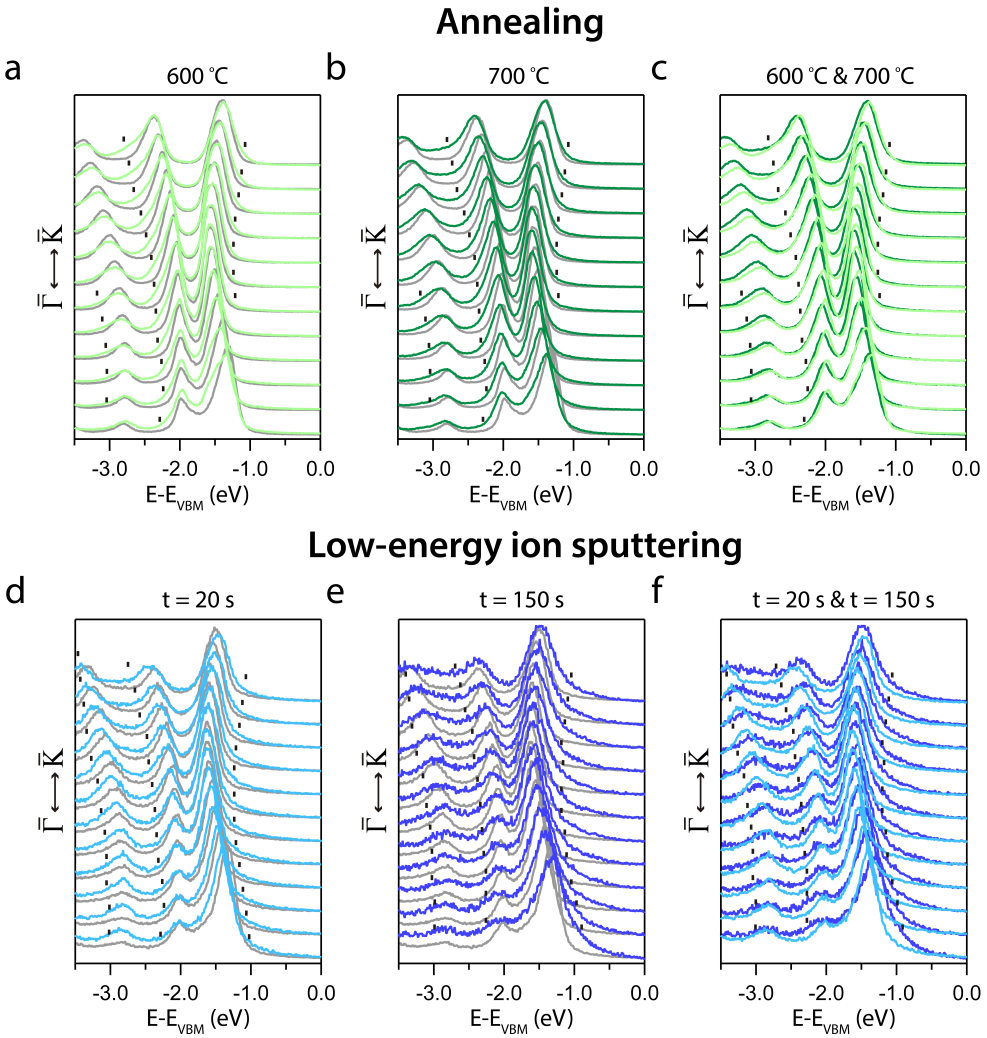

Figure 5.9: EDCs corresponding to the rectangle regions marked in Fig.5.6. (a-b) Annealing at 600 °C and 700 °C, respectively. (c) Comparative of the EDCs between (a-b) annealings. (d-e) LEIS with $t = 20$ s and $t = 150$ s, respectively. (f) Comparative of the EDCs between (d-e) LEIS. The EDCs corresponding to the pristine sample in each case were added for better comparison (black lines). The ticks mark the regions in which shoulders develop.

Panels (d-e) correspond to the LEIS $t = 20$ s and $t = 150$ s, respectively. A similar shoulder development can be observed after LEIS. The shoulders appear in the same regions as in the annealing case. Longer LEIS time generates larger shoulders (see panel (f)), in line with the trend observed for the VB tail (see Fig.5.7d-e). However, some differences between annealing and LEIS are observed. First, the extension of the shoulder development is considerably larger in LEIS. Second, LEIS leads to the disappearance of the band around -2 eV, apparent in Fig.5.6e-f, and now clearly seen. This band's orbital weight at that energy is mostly given by S p orbitals. Therefore, the decrease in its intensity points to a higher removal of S concerning Mo. This effect is also subtly observed after annealing. (see panel (c)).

DFT band structure calculations for a 1 monolayer-MoS_2 incorporating 4% of V_S were performed to gain insight into the experimental changes that we have shown. Dr. Cesar González, a collaborator from the Dto. de Física de Materiales, UCM, Madrid, performed the calculation. Fig.5.10a shows the pristine band structure, as a reference. Fig.5.10b displays the MoS_2 band structure with 4% V_S.

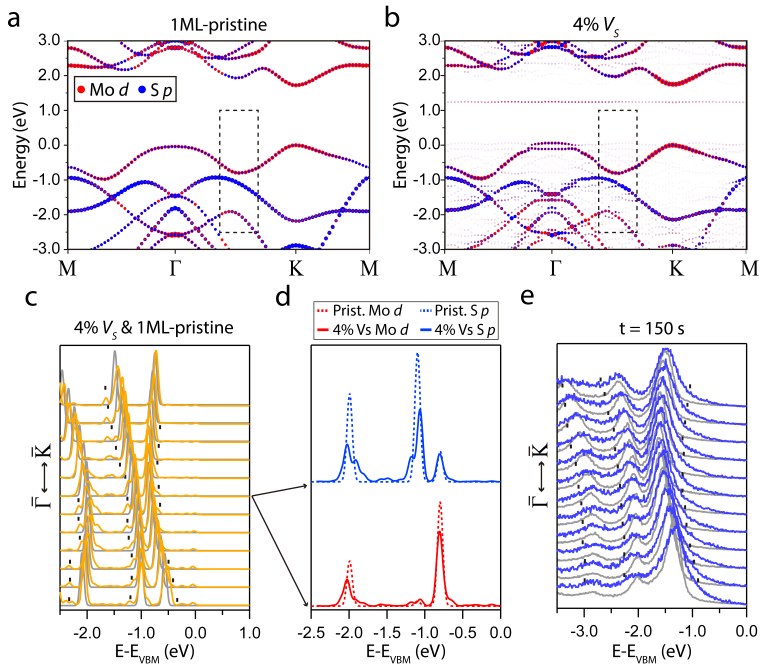

Figure 5.10: DFT orbital-projected electronic band structures calculated for a MoS_2 monolayer along the MΓKM phat for (a) pristine and (b) 4% V_S. Mo d orbitals (red) and S p orbitals (blue). (c) EDCs taken from the dashed rectangle regions in (a-b) without orbital projection. Pristine (black lines) and 4% V_S (orange lines). The central EDC is marked with an arrow and represented with orbital projection in (d) further highlighting the orbital origin of the shoulders at intensity maxima. (e) EDCs taken from the LEIS with $t = 150$s are included as an example and for comparing the shoulder development observed in (c).

Additional features can be observed in the calculation including V_S. A flat, non-dispersive band near the CBM at 1.1 eV energy and new spectral weight distributed throughout the reciprocal space. Since we cannot access unoccupied states with ARPES, in the following, we will only show the part of the calculations corresponding to unoccupied states. To compare the calculations with the experimental results, we extracted a set of EDCs from a region similar to the dashed rectangles of Fig.5.6. Fig.5.10c shows the set of EDCs taken from the 4% V_S band structure. Clearly, the same shoulder development at higher and lower binding energies, present in the experimental band structure after annealing and LEIS is observed in the calculated bands. Panel (d) shows the orbital projection of the shoulders, highlighting the intensity reduction in the S p band by the V_S introduction. Comparing panels (c) and (e) reveals a remarkable agreement between the experimental data and the theoretical calculations, an indication not only of the presence of V_S in the treated samples but also that the concentration should be in the same low range as in the calculations.

5.3.3 . Interaction of hydrogen with surfaces containing defects

After annealing the samples, we conducted in situ exposure to pure H_2 to evaluate their reactivity, as depicted in Figure 5.11. In panel (a), the ARPES intensity along the $\overline{\Gamma K}$ direction is displayed after hydrogenation of the annealed sample at 700 °C. Notably, new spectral weight emerging below 0 eV energy becomes apparent. Panel (b) presents an EDC at the $\overline{\Gamma}$ point, emphasizing the appearance of spectral weight (EDCs of the pristine and 700 °C cases are included for comparison). This new spectral weight forms a well-defined step at the Fermi energy across the entire BZ, as illustrated in panel (c). Furthermore, hydrogenation induces a downward, -0.17 eV, n-type shift of the VB, as seen in panel (d). Simultaneously, the overall band structure exhibits increased sharpness after hydrogenation (compare with Fig.5.6).

Fig.5.12a shows band structure calculations for 1 ML MoS_2 with 2 H atoms adsorbed at the V_S sites (4% V_S). To simulate the impact of H_2 exposure in a surface with V_S various adsorption configurations were examined. Since the evolution of the band structure after annealing indicates that the introduced sulfur defect density is not very high, a 4% of V_S was introduced accordingly. First, in the pristine scenario (with no V_S) we observed that the H_2 molecule prefers to be physisorbed on top sites of Mo atoms (T_{MO}) with a vertical orientation. When V_S defects are introduced, the H_2 molecule tends to occupy the V_S position. However, the outcome depends on the H_2 orientation. Vertically oriented H_2 favours physisorption, adopting an equilibrium position ~ 1.8 Å above the top S layer. Conversely, when the molecule is forced to lie horizontally near a V_S, it undergoes dissociation. The resulting H atoms bind to the uncoordinated Mo

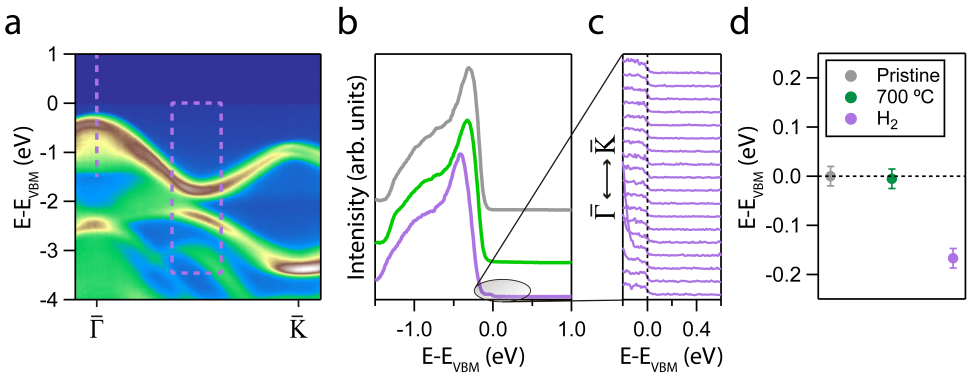

Figure 5.11: Hydrogenation of the sample annealed at 700 °C. The hydrogen dose was 1000 Langmuir (L) at a $1{\cdot}10^{-4}$ mbar pressure. (a) ARPES intensity showing the evolution of the MoS_2 dispersion along the $\overline{\Gamma K}$ direction. (b) EDCs centred at $\overline{\Gamma}$. The pristine and annealed curves were added for better comparison. (c) EDCs showing the formation of a Fermi step after hydrogenation. (d) Summary of the VBM shifting.

atoms (associated with the missing S atom of the V_S), forming a bridge between the Mo atoms. The dissociation scenario is 0.17 eV more favourable than physisorption. Additional configurations were tested by placing one and three hydrogen atoms in the V_S (not shown), the results of which agree less well with those shown for two hydrogen atoms.

In panel (b), we present the EDCs taken at the $\overline{\Gamma}$ point corresponding to different hydrogen pressures during exposure. Relatively high-pressure, $1 \cdot 10^{-4}$ mbar (corresponding to the data in Fig.5.11), and relatively low pressure, $1 \cdot 10^{-6}$ mbar. When the hydrogen pressure is low, it is observed that the spectral weight of the VB tails decreases moderately after hydrogenation; however, despite the large hydrogen dose, the changes are far from those observed at high pressure. This behaviour is in agreement with the calculations; the relatively high pressure helps molecules overcome the energy barrier associated with rotating into a horizontal position within the V_S. In panel (c), we present the EDCs corresponding to the rectangular region marked in panel (a), with the EDCs for the 4% V_S calculation (orange lines) included for comparison. Interestingly, the shoulders at the intensity maxima, attributed to the presence of V_S, are suppressed when hydrogen atoms are adsorbed onto the V_S site. Panel (c) presents a set of EDCs after the high-pressure hydrogenation of the annealed sample at 700 °C. A comparison between panels (c) and (d) reveals identical suppression of the shoulder intensity maxima.

Fig.5.13 shows the in situ hydrogen exposure of the ion-sputtered sample for $t = 150$ s. Panel (a) shows the ARPES intensity along the $\overline{\Gamma K}$ direction after hydrogenating the ion-sputtered sample for a duration of $t = 150$ s. In this case, the response of the band structure differs from that observed after annealing. Hydrogenation amplifies the trend observed in LEIS, wherein the VB tail grows as the

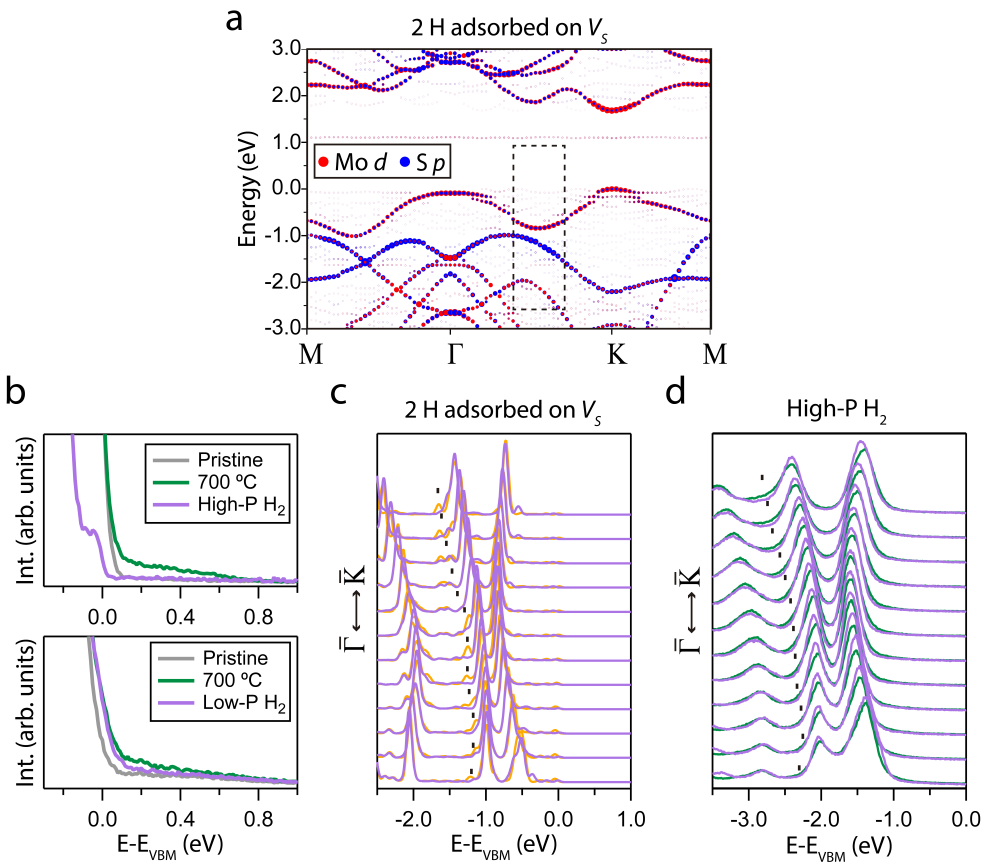

Figure 5.12: (a) DFT orbital-projected electronic band structure calculated for a MoS_2 monolayer along the MΓKM phat for two hydrogen atoms adsorbed on a V_S (4% of V_S). (b) Enlarged region of EDCs centred at $\bar{\Gamma}$ around the VBM showing the high and low-pressure of H_2 dosing. The high pressure (high-P) corresponds to $1 \cdot 10^{-4}$ mbar and a dose of 1000 L. The low pressure (low-P) corresponds to $1 \cdot 10^{-6}$ mbar and a dose of 1000 L. The pristine and 700 °C annealing are included for comparison. (c) EDCs taken from the dashed rectangle regions in (a) without orbital projection. 4% V_S (orange lines) and two hydrogen atoms on a V_S (purple lines). (d) EDCs taken from the high-pressure hydrogenation after 700 °C annealing shown in Fig.5.11, included as an example and for comparing with the shoulder softening observed in (c).

band structure broadens due to lattice disordering (as previously shown in Fig.5.7 and Fig.5.9). Panels (b) and (c) highlight the increased VB tail after hydrogenation. Unlike the annealing case, no Fermi step or n-type shift was observed after hydrogenation, as depicted in Panel (h). Panel (e) presents the EDCs corresponding to the rectangular region marked in panel (a), where no shoulder smoothing or suppression is observed. Furthermore, the EDCs indicate further shoulder broadening and a reduction in the S p_z component after hydrogenation.

The appearance of a Fermi step after hydrogenation, akin to what was observed in the annealed sample, has also been reported in other semiconductors,

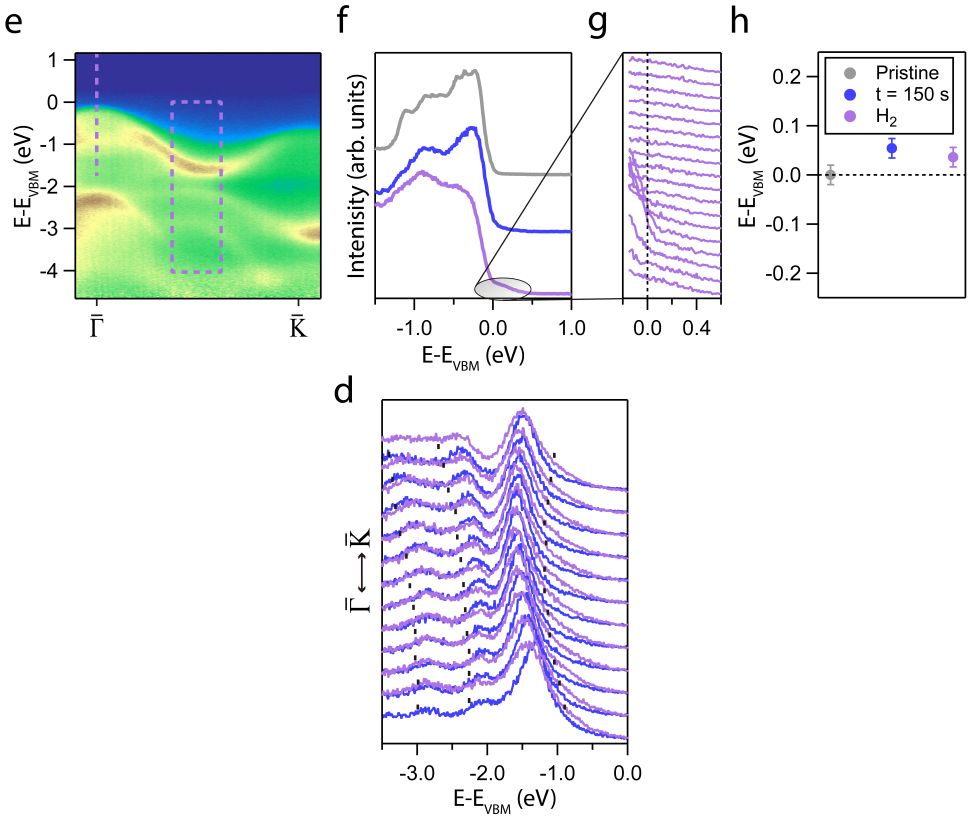

Figure 5.13: Hydrogenation of the ion-sputtered for $t = 150$ s sample. The hydrogen dose was 3340 Langmuir (L) at a $1 \cdot 10^{-6}$ mbar pressure. (a) ARPES intensity showing the evolution of the MoS_2 dispersion along the $\overline{\Gamma K}$ direction. (b) EDCs centred at $\overline{\Gamma}$. The pristine and ion-sputtered curves were added for better comparison. (c) EDCs showing the increase of the VB tail and absence of a Fermi step after hydrogenation. (d) Summary of the VBM shifting.

including Ge (111) [279], Si-terminated n- and p-doped β-SiC(100) [280], $SrTiO_3$ (001) [281], and ZnO ($10\bar{1}0$) [282]. In these examples, a clear transition from semiconducting to metallic surfaces upon hydrogen adsorption can be observed. The hydrogen adsorption in those cases occurs due to dangling bonds passivisation. Similar to these semiconductors, the formation of a metallic Fermi step and an n-type shift of the VB in MoS_2 strongly indicates that a prepared surface with defects can dissociate and adsorb hydrogen. Comparing our experimental results with our calculations and those theoretically predicted in other works [176, 283, 284] allows us to directly prove the dissociative capacity of the V_S defects. Atomic hydrogen adsorption on V_S involves the formation of Mo-H bonds, facilitating charge transfer from the adsorbate to the surface. The excess electrons at the Mo atoms, resulting from V_S formation, are compensated through hydrogen bonding, enhancing overall surface stability.

Furthermore, the improved band structure sharpness observed after hydrogenation (see Fig.5.11a and Fig.5.12c) provides additional experimental evidence of bond formation. This "healing" effect brought about by hydrogen incorporation into V_S is consistent with the "V_S passivation" previously reported for MoS_2 [285, 286]. However, these earlier works did not intentionally generate V_S, and the interaction between hydrogen and V_S was observed to a much lesser extent, with no surface metallisation despite the large hydrogen doses used. Additionally, we have not detected any ambipolar VB or band replicas after hydrogenation, as proposed by Han et al. [285]. Nevertheless, we did observe band replicas and multiple VBM effects resembling ambipolar behaviour. These observations typically occur when the millimeter-sized ARPES beam probes a region of the sample exposing more than one MoS_2 crystallographic grain.

Conversely, no evidence of hydrogen adsorption was observed after the ion-bombarded sample was hydrogenated. It is evident that both treatments increased the defect density. However, with LEIS, a higher defect density was generated, as indicated by the suppression of the S p band (see Fig.5.9d-f). This suggests that either the defect density is exceedingly high, leading to the formation of V_S agglomerates, or bombardment introduces additional defects apart from the V_S, such as sulfur divacancies, interstitials, antisites, etc., or possibly a combination of both factors [258]. Given the low ionic energy used and the similarity in band structure evolution between LEIS and annealing, we favour the former hypothesis. This emphasises the significance of V_S defects over the other types of defects. Our experimental and theoretical results, along with those of Li et al. [181], indicate that for an optimal HER in the MoS_2 basal plane, the V_S concentrations should be kept low. Unrestricted increases in V_S density lead to a reduction in its intrinsic activity and, paradoxically, to an inert basal plane [285].

5.4 . Conclusions

In this chapter, we have investigated the influence of sulfur vacancies on H_2 adsorption on the basal plane of freshly prepared surfaces of Nb-doped MoS_2 bulk crystals. ARPES measurements were employed to study the effect of mild annealing at temperatures of 600 °C, 700 °C as well as Ar^+ LEIS. The results showed distinct changes in the band structure of pristine samples, clearly attributed to the generation of V_S defects at low concentrations of approximately 4%. Selected EDCs that probe the Mo d_{z^2} and S p_z orbitals were presented upon the treatments to highlight the details of the induced changes. Two characteristic features associated with defect creation were identified: the appearance of new states in the form of a VB tail and the emergence of multiple intensity maxima shoulders in S p-like bands. Both originate from the removal of sulfur from the structure, as

evidenced by the suppression of a peak predominantly coming from sulfur orbitals. These fingerprints were strongly supported by DFT calculations conducted on a MoS_2 monolayer with S vacancies, which neatly matched the experimental results.

When the samples with defects were exposed to molecular H_2, the outcome varied depending on whether they had been annealed or ion-sputtered. A low V_S density is achieved for annealing, while a high V_S density is achieved for ion-sputtering. In the case of annealed samples, they were subjected to both high and low H_2 pressure. High H_2 pressure exposure led to the formation of a well-defined Fermi cutoff near the VBM, a downward, 0.17 eV, n-type VB shift and recovery of the crystalline order. The charge transfer effectively reversed the changes induced by the S vacancies. In contrast, exposure to a low H_2 pressure had a similar impact on the band structure, but the observed effects were relatively minor. These results suggest that high pressure accelerates the HER kinetics, shifting the equilibrium towards more adsorbed molecules and explaining the observed differences between high and low H_2 partial pressures, even when substantial doses were used in both cases.

On the other hand, the H_2 dosing of the ion-sputtered samples yielded significantly different results compared to the annealed samples. Spectroscopic signals associated with defect production were considerably stronger after LEIS than after annealing, indicating a more efficient removal of the S. However, no signs of H_2 adsorption were detected; instead, hydrogenation appeared to exacerbate structural damage. This suggests that a large concentration of S vacancies loses their efficiency in H_2 dissociation and adsorption, probably owing to the formation of defect aggregates, such as linear vacancies. This fact highlights the relevance of the V_S electronic environment compared to other types of HER defects.

By engineering a small density of defects in bulk MoS_2 through a straightforward treatment, such as thermal annealing, hydrogen absorption on the basal plane can be effectively improved. The need for a H_2 overpressure to enhance dissociation and adsorption is advantageous in real-world industrial catalytic reactions, where normal conditions (atmospheric pressure and high temperature) differ significantly from UHV experiments. The knowledge developed in our work could contribute to refining strategies for optimising the performance of MoS_2 as an HER catalyst.

6 - Conclusions and perspectives

In this chapter, we consolidate the main results of this thesis and summarise the conclusions of each chapter. Then, we mention the perspectives of the work carried out and the research in progress, outlining future results.

6.1 . Conclusions

Throughout this thesis, we delved into three specific cases that illustrate the exceptional sensitivity of quasi-2D systems to alterations in both their atomic and electronic structures. To achieve this, we took advantage of state-of-the-art synchrotron radiation facilities, enabling the probing of electronic structures through ARPES. Simultaneously, we combined our experimental findings with DFT calculations, seeking to increase the depth of our analysis.

In Chap.3 "A CDW Transition in $LaSb_2$" we have centred our attention in $LaSb_2$, a light rare earth diantimonide with unconventional LMR. Since the LMR in $LaSb_2$ has been linked to the possible presence of CDW, we conducted ARPES measurements at 200 K and 13 K, expecting to find its stabilisation. We observed drastic changes in the band structure and FS of $LaSb_2$ at 13 K, which we attributed to the stabilisation of a CDW phase. These changes include band folding and replicas of the FS along the $\overline{\Gamma Y}$ direction. Both are well-established PES signatures indicating the emergence of a new periodicity. DFT calculations were carried out to deepen our understanding of the experimental results. The calculations revealed that the atoms of the La/Sb bilayer are responsible for the parallel nested FS sheets. Second, the atomic distortion consisting of displacing 0.02 Å all atoms in the unit cell along the *b'* direction accurately reproduced the experimental band folding and spectral weight redistribution. Thus, we propose this PLD as the most likely accompanying the CDW stabilisation.

In Chap.4 "Novel Quantum Well States in MoS_2" we presented in detail the electronic structure of undoped MoS_2. Since the nature of the majority charge carriers in MoS_2 is currently under debate, our results indicate that the Fermi level in clean MoS_2 is close to that of an intrinsic semiconductor.

Thereafter, we showed a series of MoS_2 spectra in which we identified a variable number of additional discrete bands (ADBs) beneath the VBM. We demonstrated that ADBs are QWS by probing their k_z non-dispersive character at different photon energies. Interestingly, we found a constant energy separation between the

QWS that can fit a parabolic well potential instead of the infinite square well often invoked for modelling two-dimensional electron gases. The maximum number of QWS observed varies from one sample to another, and in certain cases, no QWS are observed at all. We attribute this variation to the specific process generating confinement in the samples. The QWS result from a dimensionality reduction caused by the mechanical exfoliation process, during which tearing forces applied for exfoliation leave behind a decoupled few-layer assembly suspended on top of the bulk crystal. It is within this few-layer assembly that the quantum confinement effects emerge.

In Chap.5 "Boosting MoS_2 Hydrogen Adsorption" we have investigated the role of defects introduction into the MoS_2 surface and its impact on hydrogen adsorption. Stabilising a comprehensive correlation between the atomic structure and the evolution of the Mo-d band. To generate sulfur defects we employed in situ thermal annealing and LEIS. Hence, we can ascribe the band structure changes upon treatments to sulfur defect production. We found that both techniques produced similar defects; however, the rate at which LEIS produced defects was considerably higher.

There is an ongoing debate about the ideal single sulfur vacancies (V_S) density for optimizing the HER on the basal plane. Some studies propose an optimal V_S density of around 12%, where a balance between active sites and intrinsic activity is achieved. However, others argue that the V_S density should be maximized, as increasing the number of active sites compensates for the loss of intrinsic activity. To address this question, we prepared surfaces with relatively high and low V_S concentrations by LEIS and annealing, respectively, and dosed them with hydrogen.

We found that the V_S play an active role in H_2 dissociation and adsorption at a low V_S density, whereas at a high V_S density the surface became completely inert. We attributed the inertness at high V_S density to the formation of vacancy clusters or additional defects, whose electrostatic environment does not interact with H_2, resulting in the loss of the intrinsic V_S activity. Conversely, at low V_S density, there is a balance between the number of active centres and their intrinsic activity, allowing us to observe changes upon hydrogenation.

Additionally, we observed that hydrogen partial pressure plays a significant role in favouring the interaction with the defective MoS_2 surface. To investigate this, two surfaces were prepared with a nearly identical low density V_S. Each surface was subsequently exposed to a large H_2 dose at both high and low H_2 pressures. While H_2 adsorption signatures were detected in both cases, we observed drastic changes, such as surface metallisation, with a clear Fermi step that extends throughout the whole reciprocal space, when hydrogenation occurred at high pressure. To our knowledge, this is the first time of such a clear indication of metallisation extending

throughout the entire BZ has been observed in MoS_2.

Given that a substantial hydrogen dose was applied in both scenarios, the observed changes can undoubtedly be attributed to the pressure effect. Furthermore, our DFT simulations indicated that the H_2 molecule must be oriented horizontally within the V_S to dissociate and adsorb, which requires overcoming a certain barrier to achieve that orientation. High pressure can modify several physicochemical aspects related to the chemistry at surfaces, such as the overall adsorption rate, the kinetics of the reactions or the thermodynamic equilibrium of the reactions (Le Chatelier principle). These changes can lead to an apparent reduction in the effective energy barrier, which means that the hydrogenation reaction can occur more easily under high pressure conditions.

6.2 . Perspectives

This PhD study has provided valuable insights, leading to several interesting perspectives for future research.

In the context of the $LaSb_2$ experiments, the natural progression to complement the spectroscopic findings, demonstrating the stabilization of a CDW, involves measuring the crystal structure as a function of temperature. XRD can serve this purpose. However, conducting X-ray diffraction (XRD) experiments on LaSb2 is challenging due to the difficulty in obtaining high-quality crystals. Overcoming these challenges could shed light on the proposed PLD and help determine the critical temperature (T_{CDW}) associated with the CDW transition.

Besides the observed CDW spectroscopic signatures in $LaSb_2$, intriguing changes at 13 K were noted, including spectral weight reduction near the Fermi level across the entire BZ and significant alterations in the binding energy of specific shallow bands. These observations suggest an increase in electron correlation effects. Exploring $LaSb_2$ at even lower temperatures could reveal a new phase, possibly linked to a Mott transition. Investigating $LaSb_2$ at lower temperatures, close to the superconducting transition may unveil insights into the competition or coexistence between different phases, a phenomenon that is still not well understood.

Regarding defect production and hydrogen adsorption in MoS_2, quantifying the introduced defect density after annealing or LEIS is a critical next step. Atomic microscopic techniques, such as STM, offer a reliable means to estimate defect density. STM can also provide clarity on the surface conditions post-LEIS, especially concerning defects other than V_S. Precision in determining the density of defects generated through annealing is essential, particularly for systematic testing of the catalytic activity of defect-containing samples in an electrochemical cell.

Since mild annealing has clear industrial potential, quantifying the defect density can be the first step towards scaling.

From an academic standpoint, while MoS_2 is indeed a sustainable material and ideal for catalytic purposes, extending the knowledge gained regarding defect generation to other materials is vital. Recent calculations indicate that sulfur vacancies in Janus MoSSe can exhibit catalytic activity comparable to strained MoS_2. The know-how of this work can serve as a basis for exploring these new Janus TMDs in the context of the HER and presents an opportunity for future research.

A - Appendix

A.1 . Details of the DFT calculations for $LaSb_2$

In Chap.3 we have presented DFT electronic band calculations [287] that were carried out by combining the Vienna ab-initio simulation package (VASP) [288, 289] and post-processing with the VASPKIT package [290]. The generalized gradient approximation (GGA) in the Perdew-Burke-Ernzerhof (PBE) formulation [291] was used for the exchange–correlation potential. The cut-off energy was set at 500 eV. A Monkhorst-Pack [292, 293] k-meshes with a size of 8 $\times$ 8 $\times$ 2 for the $LaSb_2$ primitive cell and a size of 8 $\times$ 2 $\times$ 2 for the $LaSb_2$ supercell was used for the geometry optimization. The self-consistent field convergence for the total energy and the force variation was set to $10^{\cdot -6}$ eV and 0.001 eV/Å, respectively.

A.2 . EDCs normalisation and EDCs overlapping representation

To facilitate the comparison of the spectra obtained from various samples or samples subjected to different treatments (such as annealing, LEIS, or hydrogenation), it is essential to normalise them. In Fig.A.1a EDCs corresponding to normal emission (EDC at the $\overline{\Gamma}$ point) are presented. Normalisation consists of matching the intensity of Peak 1 (P_1) between the spectra. The choice of P_1 is justified by its predominantly molybdenum composition. When sample-to-sample variations (as seen in Chap.4) or induced structural modifications occur (as seen in Chap.5), mainly the sulfur concentration is altered, while the effects on Mo are minor. Consequently, selecting the upmost band of the band structure, whose orbital weight is mostly attributed to Mo d_{z^2} seems to be a fair choice for normalisation. Within this band, the emission at the $\overline{\Gamma}$ point exhibits high intensity for the employed photon energy ($h\nu = 70$ eV) and linear horizontal polarisation [294]. Therefore, changes in the intensity of the other peaks qualitatively reflect the relative variations in the sulfur concentration.

The reader may wonder why we did not normalise to the photon flux, as is customary in other PES studies. In our experience, while working with MoS_2 crystals and other TMDs, we observed a significant degree of variability in the photoemission intensity. This variability occurs on a sample-to-sample basis and when scanning different regions of a sample. This phenomenon is well-documented in TMDs and is attributed to the influence of small but ever-present concentrations

of defects on the structure of the material [172]. Therefore, it is justifiable to follow the normalisation procedure we described to account for these variations and facilitate meaningful comparisons between spectra.

In addition, as the treatments applied to the samples often cause displacements of the VBM the comparison of shifted EDCs is somewhat complicated. Therefore, to ease their comparison it is customary to overlap the curves. This is achieved by aligning the VBMs of all samples with that of the pristine sample, as it is exemplified in Fig.A.1b. Whenever we display EDCs in this manner, we provide the actual values of the VBMs alongside the figure, as shown in Fig.A.1c. The VBM is calculated following the common practice in PES, this is, using a linear extrapolation of the leading edge to the extended baseline.

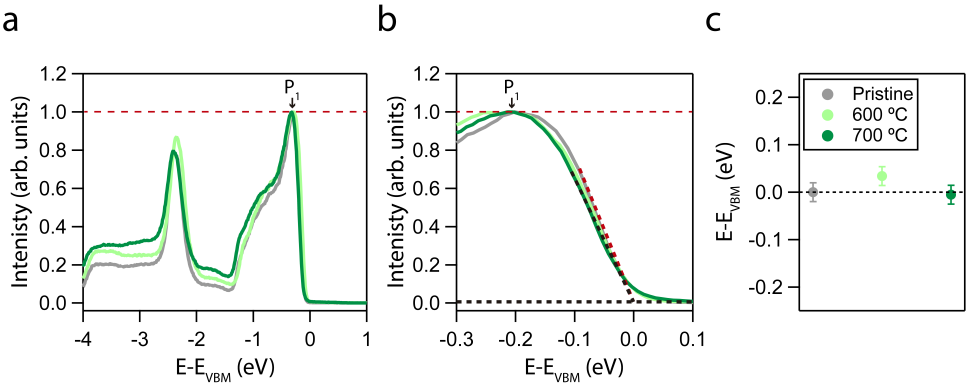

Figure A.1: (a) MoS_2 EDCs obtained at $\overline{\Gamma}$ for a pristine (black line) sample and after annealing at 600 °C (light green line) and 700 °C (green line). The EDCs were normalised by equalling the intensity of Peak 1 (P_1). (b) Enlarged region showing the VBM overlapping of the EDCs shown in (a). The VBM of the 600 °C and 700 °C EDCs were adjusted to match the VBM of the pristine EDC, as indicated by the red lines. The EDCs centered at the $\overline{\Gamma}$ point integrates a $\Delta k_{\parallel} = 0.1$ Å^{-1} region. (c) VBM energy values of the EDCs shown in (a).

A.3 . Details of the DFT calculations for MoS_2

In Chap.4 and Chap.5 we have presented DFT simulations that were performed using the plane-wave Quantum ESPRESSO package [295]. We used the GGA developed by PBE for the exchange and correlation functional [291] as well as the Projector-Augmented Wave (PAW) pseudo-potentials supplied by the code [296]. The cut-off used for the plane waves was 49 Ry. The calculations converged until the difference in the energy (force) was less than $5 \cdot 10^{-5}$ Ry ($4 \cdot 10^{-4}$ Ry/Bohr radius).

Particularly, in Chap.5, the band structures for three cases were calculated:

pristine, V_S and two H atoms adsorbed on a V_S. The Grimme parameterisation of the vdW forces [297] was employed to accurately account for the interactions between H_2 molecules and the MoS_2 surface. Before simulating the V_S inclusion and hydrogen exposure, the pristine band structure was calculated. The pristine structure consists of an MoS_2 monolayer with a periodicity of 1 x 1. The first BZ k-mesh has a 12 x 12 size. The lattice parameter obtained was 3.167 Å, leading to a band structure with a direct band gap of 1.8 eV at the K point. To simulate the V_S defects, we expanded the periodicity of the pristine structure to a 5 x 5 supercell and removed one atom from the cell, corresponding to a 4% V_S concentration. All calculations, including V_S, were performed using this supercell and a 2×2 k-mesh in the first BZ. The supercell size was sufficiently large to simulate an isolated-like vacancy. To compare the calculations with the experimental results, we unfolded the supercell bands into a 1 x 1 unit cell using the unfold-x code base which is suitable for the QE output [298].

List of abbreviations

ADBs additional discrete bands.

ARPES angle-resolved photoemission spectroscopy.

BZ Brillouin zone.

CDW charge density wave.

CEM constant energy map.

CFT crystal field theory.

CL core-level.

CVT chemical vapor transport.

DFT density functional theory.

dHvA de Haas–van Alphen.

EDC energy distribution curve.

FS Fermi surface.

FWHM full width at half maximum.

HER hydrogen evolution reaction.

LDOS local density of states.

LEED low-energy electron diffraction.

LEIS low-energy ion sputtering.

LMR linear magnetoresistance.

LPE liquid-phase exfoliation.

MDC momentum distribution curve.

n-vdW non van der Waals.

OER oxygen evolution reaction.

PES photoelectron spectroscopy.

PGM platinum group metals.

PLD periodic lattice distortion.

QW quantum well.

QWS quantum well states.

SBZ surface Brillouin zone.

SOC spin-orbit coupling.

STM scanning tunneling microscopy.

TMDs transition metal dichalcogenides.

UHV ultra-high vacuum.

VB valence band.

VBM valence band maximum.

vdW van der Waals.

Vs single sulfur vacancies.

WS water splitting.

XPS X-ray photoemission spectroscopy.

XRD X-ray diffraction.

Bibliography

[1] Lev Davidovich Landau. "On the theory of phase transitions. I." In: *Phys. Z. Sowjet.* 11 (1937), p. 26.

[2] R. Peierls. "Quelques propriétés typiques des corps solides". en. In: *Annales de l'institut Henri Poincaré* 5.3 (1935), pp. 177–222.

[3] B. J. Alder and T. E. Wainwright. "Phase Transition in Elastic Disks". In: *Physical Review* 127.2 (1962), pp. 359–361. DOI: 10.1103/PhysRev.127.359.

[4] C. C. Grimes and G. Adams. "Evidence for a Liquid-to-Crystal Phase Transition in a Classical, Two-Dimensional Sheet of Electrons". In: *Physical Review Letters* 42.12 (1979), pp. 795–798. DOI: 10.1103/PhysRevLett.42.795.

[5] N. D. Mermin. "Crystalline Order in Two Dimensions". In: *Physical Review* 176.1 (1968), pp. 250–254. DOI: 10.1103/PhysRev.176.250.

[6] J. M. Kosterlitz and D. J. Thouless. "Ordering, metastability and phase transitions in two-dimensional systems". en. In: *Journal of Physics C: Solid State Physics* 6.7 (1973), p. 1181. DOI: 10.1088/0022-3719/6/7/010.

[7] Sudip Chakravarty and Chandan Dasgupta. "Absence of crystalline order in two dimensions". In: *Physical Review B* 22.1 (1980), pp. 369–372. DOI: 10.1103/PhysRevB.22.369.

[8] C. R. M. Wronski. "The size dependence of the melting point of small particles of tin". en. In: *British Journal of Applied Physics* 18.12 (1967), p. 1731. DOI: 10.1088/0508-3443/18/12/308.

[9] K. S. Novoselov et al. "Electric Field Effect in Atomically Thin Carbon Films". In: *Science* 306.5696 (2004), pp. 666–669. DOI: 10.1126/science.1102896.

[10] Riikka L. Puurunen. "A Short History of Atomic Layer Deposition: Tuomo Suntola's Atomic Layer Epitaxy". en. In: *Chemical Vapor Deposition* 20.10-11-12 (2014), pp. 332–344. DOI: 10.1002/cvde.201402012.

[11] Bruce A Joyce and Tim B Joyce. "Basic studies of molecular beam epitaxy—past, present and some future directions". In: *Journal of Crystal Growth*. Proceedings of the Symposium - Progress in Crystal Growth 264.4 (2004), pp. 605–619. DOI: 10.1016/j.jcrysgro.2003.12.045.

[12] P. R. Wallace. "The Band Theory of Graphite". en. In: *Physical Review* 71.9 (1947), pp. 622–634. DOI: 10.1103/PhysRev.71.622.

[13] H. P. Boehm et al. "Surface properties of extremelly thin graphite lamellae". en. In: *Elsevier eBooks* (1962). DOI: 10.1016/b978-0-08-009707-7.50013-3.

[14] H. Shioyama. "Cleavage of graphite to graphene". en. In: *Journal of Materials Science Letters* 20.6 (2001), pp. 499–500. DOI: 10.1023/A:1010907928709.

[15] K. S. Novoselov et al. "Two-dimensional atomic crystals". eng. In: *Proceedings of the National Academy of Sciences of the United States of America* 102.30 (2005), pp. 10451–10453. DOI: 10.1073/pnas.0502848102.

[16] A. K. Geim and I. V. Grigorieva. "Van der Waals heterostructures". en. In: *Nature* 499.7459 (2013), pp. 419–425. DOI: 10.1038/nature12385.

[17] Patrick Vogt et al. "Silicene: Compelling Experimental Evidence for Graphenelike Two-Dimensional Silicon". en. In: *Physical Review Letters* 108.15 (2012), p. 155501. DOI: 10.1103/PhysRevLett.108.155501.

[18] M. E. Dávila et al. "Germanene: a novel two-dimensional germanium allotrope akin to graphene and silicene". en. In: *New Journal of Physics* 16.9 (2014), p. 095002. DOI: 10.1088/1367-2630/16/9/095002.

[19] Feng-feng Zhu et al. "Epitaxial growth of two-dimensional stanene". en. In: *Nature Materials* 14.10 (2015), pp. 1020–1025. DOI: 10.1038/nmat4384.

[20] Junji Yuhara et al. "Graphene's Latest Cousin: Plumbene Epitaxial Growth on a "Nano WaterCube"". en. In: *Advanced Materials* 31.27 (2019), p. 1901017. DOI: 10.1002/adma.201901017.

[21] Michał W. Ochapski and Michel P. de Jong. "Progress in epitaxial growth of stanene". en. In: *Open Physics* 20.1 (2022), pp. 208–223. DOI: 10.1515/phys-2022-0021.

[22] Jiayong Zhang et al. "Quantum Anomalous Hall Effect in Graphene based Heterostructure". en. In: *Scientific Reports* 5.1 (2015), p. 10629. DOI: 10.1038/srep10629.

[23] Kirill I. Bolotin et al. "Observation of the fractional quantum Hall effect in graphene". en. In: *Nature* 462.7270 (2009), pp. 196–199. DOI: 10.1038/nature08582.

[24] M. I. Katsnelson, K. S. Novoselov, and A. K. Geim. "Chiral tunnelling and the Klein paradox in graphene". en. In: *Nature Physics* 2.9 (2006), pp. 620–625. DOI: 10.1038/nphys384.

[25] C. Dutreix et al. "Measuring the Berry phase of graphene from wavefront dislocations in Friedel oscillations". en. In: *Nature* 574.7777 (2019), pp. 219–222. DOI: 10.1038/s41586-019-1613-5.

[26] Yong Xu et al. "Large-Gap Quantum Spin Hall Insulators in Tin Films". In: *Physical Review Letters* 111.13 (2013), p. 136804. DOI: 10.1103/PhysRevLett.111.136804.

[27] Xiang-Long Yu, Li Huang, and Jiansheng Wu. "From a normal insulator to a topological insulator in plumbene". In: *Physical Review B* 95.12 (2017), p. 125113. DOI: 10.1103/PhysRevB.95.125113.

[28] Kenji Watanabe, Takashi Taniguchi, and Hisao Kanda. "Direct-bandgap properties and evidence for ultraviolet lasing of hexagonal boron nitride single crystal". en. In: *Nature Materials* 3.6 (2004), pp. 404–409. DOI: 10.1038/nmat1134.

[29] Sergio Pezzini et al. "High-quality electrical transport using scalable CVD graphene". en. In: *2D Materials* 7.4 (2020), p. 041003. DOI: 10.1088/2053-1583/aba645.

[30] Theresia Knobloch et al. "The performance limits of hexagonal boron nitride as an insulator for scaled CMOS devices based on two-dimensional materials". en. In: *Nature Electronics* 4.2 (2021), pp. 98–108. DOI: 10.1038/s41928-020-00529-x.

[31] Seokho Moon et al. "Hexagonal Boron Nitride for Next-Generation Photonics and Electronics". en. In: *Advanced Materials* 35.4 (2023), p. 2204161. DOI: 10.1002/adma.202204161.

[32] R. F. Frindt. "Single Crystals of MoS2 Several Molecular Layers Thick". en. In: *Journal of Applied Physics* 37.4 (1966), pp. 1928–1929. DOI: 10.1063/1.1708627.

[33] Per Joensen, R.F. Frindt, and S.Roy Morrison. "Single-layer MoS2". en. In: *Materials Research Bulletin* 21.4 (1986), pp. 457–461. DOI: 10.1016/0025-5408(86)90011-5.

[34] Wencan Jin et al. "Direct Measurement of the Thickness Dependent Electronic Band Structure of MoS2 Using Angle-Resolved Photoemission Spectroscopy". In: *Physical Review Letters* 111.10 (2013), p. 106801. DOI: 10.1103/PhysRevLett.111.106801.

[35] Andrea Splendiani et al. "Emerging Photoluminescence in Monolayer MoS2". In: *Nano Letters* 10.4 (2010), pp. 1271–1275. DOI: 10.1021/nl903868w.

[36] Bei Zhao et al. "2D Metallic Transition-Metal Dichalcogenides: Structures, Synthesis, Properties, and Applications". en. In: *Advanced Functional Materials* 31.48 (2021), p. 2105132. DOI: 10.1002/adfm.202105132.

[37] Chao-Xing Liu. "Unconventional Superconductivity in Bilayer Transition Metal Dichalcogenides". In: *Physical Review Letters* 118.8 (2017), p. 087001. DOI: 10.1103/PhysRevLett.118.087001.

[38] Ziqiang Xu et al. "Topical review: recent progress of charge density waves in 2D transition metal dichalcogenide-based heterojunctions and their applications". en. In: *Nanotechnology* 32.49 (2021), p. 492001. DOI: 10.1088/1361-6528/ac21ed.

[39] Y. D. Wang et al. "Band insulator to Mott insulator transition in 1T-TaS2". en. In: *Nature Communications* 11.1 (2020), p. 4215. DOI: 10.1038/s41467-020-18040-4.

[40] Rong Rong et al. "The Interaction of 2D Materials With Circularly Polarized Light". en. In: *Advanced Science* 10.10 (2023), p. 2206191. DOI: 10.1002/advs.202206191.

[41] Xiaodong Xu et al. "Spin and pseudospins in layered transition metal dichalcogenides". en. In: *Nature Physics* 10.5 (2014), pp. 343–350. DOI: 10.1038/nphys2942.

[42] Nicolas Mounet et al. "Two-dimensional materials from high-throughput computational exfoliation of experimentally known compounds". en. In: *Nature Nanotechnology* 13.3 (2018), pp. 246–252. DOI: 10.1038/s41565-017-0035-5.

[43] Gowoon Cheon et al. "Data Mining for New Two- and One-Dimensional Weakly Bonded Solids and Lattice-Commensurate Heterostructures". en. In: *Nano Letters* 17.3 (2017), pp. 1915–1923. DOI: 10.1021/acs.nanolett.6b05229.

[44] Riccardo Frisenda et al. "Naturally occurring van der Waals materials". en. In: *npj 2D Materials and Applications* 4.1 (2020), pp. 1–13. DOI: 10.1038/s41699-020-00172-2.

[45] Andrea Damascelli, Zahid Hussain, and Zhi-Xun Shen. "Angle-resolved photoemission studies of the cuprate superconductors". en. In: *Reviews of Modern Physics* 75.2 (2003), pp. 473–541. DOI: 10.1103/RevModPhys.75.473.

[46] Sikandar Aftab et al. "Transition metal dichalcogenides solar cells and integration with perovskites". In: *Nano Energy* 108 (2023), p. 108249. DOI: 10.1016/j.nanoen.2023.108249.

[47] S. Guo et al. "Dimensional crossover in the electrical and magnetic properties of the layered LaSb 2 superconductor under pressure: The role of phase fluctuations". en. In: *Physical Review B* 83.17 (2011), p. 174520. DOI: 10.1103/PhysRevB.83.174520.

[48] I. Palacio et al. "Fermi surface of LaSb2 and direct observation of a CDW transition". en. In: *Applied Surface Science* 610 (2023), p. 155477. DOI: 10.1016/j.apsusc.2022.155477.

[49] Aravind Puthirath Balan et al. "Non-van der Waals quasi-2D materials; recent advances in synthesis, emergent properties and applications". In: *Materials Today* 58 (2022), pp. 164–200. DOI: 10.1016/j.mattod.2022.07.007.

[50] Iosif Tantis et al. "Non-van der Waals 2D Materials for Electrochemical Energy Storage". en. In: *Advanced Functional Materials* 33.19 (2023), p. 2209360. DOI: 10.1002/adfm.202209360.

[51] Tom Barnowsky, Arkady V. Krasheninnikov, and Rico Friedrich. "A New Group of 2D Non-van der Waals Materials with Ultra Low Exfoliation Energies". en. In: *Advanced Electronic Materials* 9.4 (2023), p. 2201112. DOI: 10.1002/aelm.202201112.

[52] Aleksandr Rodin et al. "Collective excitations in 2D materials". en. In: *Nature Reviews Physics* 2.10 (2020), pp. 524–537. DOI: 10.1038/s42254-020-0214-4.

[53] Yoshinori Tokura. "Quantum materials at the crossroads of strong correlation and topology". en. In: *Nature Materials* 21.9 (2022), pp. 971–973. DOI: 10.1038/s41563-022-01339-6.

[54] Di Xiao, Wang Yao, and Qian Niu. "Valley-Contrasting Physics in Graphene: Magnetic Moment and Topological Transport". In: *Physical Review Letters* 99.23 (2007), p. 236809. DOI: 10.1103/PhysRevLett.99.236809.

[55] Ziliang Ye, Dezheng Sun, and Tony F. Heinz. "Optical manipulation of valley pseudospin". en. In: *Nature Physics* 13.1 (2017), pp. 26–29. DOI: 10.1038/nphys3891.

[56] Xiao Li, Fan Zhang, and Qian Niu. "Unconventional Quantum Hall Effect and Tunable Spin Hall Effect in Dirac Materials: Application to an Isolated ${\mathrm{MoS}}_{2}$ Trilayer". In: *Physical Review Letters* 110.6 (2013), p. 066803. DOI: 10.1103/PhysRevLett.110.066803.

[57] Ajit Srivastava et al. "Valley Zeeman effect in elementary optical excitations of monolayer WSe2". en. In: *Nature Physics* 11.2 (2015), pp. 141–147. DOI: 10.1038/nphys3203.

[58] Zhi-Ming Yu et al. "Valley-Layer Coupling: A New Design Principle for Valleytronics". en. In: *Physical Review Letters* 124.3 (2020), p. 037701. DOI: 10.1103/PhysRevLett.124.037701.

[59] J. M. Riley et al. "Direct observation of spin-polarized bulk bands in an inversion-symmetric semiconductor". en. In: *Nature Physics* 10.11 (2014), pp. 835–839. DOI: 10.1038/nphys3105.

[60] Yilin Zhang et al. "The origin of the band-splitting and the spin polarization in bulk 2H-WSe2". In: *Applied Physics Letters* 122.14 (2023), p. 142402. DOI: 10.1063/5.0146774.

[61] Chongyun Jiang et al. "Zeeman splitting via spin-valley-layer coupling in bilayer MoTe2". en. In: *Nature Communications* 8.1 (2017), p. 802. DOI: 10.1038/s41467-017-00927-4.

[62] Yuan Cao et al. "Unconventional superconductivity in magic-angle graphene superlattices". eng. In: *Nature* 556.7699 (2018), pp. 43–50. DOI: 10.1038/nature26160.

[63] Beibei Shi et al. "Exotic physical properties of 2D materials modulated by moiré superlattices". en. In: *Materials Advances* 2.17 (2021), pp. 5542–5559. DOI: 10.1039/D1MA00263E.

[64] You Zhou et al. "Bilayer Wigner crystals in a transition metal dichalcogenide heterostructure". en. In: *Nature* 595.7865 (2021), pp. 48–52. DOI: 10.1038/s41586-021-03560-w.

[65] Jeong Min Park et al. "Tunable strongly coupled superconductivity in magic-angle twisted trilayer graphene". en. In: *Nature* 590.7845 (2021), pp. 249–255. DOI: 10.1038/s41586-021-03192-0.

[66] Yiran Zhang et al. "Promotion of superconductivity in magic-angle graphene multilayers". In: *Science* 377.6614 (2022), pp. 1538–1543. DOI: 10.1126/science.abn8585.

[67] Leon Balents et al. "Superconductivity and strong correlations in moiré flat bands". en. In: *Nature Physics* 16.7 (2020), pp. 725–733. DOI: 10.1038/s41567-020-0906-9.

[68] M. Gibertini et al. "Magnetic 2D materials and heterostructures". en. In: *Nature Nanotechnology* 14.5 (2019), pp. 408–419. DOI: 10.1038/s41565-019-0438-6.

[69] Bevin Huang et al. "Layer-dependent ferromagnetism in a van der Waals crystal down to the monolayer limit". en. In: *Nature* 546.7657 (2017), pp. 270–273. DOI: 10.1038/nature22391.

[70] Cheng Gong et al. "Discovery of intrinsic ferromagnetism in two-dimensional van der Waals crystals". en. In: *Nature* 546.7657 (2017), pp. 265–269. DOI: 10.1038/nature22060.

[71] Kenneth S. Burch, David Mandrus, and Je-Geun Park. "Magnetism in two-dimensional van der Waals materials". en. In: *Nature* 563.7729 (2018), pp. 47–52. DOI: 10.1038/s41586-018-0631-z.

[72] Aravind Puthirath Balan et al. "A Non-van der Waals Two-Dimensional Material from Natural Titanium Mineral Ore Ilmenite". en. In: *Chemistry of Materials* 30.17 (2018), pp. 5923–5931. DOI: 10.1021/acs.chemmater.8b01935.

[73] Cui Jin and Liangzhi Kou. "Two-dimensional non-van der Waals magnetic layers: functional materials for potential device applications". en. In: *Journal of Physics D: Applied Physics* 54.41 (2021), p. 413001. DOI: 10.1088/1361-6463/ac08ca.

[74] Aravind Puthirath Balan et al. "Exfoliation of a non-van der Waals material from iron ore hematite". en. In: *Nature Nanotechnology* 13.7 (2018), pp. 602–609. DOI: 10.1038/s41565-018-0134-y.

[75] Ruijie Yang et al. "2D Transition Metal Dichalcogenides for Photocatalysis". en. In: *Angewandte Chemie International Edition* 62.13 (2023), e202218016. DOI: 10.1002/anie.202218016.

[76] Shouheng Li et al. "Atomic structure and HER performance of doped MoS2: A mini-review". In: *Electrochemistry Communications* 155 (2023), p. 107563. DOI: 10.1016/j.elecom.2023.107563.

[77] Prasanta Kumar Sahoo et al. "2D-Layered Non-Precious Electrocatalysts for Hydrogen Evolution Reaction: Fundamentals to Applications". en. In: *Catalysts* 11.6 (2021), p. 689. DOI: 10.3390/catal11060689.

[78] Shrish Nath Upadhyay, Jena Akash Kumar Satrughna, and Srimanta Pakhira. "Recent advancements of two-dimensional transition metal dichalcogenides and their applications in electrocatalysis and energy storage". en. In: *Emergent Materials* 4.4 (2021), pp. 951–970. DOI: 10.1007/s42247-021-00241-2.

[79] Dehui Deng et al. "Catalysis with two-dimensional materials and their heterostructures". en. In: *Nature Nanotechnology* 11.3 (2016), pp. 218–230. DOI: 10.1038/nnano.2015.340.

[80] Lei Tang et al. "Confinement Catalysis with 2D Materials for Energy Conversion". en. In: *Advanced Materials* 31.50 (2019), p. 1901996. DOI: 10.1002/adma.201901996.

[81] Ángel Morales-García, Federico Calle-Vallejo, and Francesc Illas. "MXenes: New Horizons in Catalysis". In: *ACS Catalysis* 10.22 (2020), pp. 13487–13503. DOI: 10.1021/acscatal.0c03106.

[82] H. P. Bonzel and Ch. Kleint. "On the history of photoemission". en. In: *Progress in Surface Science* 49.2 (1995), pp. 107–153. DOI: 10.1016/0079-6816(95)00035-W.

[83] J. G. Jenkin, R. C. G. Leckey, and J. Liesegang. "The development of x-ray photoelectron spectroscopy: 1900–1960". en. In: *Journal of Electron Spectroscopy and Related Phenomena* 12.1 (1977), pp. 1–35. DOI: 10.1016/0368-2048(77)85065-2.

[84] Antonio Tejeda and Daniel Malterre. *A Primer in Photoemission: Concepts and Applications*. en. EDP sciences, 2019.

[85] Kai Siegbahn. *ESCA; atomic, molecular and solid state structure studied by means of electron spectroscopy*. eng. Nova acta Regiae Societatis Scientiarum Upsaliensis. Uppsala: Almqvist & Wiksells, 1967.

[86] C. N. Berglund and W. E. Spicer. "Photoemission Studies of Copper and Silver: Experiment". en. In: *Physical Review* 136.4A (1964), A1044–A1064. DOI: 10.1103/PhysRev.136.A1044.

[87] C. N. Berglund and W. E. Spicer. "Photoemission Studies of Copper and Silver: Theory". en. In: *Physical Review* 136.4A (1964), A1030–A1044. DOI: 10.1103/PhysRev.136.A1030.

[88] W. E. Spicer. "Photoemissive, Photoconductive, and Optical Absorption Studies of Alkali-Antimony Compounds". In: *Physical Review* 112.1 (1958), pp. 114–122. DOI: 10.1103/PhysRev.112.114.

[89] J. B. Pendry. "Theory of photoemission". en. In: *Surface Science* 57.2 (1976), pp. 679–705. DOI: 10.1016/0039-6028(76)90355-1.

[90] J Maurer and U Keller. "Ionization in intense laser fields beyond the electric dipole approximation: concepts, methods, achievements and future directions". en. In: *Journal of Physics B: Atomic, Molecular and Optical Physics* 54.9 (2021), p. 094001. DOI: 10.1088/1361-6455/abf731.

[91] Bertrand Berche, Daniel Malterre, and Ernesto Medina. "Gauge transformations and conserved quantities in classical and quantum mechanics". In: *American Journal of Physics* 84.8 (2016), pp. 616–625. DOI: 10.1119/1.4955153.

[92] M. P. Seah and W. A. Dench. "Quantitative electron spectroscopy of surfaces: A standard data base for electron inelastic mean free paths in solids". en. In: *Surface and Interface Analysis* 1.1 (1979), pp. 2–11. DOI: 10.1002/sia.740010103.

[93] E. O. Kane. "Implications of Crystal Momentum Conservation in Photoelectric Emission for Band-Structure Measurements". In: *Physical Review Letters* 12.4 (1964), pp. 97–98. DOI: 10.1103/PhysRevLett.12.97.

[94] G. D. Mahan. "Theory of Photoemission in Simple Metals". In: *Physical Review B* 2.11 (1970), pp. 4334–4350. DOI: 10.1103/PhysRevB.2.4334.

[95] Stefan Hüfner. "Band Structure and Angular-Resolved Photoelectron Spectra". en. In: *Photoelectron Spectroscopy: Principles and Applications*. Ed. by Stefan Hüfner. Advanced Texts in Physics. Berlin, Heidelberg: Springer, 2003, pp. 411–500. DOI: 10.1007/978-3-662-09280-4_7.

[96] P. Zhang et al. "A precise method for visualizing dispersive features in image plots". en. In: *Review of Scientific Instruments* 82.4 (2011), p. 043712. DOI: 10.1063/1.3585113.

[97] P. C. Canfield and Z. Fisk. "Growth of single crystals from metallic fluxes". In: *Philosophical Magazine B* 65.6 (1992), pp. 1117–1123. DOI: 10.1080/13642819208215073.

[98] Dake Hu et al. "Two-Dimensional Semiconductors Grown by Chemical Vapor Transport". en. In: *Angewandte Chemie International Edition* 56.13 (2017), pp. 3611–3615. DOI: 10.1002/anie.201700439.

[99] Hannu-Pekka Komsa and Arkady V. Krasheninnikov. "Native defects in bulk and monolayer MoS 2 from first principles". en. In: *Physical Review B* 91.12 (2015), p. 125304. DOI: 10.1103/PhysRevB.91.125304.

[100] R. Wang and H. Steinfink. "The crystal chemistry of selected AB2 rare earth compounds with selenium, tellurium, and antimony". In: *Inorganic Chemistry* 6.9 (1967), pp. 1685–1692. DOI: 10.1021/IC50055A017.

[101] S. L. Bud'ko et al. "Anisotropic magnetic properties of light rare-earth diantimonides". en. In: *Physical Review B* 57.21 (1998), pp. 13624–13638. DOI: 10.1103/PhysRevB.57.13624.

[102] D. P. Young et al. "High magnetic field sensor using LaSb2". In: *Applied Physics Letters* 82.21 (2003), pp. 3713–3715. DOI: 10.1063/1.1577390.

[103] F. Hulliger and H.R. Ott. "Superconductivity of lanthanum pnictides". en. In: *Journal of the Less Common Metals* 55.1 (1977), pp. 103–113. DOI: 10.1016/0022-5088(77)90266-1.

[104] A. A. Abrikosov. *Fundamentals of the Theory of Metals*. English. Amsterdam: North Holland, 1988.

[105] H. L. Stormer et al. "Strikingly linear magnetic field dependence of the magnetoresistivity in high quality two-dimensional electron systems". en. In: *Solid State Communications*. A Festschrift Issue of Solid State Communication to Pay Tribute to Professor Ellias Burstein 84.1 (1992), pp. 95–98. DOI: 10.1016/0038-1098(92)90302-P.

[106] Steven H. Simon and Bertrand I. Halperin. "Explanation for the Resistivity Law in Quantum Hall Systems". en. In: *Physical Review Letters* 73.24 (1994), pp. 3278–3281. DOI: 10.1103/PhysRevLett.73.3278.

[107] M. M. Parish and P. B. Littlewood. "Non-saturating magnetoresistance in heavily disordered semiconductors". en. In: *Nature* 426.6963 (2003), pp. 162–165. DOI: 10.1038/nature02073.

[108] R. G. Goodrich et al. "de Haas–van Alphen measurements of the electronic structure of LaSb 2". en. In: *Physical Review B* 69.12 (2004), p. 125114. DOI: 10.1103/PhysRevB.69.125114.

[109] A A Abrikosov. "Quantum linear magnetoresistance; solution of an old mystery". en. In: *Journal of Physics A: Mathematical and General* 36.35 (2003), pp. 9119–9131. DOI: 10.1088/0305-4470/36/35/301.

[110] A. A. Sinchenko et al. "Linear magnetoresistance in the charge density wave state of quasi-two-dimensional rare-earth tritellurides". In: *Physical Review B* 96.24 (2017), p. 245129. DOI: 10.1103/PhysRevB.96.245129.

[111] L. M. Falicov and Henrik Smith. "Linear Magnetoresistance and Anisotropic Quantum Fluctuations". en. In: *Physical Review Letters* 29.2 (1972), pp. 124–127. DOI: 10.1103/PhysRevLett.29.124.

[112] Yejun Feng et al. "Linear magnetoresistance in the low-field limit in density-wave materials". In: *Proceedings of the National Academy of Sciences* 116.23 (2019), pp. 11201–11206. DOI: 10.1073/pnas.1820092116.

[113] K Rossnagel. "On the origin of charge-density waves in select layered transition-metal dichalcogenides". In: *Journal of Physics: Condensed Matter* 23.21 (2011), p. 213001. DOI: 10.1088/0953-8984/23/21/213001.

[114] M. D. Johannes and I. I. Mazin. "Fermi surface nesting and the origin of charge density waves in metals". en. In: *Physical Review B* 77.16 (2008), p. 165135. DOI: 10.1103/PhysRevB.77.165135.

[115] J. C. Petersen et al. "Clocking the Melting Transition of Charge and Lattice Order in 1 T - TaS 2 with Ultrafast Extreme-Ultraviolet Angle-Resolved Photoemission Spectroscopy". en. In: *Physical Review Letters* 107.17 (2011), p. 177402. DOI: 10.1103/PhysRevLett.107.177402.

[116] C Monney et al. "Probing the exciton condensate phase in 1 T -TiSe $_2$ with photoemission". en. In: *New Journal of Physics* 12.12 (2010), p. 125019. DOI: 10.1088/1367-2630/12/12/125019.

[117] Xuetao Zhu et al. "Classification of charge density waves based on their nature". In: *Proceedings of the National Academy of Sciences* 112.8 (2015), pp. 2367–2371. DOI: 10.1073/pnas.1424791112.

[118] Bogdan Guster et al. "First principles analysis of the CDW instability of single-layer 1 T -TiSe $_2$ and its evolution with charge carrier density". In: *2D Materials* 5.2 (2018), p. 025024. DOI: 10.1088/2053-1583/aab568.

[119] V. Brouet et al. "Angle-resolved photoemission study of the evolution of band structure and charge density wave properties in $R{\text{Te}}_{3}$ ($R=\text{Y}$, La, Ce, Sm, Gd, Tb, and Dy)". In: *Physical Review B* 77.23 (2008), p. 235104. DOI: 10.1103/PhysRevB.77.235104.

[120] C. Song et al. "Charge-density-wave orderings in LaAgSb2: An x-ray scattering study". In: *Physical Review B* 68.3 (2003), p. 035113. DOI: 10.1103/PhysRevB.68.035113.

[121] K.D Myers et al. "Systematic study of anisotropic transport and magnetic properties of RAgSb2 (R=Y, La–Nd, Sm, Gd–Tm)". en. In: *Journal of Magnetism and Magnetic Materials* 205.1 (1999), pp. 27–52. DOI: 10.1016/S0304-8853(99)00472-2.

[122] R. F. Luccas et al. "Charge density wave in layered La1-xCexSb2". In: *Physical Review B* 92.23 (2015), p. 235153. DOI: 10.1103/PhysRevB.92.235153.

[123] A. I. Acatrinei et al. "Angle-resolved photoemission study and first-principles calculation of the electronic structure of LaSb2". English. In: *Journal of Physics-Condensed Matter* 15.33 (2003), pp. L511–L517. DOI: 10.1088/0953-8984/15/33/101.

[124] J. A. Galvis et al. "Scanning tunneling microscopy in the superconductor LaSb 2". en. In: *Physical Review B* 87.21 (2013), p. 214504. DOI: 10.1103/PhysRevB.87.214504.

[125] Karl F. F. Fischer, Nikolaj Roth, and Bo B. Iversen. "Transport properties and crystal structure of layered LaSb2". English. In: *Journal of Applied Physics* 125.4 (2019), p. 045110. DOI: 10.1063/1.5081819.

[126] K. D. Myers et al. "de Haas–van Alphen and Shubnikov–de Haas oscillations in R AgSb 2 (R = Y , La-Nd, Sm)". en. In: *Physical Review B* 60.19 (1999), pp. 13371–13379. DOI: 10.1103/PhysRevB.60.13371.

[127] X. Shi et al. "Observation of Dirac-like band dispersion in LaAgSb 2". en. In: *Physical Review B* 93.8 (2016), p. 081105. DOI: 10.1103/PhysRevB.93.081105.

[128] J. Voit et al. "Electronic Structure of Solids with Competing Periodic Potentials". In: *Science* 290.5491 (2000), pp. 501–503. DOI: 10.1126/science.290.5491.501.

[129] J. Schäfer et al. "High-Temperature Symmetry Breaking in the Electronic Band Structure of the Quasi-One-Dimensional Solid NbSe 3". en. In: *Physical Review Letters* 87.19 (2001), p. 196403. DOI: 10.1103/PhysRevLett.87.196403.

[130] L. Perfetti et al. "Spectroscopic Signatures of a Bandwidth-Controlled Mott Transition at the Surface of 1 T - T a S e 2". en. In: *Physical Review Letters* 90.16 (2003), p. 166401. DOI: 10.1103/PhysRevLett.90.166401.

[131] Xuetao Zhu et al. "Misconceptions associated with the origin of charge density waves". In: *Advances in Physics: X* 2.3 (2017), pp. 622–640. DOI: 10.1080/23746149.2017.1343098.

[132] J.A. Wilson, F.J. Di Salvo, and S. Mahajan. "Charge-density waves and superlattices in the metallic layered transition metal dichalcogenides". en. In: *Advances in Physics* 24.2 (1975), pp. 117–201. DOI: 10.1080/00018737500101391.

[133] Michio Naito and Shoji Tanaka. "Galvanomagnetic Effects in the Charge-Density-Wave State of 2H-NbSe2 and 2H-TaSe2". In: *Journal of the Physical Society of Japan* 51.1 (1982), pp. 228–236. DOI: 10.1143/JPSJ.51.228.

[134] T. Jaouen et al. "Phase separation in the vicinity of Fermi surface hot spots". In: *Physical Review B* 100.7 (2019), p. 075152. DOI: 10.1103/PhysRevB.100.075152.

[135] Xiangde Zhu et al. "Superconductivity and Charge Density Wave in ZrTe3-xSex". en. In: *Scientific Reports* 6.1 (2016), p. 26974. DOI: 10.1038/srep26974.

[136] M. Bovet et al. "Pseudogapped Fermi surfaces of 1 T - TaS 2 and 1 T - TaSe 2 : A charge density wave effect". en. In: *Physical Review B* 69.12 (2004), p. 125117. DOI: 10.1103/PhysRevB.69.125117.

[137] Wenzhong Bao et al. "High mobility ambipolar MoS2 field-effect transistors: Substrate and dielectric effects". In: *Applied Physics Letters* 102.4 (2013), p. 042104. DOI: 10.1063/1.4789365.

[138] Yijin Zhang et al. "Ambipolar MoS $_2$ Thin Flake Transistors". en. In: *Nano Letters* 12.3 (2012), pp. 1136–1140. DOI: 10.1021/nl2021575.

[139] Kin Fai Mak et al. "Atomically Thin MoS 2 : A New Direct-Gap Semiconductor". en. In: *Physical Review Letters* 105.13 (2010), p. 136805. DOI: 10.1103/PhysRevLett.105.136805.

[140] J. C. Knight et al. "Photonic band gap guidance in optical fibers". eng. In: *Science (New York, N.Y.)* 282.5393 (1998), pp. 1476–1478. DOI: 10.1126/science.282.5393.1476.

[141] Chia-Hao M. Chuang et al. "Improved performance and stability in quantum dot solar cells through band alignment engineering". eng. In: *Nature Materials* 13.8 (2014), pp. 796–801. DOI: 10.1038/nmat3984.

[142] Nikolaos Balis, Emmanuel Stratakis, and Emmanuel Kymakis. "Graphene and transition metal dichalcogenide nanosheets as charge transport layers for solution processed solar cells". In: *Materials Today* 19.10 (2016), pp. 580–594. DOI: 10.1016/j.mattod.2016.03.018.

[143] Meng-Lin Tsai et al. "Monolayer MoS2 Heterojunction Solar Cells". In: *ACS Nano* 8.8 (2014), pp. 8317–8322. DOI: 10.1021/nn502776h.

[144] Xing Gu et al. "A Solution-Processed Hole Extraction Layer Made from Ultrathin MoS2 Nanosheets for Efficient Organic Solar Cells". In: *Advanced Energy Materials* 3.10 (2013), pp. 1262–1268. DOI: 10.1002/aenm201300549.

[145] M. F. Crommie, C. P. Lutz, and D. M. Eigler. "Confinement of Electrons to Quantum Corrals on a Metal Surface". In: *Science* 262.5131 (1993), pp. 218–220. DOI: 10.1126/science.262.5131.218.

[146] L. Bürgi et al. "Confinement of Surface State Electrons in Fabry-P\'erot Resonators". In: *Physical Review Letters* 81.24 (1998), pp. 5370–5373. DOI: 10.1103/PhysRevLett.81.5370.

[147] T. Hirahara et al. "Quantum well states in ultrathin Bi films: Angle-resolved photoemission spectroscopy and first-principles calculations study". In: *Physical Review B* 75.3 (2007), p. 035422. DOI: 10.1103/PhysRevB.75.035422.

[148] A. Mugarza et al. "Accurate band mapping via photoemission from thin films". In: *Physical Review B* 69.11 (2004), p. 115422. DOI: 10.1103/PhysRevB.69.115422.

[149] P. Segovia, E. G. Michel, and J. E. Ortega. "Quantum Well States and Short Period Oscillations of the Density of States at the Fermi Level in Cu Films Grown on fcc Co(100)". en. In: *Physical Review Letters* 77.16 (1996), pp. 3455–3458. DOI: 10.1103/PhysRevLett.77.3455.

[150] Chaofei Liu et al. "Equally Spaced Quantum States in van der Waals Epitaxy-Grown Nanoislands". In: *Nano Letters* 21.21 (2021), pp. 9285–9292. DOI: 10.1021/acs.nanolett.1c03423.

[151] Jing Zhang et al. "Direct Visualization and Manipulation of Tunable Quantum Well State in Semiconducting Nb2SiTe4". In: *ACS Nano* 15.10 (2021), pp. 15850–15857. DOI: 10.1021/acsnano.1c03666.

[152] Penghong Ci et al. "Quantifying van der Waals Interactions in Layered Transition Metal Dichalcogenides from Pressure-Enhanced Valence Band Splitting". en. In: *Nano Letters* 17.8 (2017), pp. 4982–4988. DOI: 10.1021/acs.nanolett.7b02159.

[153] Chung-Huai Chang et al. "Orbital analysis of electronic structure and phonon dispersion in MoS 2 , MoSe 2 , WS 2 , and WSe 2 monolayers under strain". en. In: *Physical Review B* 88.19 (2013), p. 195420. DOI: 10.1103/PhysRevB.88.195420.

[154] Sohail Ahmad and Sugata Mukherjee. "A Comparative Study of Electronic Properties of Bulk MoS2 and Its Monolayer Using DFT Technique: Application of Mechanical Strain on MoS2 Monolayer". en. In: *Graphene* 03.04 (2014), pp. 52–59. DOI: 10.4236/graphene.2014.34008.

[155] Saikat Bolar et al. "Activation Strategy of MoS2 as HER Electrocatalyst through Doping-Induced Lattice Strain, Band Gap Engineering, and Active Crystal Plane Design". In: *ACS Applied Materials & Interfaces* 13.1 (2021), pp. 765–780. DOI: 10.1021/acsami.0c20500.

[156] Jonghwan Kim et al. "Observation of ultralong valley lifetime in WSe2/MoS2 heterostructures". In: *Science Advances* 3.7 (2017), e1700518. DOI: 10.1126/sciadv.1700518.

[157] Woojoo Lee et al. "Momentum-Resolved Electronic Structures of a Monolayer-MoS2/Multilayer-MoSe2 Heterostructure". In: *The Journal of Physical Chemistry C* 125.30 (2021), pp. 16591–16597. DOI: 10.1021/acs.jpcc.1c04219.

[158] Nadine Leisgang et al. "Giant Stark splitting of an exciton in bilayer MoS2". en. In: *Nature Nanotechnology* 15.11 (2020), pp. 901–907. DOI: 10.1038/s41565-020-0750-1.

[159] Mingu Kang et al. "Universal Mechanism of Band-Gap Engineering in Transition-Metal Dichalcogenides". In: *Nano Letters* 17.3 (2017), pp. 1610–1615. DOI: 10.1021/acs.nanolett.6b04775.

[160] Mamta Devi Sharma et al. "Doping of MoS2 by "Cu" and "V": An Efficient Strategy for the Enhancement of Hydrogen Evolution Activity". In: *Langmuir* 37.16 (2021), pp. 4847–4858. DOI: 10.1021/acs.langmuir.1c00036.

[161] Yi Shi et al. "Energy Level Engineering of MoS $_2$ by Transition-Metal Doping for Accelerating Hydrogen Evolution Reaction". en. In: *Journal of the American Chemical Society* 139.43 (2017), pp. 15479–15485. DOI: 10.1021/jacs.7b08881.

[162] Subramaniam Jayabal et al. "Metallic 1T-MoS2 nanosheets and their composite materials: Preparation, properties and emerging applications". en. In: *Materials Today Energy* 10 (2018), pp. 264–279. DOI: 10.1016/j.mtener.2018.10.009.

[163] Hai He et al. "Structural Properties and Phase Transition of Na Adsorption on Monolayer MoS2". en. In: *Nanoscale Research Letters* 11.1 (2016), p. 330. DOI: 10.1186/s11671-016-1550-2.

[164] Yicen Zhang et al. "Recent progress of electrochemical hydrogen evolution over 1T-MoS2 catalysts". In: *Frontiers in Chemistry* 10 (2022).

[165] Jyah Strachan, Anthony F. Masters, and Thomas Maschmeyer. "3R-MoS2 in Review: History, Status, and Outlook". In: *ACS Applied Energy Materials* 4.8 (2021), pp. 7405–7418. DOI: 10.1021/acsaem.1c00638.

[166] B. Schönfeld, J. J. Huang, and S. C. Moss. "Anisotropic mean-square displacements (MSD) in single-crystals of 2 *H* - and 3 *R* -MoS $_2$". In: *Acta Crystallographica Section B Structural Science* 39.4 (1983), pp. 404–407. DOI: 10.1107/S0108768183002645.

[167] Florence P. Novais Antunes et al. "Van der Waals interactions and the properties of graphite and 2H-, 3R- and 1T-MoS2: A comparative study". en. In: *Computational Materials Science* 152 (2018), pp. 146–150. DOI: 10.1016/j.commatsci.2018.05.045.

[168] Jie Sun et al. "Synthesis Methods of Two-Dimensional MoS2: A Brief Review". en. In: *Crystals* 7.7 (2017), p. 198. DOI: 10.3390/cryst7070198.

[169] B. Radisavljevic et al. "Single-layer MoS2 transistors". en. In: *Nature Nanotechnology* 6.3 (2011), pp. 147–150. DOI: 10.1038/nnano.2010.279.

[170] Hai Li et al. "Optical Identification of Single- and Few-Layer MoS2 Sheets". In: *Small* 8.5 (2012), pp. 682–686. DOI: 10.1002/smll.201101958.

[171] Yi-Hsien Lee et al. "Synthesis of Large-Area MoS2 Atomic Layers with Chemical Vapor Deposition". In: *Advanced Materials* 24.17 (2012), pp. 2320–2325. DOI: 10.1002/adma.201104798.

[172] Rafik Addou et al. "Impurities and Electronic Property Variations of Natural MoS $_2$ Crystal Surfaces". en. In: *ACS Nano* 9.9 (2015), pp. 9124–9133. DOI: 10.1021/acsnano.5b03309.

[173] Mengxi Liu et al. "Temperature-Triggered Sulfur Vacancy Evolution in Monolayer MoS2/Graphene Heterostructures". en. In: *Small* 13.40 (2017), p. 1602967. DOI: 10.1002/smll.201602967.

[174] Stephen McDonnell et al. "Defect-Dominated Doping and Contact Resistance in MoS $_2$". en. In: *ACS Nano* 8.3 (2014), pp. 2880–2888. DOI: 10.1021/nn500044q.

[175] Ji-Young Noh, Hanchul Kim, and Yong-Sung Kim. "Stability and electronic structures of native defects in single-layer MoS 2". en. In: *Physical Review B* 89.20 (2014), p. 205417. DOI: 10.1103/PhysRevB.89.205417.

[176] Sang Wook Han et al. "Hydrogen physisorption based on the dissociative hydrogen chemisorption at the sulphur vacancy of MoS2 surface". en. In: *Scientific Reports* 7.1 (2017), p. 7152. DOI: 10.1038/s41598-017-07178-9.

[177] Youngsin Park et al. "Unveiling the origin of n-type doping of natural MoS2: carbon". en. In: *npj 2D Materials and Applications* 7.1 (2023), pp. 1–7. DOI: 10.1038/s41699-023-00424-x.

[178] M. D. Siao et al. "Two-dimensional electronic transport and surface electron accumulation in MoS2". en. In: *Nature Communications* 9.1 (2018), p. 1442. DOI: 10.1038/s41467-018-03824-6.

[179] Ashim Kumar Saha and Masato Yoshiya. "Native point defects in MoS2 and their influences on optical properties by first principles calculations". en. In: *Physica B: Condensed Matter*. Special issue on Frontiers in Materials Science: Condensed Matters 532 (2018), pp. 184–194. DOI: 10.1016/j.physb.2017.07.026.

[180] Akash Singh and Abhishek Kumar Singh. "Origin of n-type conductivity of monolayer ${\mathrm{MoS}}_{2}$". In: *Physical Review B* 99.12 (2019), p. 121201. DOI: 10.1103/PhysRevB.99.121201.

[181] Hong Li et al. "Activating and optimizing MoS2 basal planes for hydrogen evolution through the formation of strained sulphur vacancies". en. In: *Nature Materials* 15.1 (2016), pp. 48–53. DOI: 10.1038/nmat4465.

[182] Shinichiro Mouri, Yuhei Miyauchi, and Kazunari Matsuda. "Tunable Photoluminescence of Monolayer MoS2 via Chemical Doping". In: *Nano Letters* 13.12 (2013), pp. 5944–5948. DOI: 10.1021/nl403036h.

[183] Steven Chuang et al. "MoS2 P-type transistors and diodes enabled by high work function MoOx contacts". eng. In: *Nano Letters* 14.3 (2014), pp. 1337–1342. DOI: 10.1021/nl4043505.

[184] Y. Kim et al. "Plasma functionalization for cyclic transition between neutral and charged excitons in monolayer MoS2". en. In: *Scientific Reports* 6.1 (2016), p. 21405. DOI: 10.1038/srep21405.

[185] Kapildeb Dolui et al. "Possible doping strategies for MoS 2 monolayers: An *ab initio* study". en. In: *Physical Review B* 88.7 (2013), p. 075420. DOI: 10.1103/PhysRevB.88.075420.

[186] Joonki Suh et al. "Doping against the Native Propensity of MoS2: Degenerate Hole Doping by Cation Substitution". In: *Nano Letters* 14.12 (2014), pp. 6976–6982. DOI: 10.1021/nl503251h.

[187] Masihhur R. Laskar et al. "p-type doping of MoS $_2$ thin films using Nb". en. In: *Applied Physics Letters* 104.9 (2014), p. 092104. DOI: 10.1063/1.4867197.

[188] Mengge Li et al. "P-type Doping in Large-Area Monolayer MoS $_2$ by Chemical Vapor Deposition". en. In: *ACS Applied Materials & Interfaces* 12.5 (2020), pp. 6276–6282. DOI: 10.1021/acsami.9b19864.

[189] Leyi Loh et al. "Substitutional doping in 2D transition metal dichalcogenides". en. In: *Nano Research* 14.6 (2021), pp. 1668–1681. DOI: 10.1007/s12274-020-3013-4.

[190] X. Yu and H. Hantsche. "Some aspects of the charging effect in monochromatized focused XPS". en. In: *Fresenius' Journal of Analytical Chemistry* 346.1 (1993), pp. 233–236. DOI: 10.1007/BF00321421.

[191] Soohyun Cho et al. "Electronic-dimensionality reduction of bulk MoS2 by hydrogen treatment". en. In: *Physical Chemistry Chemical Physics* 20.35 (2018), pp. 23007–23012. DOI: 10.1039/C8CP02365D.

[192] Beom Seo Kim et al. "Determination of the band parameters of bulk 2H-MX2 (M = Mo, W; X = S, Se) by angle-resolved photoemission spectroscopy". en. In: *Scientific Reports* 6.1 (2016), p. 36389. DOI: 10.1038/srep36389.

[193] Z. Y. Zhu, Y. C. Cheng, and U. Schwingenschlögl. "Giant spin-orbit-induced spin splitting in two-dimensional transition-metal dichalcogenide semiconductors". en. In: *Physical Review B* 84.15 (2011), p. 153402. DOI: 10.1103/PhysRevB.84.153402.

[194] L. F. Mattheiss. "Energy Bands for 2 H - Nb Se 2 and 2 H - Mo S 2". en. In: *Physical Review Letters* 30.17 (1973), pp. 784–787. DOI: 10.1103/PhysRevLett.30.784.

[195] Yu Wang et al. "Real-space detection and manipulation of two-dimensional quantum well states in few-layer MoS 2". en. In: *Physical Review B* 105.8 (2022), p. L081404. DOI: 10.1103/PhysRevB.105.L081404.

[196] Xiaofeng Fan, David J. Singh, and Weitao Zheng. "Valence Band Splitting on Multilayer MoS $_2$: Mixing of Spin–Orbit Coupling and Interlayer Coupling". en. In: *The Journal of Physical Chemistry Letters* 7.12 (2016), pp. 2175–2181. DOI: 10.1021/acs.jpclett.6b00693.

[197] A. Kuc, N. Zibouche, and T. Heine. "Influence of quantum confinement on the electronic structure of the transition metal sulfide T S 2". en. In: *Physical Review B* 83.24 (2011), p. 245213. DOI: 10.1103/PhysRevB.83.245213.

[198] Jason K. Ellis, Melissa J. Lucero, and Gustavo E. Scuseria. "The indirect to direct band gap transition in multilayered MoS2 as predicted by screened hybrid density functional theory". en. In: *Applied Physics Letters* 99.26 (2011), p. 261908. DOI: 10.1063/1.3672219.

[199] Tawinan Cheiwchanchamnangij and Walter R. L. Lambrecht. "Quasiparticle band structure calculation of monolayer, bilayer, and bulk MoS 2". en. In: *Physical Review B* 85.20 (2012), p. 205302. DOI: 10.1103/PhysRevB.85.205302.

[200] A. Kumar and P. K. Ahluwalia. "Electronic structure of transition metal dichalcogenides monolayers 1H-MX2 (M = Mo, W; X = S, Se, Te) from ab-initio theory: new direct band gap semiconductors". en. In: *The European Physical Journal B* 85.6 (2012), p. 186. DOI: 10.1140/epjb/e2012-30070-x.

[201] Yi Zhang et al. "Direct observation of the transition from indirect to direct bandgap in atomically thin epitaxial MoSe2". en. In: *Nature Nanotechnology* 9.2 (2014), pp. 111–115. DOI: 10.1038/nnano.2013.277.

[202] Yi Zhang et al. "Electronic Structure, Surface Doping, and Optical Response in Epitaxial WSe2 Thin Films". In: *Nano Letters* 16.4 (2016), pp. 2485–2491. DOI: 10.1021/acs.nanolett.6b00059.

[203] Fabio Bussolotti et al. "Electronic properties of atomically thin MoS $_2$ layers grown by physical vapour deposition: band structure and energy level alignment at layer/substrate interfaces". en. In: *RSC Advances* 8.14 (2018), pp. 7744–7752. DOI: 10.1039/C8RA00635K.

[204] R. C. Miller et al. "Parabolic quantum wells with the G a A s - Al x Ga 1 - x As system". en. In: *Physical Review B* 29.6 (1984), pp. 3740–3743. DOI: 10.1103/PhysRevB.29.3740.

[205] Fang Liu. "Mechanical exfoliation of large area 2D materials from vdW crystals". In: *Progress in Surface Science* 96.2 (2021), p. 100626. DOI: 10.1016/j.progsurf.2021.100626.

[206] Mark K. Debe. "Electrocatalyst approaches and challenges for automotive fuel cells". en. In: *Nature* 486.7401 (2012), pp. 43–51. DOI: 10.1038/nature11115.

[207] Wei Li, Jun Liu, and Dongyuan Zhao. "Mesoporous materials for energy conversion and storage devices". en. In: *Nature Reviews Materials* 1.6 (2016), pp. 1–17. DOI: 10.1038/natrevmats.2016.23.

[208] Ifan Erfyl Lester Stephens, Jan Rossmeisl, and Ib Chorkendorff. "Toward sustainable fuel cells". In: *Science* 354.6318 (2016), pp. 1378–1379. DOI: 10.1126/science.aal3303.

[209] Bonnie J. Glaister and Gavin M. Mudd. "The environmental costs of platinum–PGM mining and sustainability: Is the glass half-full or half-empty?" en. In: *Minerals Engineering* 23.5 (2010), pp. 438–450. DOI: 10.1016/j.mineng.2009.12.007.

[210] Anastasiya Bavykina et al. "Metal–Organic Frameworks in Heterogeneous Catalysis: Recent Progress, New Trends, and Future Perspectives". In: *Chemical Reviews* 120.16 (2020), pp. 8468–8535. DOI: 10.1021/acs.chemrev.9b00685.

[211] Xien Liu and Liming Dai. "Carbon-based metal-free catalysts". en. In: *Nature Reviews Materials* 1.11 (2016), pp. 1–12. DOI: 10.1038/natrevmats.2016.64.

[212] Iqra Sadiq, Syed Asim Ali, and Tokeer Ahmad. "Graphene-Based Derivatives Heterostructured Catalytic Systems for Sustainable Hydrogen Energy via Overall Water Splitting". en. In: *Catalysts* 13.1 (2023), p. 109. DOI: 10.3390/catal13010109.

[213] M. A. Peña and J. L. G. Fierro. "Chemical Structures and Performance of Perovskite Oxides". In: *Chemical Reviews* 101.7 (2001), pp. 1981–2018. DOI: 10.1021/cr980129f.

[214] Tung-Han Yang et al. "Noble-Metal Nanoframes and Their Catalytic Applications". In: *Chemical Reviews* 121.2 (2021), pp. 796–833. DOI: 10.1021/acs.chemrev.0c00940.

[215] Jun Mao et al. "The rise of two-dimensional MoS2 for catalysis". en. In: *Frontiers of Physics* 13.4 (2018), p. 138118. DOI: 10.1007/s11467-018-0812-0.

[216] Niall Farrell. "Policy design for green hydrogen". In: *Renewable and Sustainable Energy Reviews* 178 (2023), p. 113216. DOI: 10.1016/j.rser.2023.113216.

[217] Zhi Wei Seh et al. "Combining theory and experiment in electrocatalysis: Insights into materials design". In: *Science* 355.6321 (2017), eaad4998. DOI: 10.1126/science.aad4998.

[218] Qiuhua Liang, Geert Brocks, and Anja Bieberle-Hütter. "Oxygen evolution reaction (OER) mechanism under alkaline and acidic conditions". en. In: *Journal of Physics: Energy* 3.2 (2021), p. 026001. DOI: 10.1088/2515-7655/abdc85.

[219] Estefania German and Ralph Gebauer. "Why are MoS2 monolayers not a good catalyst for the oxygen evolution reaction?" In: *Applied Surface Science* 528 (2020), p. 146591. DOI: 10.1016/j.apsusc.2020.146591.

[220] N Krstajic et al. "On the kinetics of the hydrogen evolution reaction on nickel in alkaline solution Part I. The mechanism". en. In: *Journal of Electroanalytical Chemistry* (2001).

[221] J. K. Nørskov et al. "Trends in the Exchange Current for Hydrogen Evolution". en. In: *Journal of The Electrochemical Society* 152.3 (2005), J23. DOI: 10.1149/1.1856988.

[222] Zhi-Jian Zhao et al. "Theory-guided design of catalytic materials using scaling relationships and reactivity descriptors". en. In: *Nature Reviews Materials* 4.12 (2019), pp. 792–804. DOI: 10.1038/s41578-019-0152-x.

[223] Guoqing Li et al. "All The Catalytic Active Sites of MoS2 for Hydrogen Evolution". In: *Journal of the American Chemical Society* 138.51 (2016), pp. 16632–16638. DOI: 10.1021/jacs.6b05940.

[224] Henrik Topsøe, Bjerne S. Clausen, and Franklin E. Massoth. "Hydrotreating Catalysis". en. In: *Catalysis: Science and Technology*. Ed. by John R. Anderson and Michel Boudart. Catalysis-Science and Technology. Berlin, Heidelberg: Springer, 1996, pp. 1–269. DOI: 10.1007/978-3-642-61040-0_1.

[225] Berit Hinnemann et al. "Biomimetic Hydrogen Evolution: MoS2 Nanoparticles as Catalyst for Hydrogen Evolution". In: *Journal of the American Chemical Society* 127.15 (2005), pp. 5308–5309. DOI: 10.1021/ja0504690.

[226] Thomas F. Jaramillo et al. "Identification of Active Edge Sites for Electrochemical H $_2$ Evolution from MoS $_2$ Nanocatalysts". en. In: *Science* 317.5834 (2007), pp. 100–102. DOI: 10.1126/science.1141483.

[227] Lars P. Hansen et al. "Atomic-Scale Edge Structures on Industrial-Style MoS2 Nanocatalysts". In: *Angewandte Chemie International Edition* 50.43 (2011), pp. 10153–10156. DOI: 10.1002/anie.201103745.

[228] Norberto Salazar et al. "Site-dependent reactivity of MoS2 nanoparticles in hydrodesulfurization of thiophene". en. In: *Nature Communications* 11.1 (2020), p. 4369. DOI: 10.1038/s41467-020-18183-4.

[229] Qingwei Zhou et al. "Vertically conductive MoS2 pyramids with a high density of active edge sites for efficient hydrogen evolution". en. In: *Journal of Materials Chemistry C* 8.9 (2020), pp. 3017–3022. DOI: 10.1039/C9TC05872A.

[230] Thuc Hue Ly et al. "Vertically Conductive MoS2 Spiral Pyramid". In: *Advanced Materials* 28.35 (2016), pp. 7723–7728. DOI: 10.1002/adma.201602328.

[231] Jakob Kibsgaard et al. "Engineering the surface structure of MoS2 to preferentially expose active edge sites for electrocatalysis". en. In: *Nature Materials* 11.11 (2012), pp. 963–969. DOI: 10.1038/nmat3439.

[232] Zhebo Chen et al. "Core–shell MoO3–MoS2 Nanowires for Hydrogen Evolution: A Functional Design for Electrocatalytic Materials". In: *Nano Letters* 11.10 (2011), pp. 4168–4175. DOI: 10.1021/nl2020476.

[233] Bangjun Guo et al. "Hollow Structured Micro/Nano MoS2 Spheres for High Electrocatalytic Activity Hydrogen Evolution Reaction". In: *ACS Applied Materials & Interfaces* 8.8 (2016), pp. 5517–5525. DOI: 10.1021/acsami.5b10252.

[234] Neha P. Kondekar et al. "In Situ XPS Investigation of Transformations at Crystallographically Oriented MoS_2 Interfaces". en. In: *ACS Applied Materials & Interfaces* 9.37 (2017), pp. 32394–32404. DOI: 10.1021/acsami.7b10230.

[235] Desheng Kong et al. "Synthesis of MoS2 and MoSe2 Films with Vertically Aligned Layers". In: *Nano Letters* 13.3 (2013), pp. 1341–1347. DOI: 10.1021/nl400258t.

[236] Haotian Wang et al. "Electrochemical tuning of vertically aligned MoS2 nanofilms and its application in improving hydrogen evolution reaction". In: *Proceedings of the National Academy of Sciences* 110.49 (2013), pp. 19701–19706. DOI: 10.1073/pnas.1316792110.

[237] Jarin Joyner et al. "Graphene Supported MoS2 Structures with High Defect Density for an Efficient HER Electrocatalysts". In: *ACS Applied Materials & Interfaces* 12.11 (2020), pp. 12629–12638. DOI: 10.1021/acsami.9b17713.

[238] Charlie Tsai, Frank Abild-Pedersen, and Jens K. Nørskov. "Tuning the MoS2 Edge-Site Activity for Hydrogen Evolution via Support Interactions". In: *Nano Letters* 14.3 (2014), pp. 1381–1387. DOI: 10.1021/nl404444k.

[239] Yongwen Tan et al. "Monolayer MoS2 Films Supported by 3D Nanoporous Metals for High-Efficiency Electrocatalytic Hydrogen Production". In: *Advanced Materials* 26.47 (2014), pp. 8023–8028. DOI: 10.1002/adma.201403808.

[240] P. Raybaud et al. "Ab Initio Study of the H2–H2S/MoS2 Gas–Solid Interface: The Nature of the Catalytically Active Sites". en. In: *Journal of Catalysis* 189.1 (2000), pp. 129–146. DOI: 10.1006/jcat.1999.2698.

[241] Line S. Byskov et al. "DFT Calculations of Unpromoted and Promoted MoS2-Based Hydrodesulfurization Catalysts". In: *Journal of Catalysis* 187.1 (1999), pp. 109–122. DOI: 10.1006/jcat.1999.2598.

[242] S. J. Tauster, T. A. Pecoraro, and R. R. Chianelli. "Structure and properties of molybdenum sulfide: Correlation of O2 chemisorption with hydrodesulfurization activity". In: *Journal of Catalysis* 63.2 (1980), pp. 515–519. DOI: 10.1016/0021-9517(80)90109-8.

[243] Qing Tang and De-en Jiang. "Mechanism of Hydrogen Evolution Reaction on 1T-MoS2 from First Principles". In: *ACS Catalysis* 6.8 (2016), pp. 4953–4961. DOI: 10.1021/acscatal.6b01211.

[244] Mark A. Lukowski et al. "Enhanced Hydrogen Evolution Catalysis from Chemically Exfoliated Metallic MoS2 Nanosheets". In: *Journal of the American Chemical Society* 135.28 (2013), pp. 10274–10277. DOI: 10.1021/ja404523s.

[245] Goki Eda et al. "Photoluminescence from Chemically Exfoliated MoS $_2$". en. In: *Nano Letters* 11.12 (2011), pp. 5111–5116. DOI: 10.1021/nl201874w.

[246] B. Hammer and J.K. Nørskov. "Theoretical surface science and catalysis—calculations and concepts". en. In: *Advances in Catalysis*. Vol. 45. Elsevier, 2000, pp. 71–129. DOI: 10.1016/S0360-0564(02)45013-4.

[247] Jens K. Nørskov et al. "Density functional theory in surface chemistry and catalysis". In: *Proceedings of the National Academy of Sciences* 108.3 (2011), pp. 937–943. DOI: 10.1073/pnas.1006652108.

[248] Huashan Li et al. "Atomic Structure and Dynamics of Single Platinum Atom Interactions with Monolayer MoS2". In: *ACS Nano* 11.3 (2017), pp. 3392–3403. DOI: 10.1021/acsnano.7b00796.

[249] Manjeet Chhetri et al. "Effects of p- and n-type Doping in Inorganic Fullerene MoS $_2$ on the Hydrogen Evolution Reaction". en. In: *ChemElectroChem* 3.11 (2016), pp. 1937–1943. DOI: 10.1002/celc.201600291.

[250] Xiaopei Xu et al. "Computational screening of nonmetal dopants to active MoS2 basal-plane for hydrogen evolution reaction via structural descriptor". In: *Journal of Catalysis* 416 (2022), pp. 47–57. DOI: 10.1016/j.jcat.2022.10.011.

[251] Wen Xiao et al. "Dual-Functional N Dopants in Edges and Basal Plane of MoS2 Nanosheets Toward Efficient and Durable Hydrogen Evolution". en. In: *Advanced Energy Materials* 7.7 (2017), p. 1602086. DOI: 10.1002/aenm.201602086.

[252] C. Rong and X. Qin. "Adsorption and Activation of Thiophene on MoS2, Co9S8 and RuS2". en. In: *Studies in Surface Science and Catalysis*. Vol. 75. Elsevier, 1993, pp. 1919–1922. DOI: 10.1016/S0167-2991(08)64190-7.

[253] Xin Wang et al. "Single-Atom Vacancy Defect to Trigger High-Efficiency Hydrogen Evolution of MoS2". In: *Journal of the American Chemical Society* 142.9 (2020), pp. 4298–4308. DOI: 10.1021/jacs.9b12113.

[254] C González, B Biel, and Y J Dappe. "Theoretical characterisation of point defects on a MoS2 monolayer by scanning tunnelling microscopy". en. In: *Nanotechnology* 27.10 (2016), p. 105702. DOI: 10.1088/0957-4484/27/10/105702.

[255] Sang Wook Han et al. "Hydrogen interaction with selectively desulfurized MoS $_2$ surface using Ne $^+$ sputtering". en. In: *Journal of Applied Physics* 125.8 (2019), p. 085102. DOI: 10.1063/1.5079281.

[256] Lei Li et al. "Role of Sulfur Vacancies and Undercoordinated Mo Regions in MoS $_2$ Nanosheets toward the Evolution of Hydrogen". en. In: *ACS Nano* 13.6 (2019), pp. 6824–6834. DOI: 10.1021/acsnano.9b01583.

[257] Meng Tang et al. "Sulfur Line Vacancies in MoS2 for Catalytic Hydrogen Evolution Reaction". en. In: *Crystals* 12.9 (2022), p. 1218. DOI: 10.3390/cryst12091218.

[258] Weigang Lu, Blake Birmingham, and Zhenrong Zhang. "Defect engineering on MoS2 surface with argon ion bombardments and thermal annealing". In: *Applied Surface Science* 532 (2020), p. 147461. DOI: 10.1016/j.apsusc.2020.147461.

[259] Muhammad Hilmi Johari et al. "Effects of post-annealing on MoS $_2$ thin films synthesized by multi-step chemical vapor deposition". en. In: *Nanomaterials and Nanotechnology* 11 (2021), p. 184798042098153. DOI: 10.1177/1847980420981537.

[260] Elmar Mitterreiter et al. "The role of chalcogen vacancies for atomic defect emission in MoS2". en. In: *Nature Communications* 12.1 (2021), p. 3822. DOI: 10.1038/s41467-021-24102-y.

[261] Rupika Tomar et al. "Probing Sulfur Vacancies in CVD-Grown Monolayer MoS2 on SiO2/Si in the Temperature Range 750–900°C". en. In: *Journal of Electronic Materials* 52.8 (2023), pp. 5513–5520. DOI: 10.1007/s11664-023-10463-1.

[262] Peiyu Chen et al. "Thermal Degradation of Monolayer MoS $_2$ on SrTiO $_3$ Supports". en. In: *The Journal of Physical Chemistry C* 123.6 (2019), pp. 3876–3885. DOI: 10.1021/acs.jpcc.8b11298.

[263] Quan Ma et al. "Controlled argon beam-induced desulfurization of monolayer molybdenum disulfide". en. In: *Journal of Physics: Condensed Matter* 25.25 (2013), p. 252201. DOI: 10.1088/0953-8984/25/25/252201.

[264] Antonino Santoni et al. "Electronic structure of Ar+ ion-sputtered thin-film MoS2: A XPS and IPES study". en. In: *Applied Surface Science* 392 (2017), pp. 795–800. DOI: 10.1016/j.apsusc.2016.09.007.

[265] Simone Bertolazzi et al. "Engineering Chemically Active Defects in Monolayer MoS2 Transistors via Ion-Beam Irradiation and Their Healing via Vapor Deposition of Alkanethiols". en. In: *Advanced Materials* 29.18 (2017), p. 1606760. DOI: 10.1002/adma.201606760.

[266] Mahdi Ghorbani-Asl et al. "Two-dimensional MoS2 under ion irradiation: from controlled defect production to electronic structure engineering". en. In: *2D Materials* 4.2 (2017), p. 025078. DOI: 10.1088/2053-1583/aa6b17.

[267] M. A Baker et al. "XPS investigation of preferential sputtering of S from MoS2 and determination of MoSx stoichiometry from Mo and S peak positions". en. In: *Applied Surface Science* 150.1 (1999), pp. 255–262. DOI: 10.1016/S0169-4332(99)00253-6.

[268] N.S. McIntyre et al. "Effects of argon ion bombardment on basal plane and polycrystalline MoS2". en. In: *Surface Science* 237.1-3 (1990), pp. L390–L397. DOI: 10.1016/0039-6028(90)90508-6.

[269] P. W. Anderson. "Absence of Diffusion in Certain Random Lattices". en. In: *Physical Review* 109.5 (1958), pp. 1492–1505. DOI: 10.1103/PhysRev.109.1492.

[270] Nevill Francis Mott et al. *Electronic Processes in Non-Crystalline Materials*. Oxford Classic Texts in the Physical Sciences. Oxford, New York: Oxford University Press, 2012.

[271] John F. Wager. "Real- and reciprocal-space attributes of band tail states". In: *AIP Advances* 7.12 (2017), p. 125321. DOI: 10.1063/1.5008521.

[272] Simone Knief and Wolfgang Von Niessen. "Disorder, defects, and optical absorption in a - Si and a - S i : H". en. In: *Physical Review B* 59.20 (1999), pp. 12940–12946. DOI: 10.1103/PhysRevB.59.12940.

[273] M. Beaudoin et al. "Optical absorption edge of semi-insulating GaAs and InP at high temperatures". en. In: *Applied Physics Letters* 70.26 (1997), pp. 3540–3542. DOI: 10.1063/1.119226.

[274] G. D. Cody et al. "Disorder and the Optical-Absorption Edge of Hydrogenated Amorphous Silicon". en. In: *Physical Review Letters* 47.20 (1981), pp. 1480–1483. DOI: 10.1103/PhysRevLett.47.1480.

[275] Min-I Lee et al. "Defect State Analysis in Ion-Irradiated Amorphous Silicon Heterojunctions by HAXPES". en. In: *physica status solidi (RRL) – Rapid Research Letters* 13.5 (2019), p. 1800655. DOI: 10.1002/pssr.201800655.

[276] Bruno Alessi et al. "Bridging energy bands to the crystalline and amorphous states of Si QDs". en. In: *Faraday Discussions* 222 (2020), pp. 390–404. DOI: 10.1039/C9FD00103D.

[277] Samer Aljishi, Shu Jin, and Lothar Ley. "Defects and disorder broadened band tails in compensated hydrogenated amorphous silicon". en. In: *Journal of Non-Crystalline Solids* 137-138 (1991), pp. 387–390. DOI: 10.1016/S0022-3093(05)80137-1.

[278] Gilles Horowitz. "Validity of the concept of band edge in organic semiconductors". In: *Journal of Applied Physics* 118.11 (2015), p. 115502. DOI: 10.1063/1.4931061.

[279] I. C. Razado et al. "Hydrogen-induced metallization on Ge(111) c(2×8)". en. In: *Applied Surface Science*. Proceedings of the Eight International Conference on Atomically Controlled Surfaces, Interfaces and Nanostructures and the Thirteenth International Congress on Thin Films 252.15 (2006), pp. 5300–5303. DOI: 10.1016/j.apsusc.2005.12.062.

[280] Vincent Derycke et al. "Nanochemistry at the atomic scale revealed in hydrogen-induced semiconductor surface metallization". en. In: *Nature Materials* 2.4 (2003), pp. 253–258. DOI: 10.1038/nmat835.

[281] M. D'Angelo et al. "Hydrogen-Induced Surface Metallization of SrTiO 3 (001)". en. In: *Physical Review Letters* 108.11 (2012), p. 116802. DOI: 10.1103/PhysRevLett.108.116802.

[282] Y. Wang et al. "Hydrogen Induced Metallicity on the ZnO (10 1 ¯ 0) Surface". en. In: *Physical Review Letters* 95.26 (2005), p. 266104. DOI: 10.1103/PhysRevLett.95.266104.

[283] Hongxing Li, Min Huang, and Gengyu Cao. "Markedly different adsorption behaviors of gas molecules on defective monolayer MoS2: a first-principles study". en. In: *Physical Chemistry Chemical Physics* 18.22 (2016), pp. 15110–15117. DOI: 10.1039/C6CP01362G.

[284] M. Houssa et al. "Point defects in MoS 2 : Comparison between first-principles simulations and electron spin resonance experiments". en. In: *Applied Surface Science* 416 (2017), pp. 853–857. DOI: 10.1016/j.apsusc.2017.04.249.

[285] Sang Wook Han et al. "Hydrogen interaction with a sulfur-vacancy-induced occupied defect state in the electronic band structure of MoS2". en. In: *Physical Chemistry Chemical Physics* 21.28 (2019), pp. 15302–15309. DOI: 10.1039/C9CP01030K.

[286] Debora Pierucci et al. "Tunable Doping in Hydrogenated Single Layered Molybdenum Disulfide". en. In: *ACS Nano* 11.2 (2017), pp. 1755–1761. DOI: 10.1021/acsnano.6b07661.

[287] W. Kohn and L. J. Sham. "Self-Consistent Equations Including Exchange and Correlation Effects". In: *Physical Review* 140.4A (1965), A1133–A1138. DOI: 10.1103/PhysRev.140.A1133.

[288] G. Kresse and J. Furthmüller. "Efficiency of ab-initio total energy calculations for metals and semiconductors using a plane-wave basis set". In: *Computational Materials Science* 6.1 (1996), pp. 15–50. DOI: 10.1016/0927-0256(96)00008-0.

[289] G. Kresse and J. Furthmüller. "Efficient iterative schemes for ab initio total-energy calculations using a plane-wave basis set". In: *Physical Review B* 54.16 (1996), pp. 11169–11186. DOI: 10.1103/PhysRevB.54.11169.

[290] Vei Wang et al. "VASPKIT: A user-friendly interface facilitating high-throughput computing and analysis using VASP code". In: *Computer Physics Communications* 267 (2021), p. 108033. DOI: 10.1016/j.cpc.2021.108033.

[291] John P. Perdew, Kieron Burke, and Matthias Ernzerhof. "Generalized Gradient Approximation Made Simple". In: *Physical Review Letters* 77.18 (1996), pp. 3865–3868. DOI: 10.1103/PhysRevLett.77.3865.

[292] Hendrik J. Monkhorst and James D. Pack. "Special points for Brillouin-zone integrations". In: *Physical Review B* 13.12 (1976), pp. 5188–5192. DOI: 10.1103/PhysRevB.13.5188.

[293] James D. Pack and Hendrik J. Monkhorst. ""Special points for Brillouin-zone integrations"—a reply". In: *Physical Review B* 16.4 (1977), pp. 1748–1749. DOI: 10.1103/PhysRevB.16.1748.

[294] Sang Wook Han et al. "Band-gap expansion in the surface-localized electronic structure of MoS 2 (0002)". en. In: *Physical Review B* 86.11 (2012), p. 115105. DOI: 10.1103/PhysRevB.86.115105.

[295] Paolo Giannozzi et al. "QUANTUM ESPRESSO: a modular and open-source software project for quantum simulations of materials". en. In: *Journal of Physics: Condensed Matter* 21.39 (2009), p. 395502. DOI: 10.1088/0953-8984/21/39/395502.

[296] Andrea Dal Corso. "Projector augmented-wave method: Application to relativistic spin-density functional theory". In: *Physical Review B* 82.7 (2010), p. 075116. DOI: 10.1103/PhysRevB.82.075116.

[297] Stefan Grimme et al. "A consistent and accurate ab initio parametrization of density functional dispersion correction (DFT-D) for the 94 elements H-Pu". In: *The Journal of Chemical Physics* 132.15 (2010), p. 154104. DOI: 10.1063/1.3382344.

[298] Voicu Popescu and Alex Zunger. "Extracting E versus $\stackrel{P\vec}{k}$ effective band structure from supercell calculations on alloys and impurities". In: *Physical Review B* 85.8 (2012), p. 085201. DOI: 10.1103/PhysRevB.85.085201.